

Thesis for the acquisition of the academic degree  
Master of Science

**Simulation of the Beam Conditions  
Monitor for the Run III upgrade of the  
LHCb detector and development of a  
control system for the Timepix4  
telescope**

David Rolf  
born in Münster

September 2021

Lehrstuhl für Experimentelle Physik V  
Fakultät Physik  
Technische Universität Dortmund

First corrector: Prof. Dr. Johannes Albrecht  
Second corrector: Prof. Dr. Kevin Kröninger  
Submission date: 30. September 2021

## Abstract

The LHCb experiment is currently undergoing a major upgrade, preparing for the next period of data taking starting in 2022, where the instantaneous luminosity will increase by a factor of five. To ensure a safe operation of the experiment, simulation studies are performed for the Beam Conditions Monitor (BCM), responsible of protecting LHCb against possible damage from the beam. In the first part of this thesis the impact of the changed beam conditions and configurations of the LHCb subdetectors on the BCM settings is evaluated, by studying the BCM response under nominal and failing beam scenarios, respectively. The simulation shows that the BCM will be able to protect the most delicate components of the LHCb detector. For a possible future BCM detector a beam telescope design is considered. In the second part of this thesis a control system is described, that has been developed for the Timepix4 telescope, a beam telescope of the next generation. Two projects are implemented, responsible to remotely control the high voltage of the telescope and to monitor the temperature and humidity. The communication with the hardware has been established and user interfaces have been created for the various controlling and monitoring tasks.

## Kurzfassung

Das LHCb-Experiment wird derzeit umfassend aufgerüstet, um sich auf die nächste Periode der Datennahme ab 2022 vorzubereiten, in der die instantane Luminosität um den Faktor fünf zunehmen wird. Um einen sicheren Betrieb des Experiments zu gewährleisten, werden Simulationsstudien für den Beam Conditions Monitor (BCM) durchgeführt, welcher für den Schutz von LHCb durch mögliche Schäden durch den Strahl verantwortlich ist. Im ersten Teil dieser Arbeit werden die Auswirkungen der geänderten Strahlbedingungen und Konfigurationen der LHCb-Subdetektoren auf die Einstellungen des BCM untersucht, indem das Verhalten des BCM bei nominalen und fehlerhaften Strahlszenarien betrachtet wird. Die Simulation zeigt, dass der BCM in der Lage sein wird, die empfindlichsten Komponenten des LHCb-Detektors zu schützen. Für einen möglichen zukünftigen BCM-Detektor wird ein Strahlenteleskopdesign in Betracht gezogen. Im zweiten Teil dieser Arbeit wird ein Kontrollsystem beschrieben, welches für das Timepix4-Teleskop, ein Strahlenteleskop der nächsten Generation, entwickelt wurde. Es sind zwei Projekte implementiert, die für die Steuerung der Hochspannung des Teleskops und für die Überwachung der Temperatur und der Luftfeuchtigkeit zuständig sind. Die Kommunikation mit der Hardware wurde hergestellt und Benutzeroberflächen sind für die verschiedenen Steuerungs- und Überwachungsaufgaben erstellt worden.





# Contents

<b>1</b>	<b>Introduction</b>	<b>1</b>
1.1	The Large Hadron Collider at CERN . . . . .	2
1.2	The LHCb experiment . . . . .	4
1.2.1	The LHCb upgrade detector . . . . .	4
<b>2</b>	<b>Run III simulation of the Beam Conditions Monitor</b>	<b>6</b>
2.1	The Beam Conditions Monitor . . . . .	6
2.1.1	Beam dump logic . . . . .	8
2.2	The upgraded Vertex Locator . . . . .	9
2.3	Determination of new thresholds . . . . .	11
2.3.1	Simulation data . . . . .	11
2.3.2	Occupancy . . . . .	12
2.3.3	Energy deposition . . . . .	13
2.3.4	Maximal energy deposition . . . . .	17
2.3.5	Correlation between the detectors . . . . .	21
2.3.6	Determination of currents . . . . .	22
2.3.7	New thresholds . . . . .	23
2.4	Detector response under adverse beam conditions . . . . .	25
2.4.1	Beam scraping simulation . . . . .	25
2.4.2	Comparison of the coverage . . . . .	26
2.4.3	RF foil temperature estimation . . . . .	31
2.4.4	Beam 2 beam scraping . . . . .	32
<b>3</b>	<b>Development of a control system for the Timepix4 telescope</b>	<b>33</b>
3.1	The Timepix4 telescope . . . . .	33
3.1.1	Layout . . . . .	34
3.2	The slow control system . . . . .	36
3.2.1	Overview . . . . .	36
3.2.2	WinCC OA and the JCOP framework . . . . .	37
3.2.3	Alarm handling . . . . .	40
3.2.4	Data logging . . . . .	41
3.2.5	Communication protocols . . . . .	42
3.3	High Voltage control . . . . .	43
3.3.1	Hardware . . . . .	43

3.3.2	Drivers and software . . . . .	45
3.3.3	DIM server . . . . .	46
3.3.4	User interface . . . . .	48
3.4	Temperature and Humidity control . . . . .	52
3.4.1	Hardware . . . . .	52
3.4.2	Estimating the dew point . . . . .	56
3.4.3	Drivers and software . . . . .	56
3.4.4	User interface . . . . .	57
3.5	Combined projects . . . . .	59
<b>4</b>	<b>Conclusion and Outlook</b>	<b>60</b>
<b>A</b>	<b>Additional plots of the simulation</b>	<b>I</b>
A.1	Occupancy plots . . . . .	I
A.2	Energy deposition plots . . . . .	III
A.3	Coverage of the detectors for beam 2 . . . . .	IV
<b>B</b>	<b>Slow control operator panels</b>	<b>VI</b>
B.1	Standard panels . . . . .	VI
B.2	High Voltage panels . . . . .	VIII
B.3	Temperature and Humidity panels . . . . .	XI
	<b>Bibliography</b>	<b>XIV</b>

# 1 Introduction

In the research of the matter of the universe physicists around the world are constantly striving to improve the description of the fundamental forces. The Standard Model (SM) is the most complete model so far, describing the electromagnetic, the weak, and the strong interactions. However, it does come with shortcomings, where it fails to accurately depict the reality. For example, in the SM neutrinos are considered massless, but neutrino oscillations prove that neutrinos are indeed massive. The fundamental force of gravitation is not described by the SM as well. Furthermore, it does not provide an explanation for dark matter, whose existence is demonstrated by astronomical observations. To research all these phenomena, large particle accelerators are built, where the particles are accelerated almost to the speed of light and collided [1, 2].

One of these particle accelerators is the Large Hadron Collider (LHC) at CERN, described in section 1.1. Multiple experiments are stationed at the LHC. The experiment of interest for this thesis is the LHCb experiment, covered in section 1.2. The work of this thesis has two main topics. Currently (2019-2021), during the Long Shutdown 2 (LS2), the LHCb detector is undergoing a major upgrade. In order to successfully protect the sensitive detector components, the safety system of the LHCb experiment, namely the Beam Conditions Monitor (BCM), needs to re-evaluate its settings. The simulation work performed for this purpose represents the first part of this thesis and is presented in chapter 2.

For a possible future BCM detector a beam telescope design is considered, that simultaneously would also allow for precise luminosity measurements. A telescope that is currently in development is the Timepix4 telescope. Its design is an excellent prototype for a future BCM and luminosity detector. In the second part of this thesis a slow control system is described, that has been developed for the Timepix4 telescope. The test setup created for this purpose and the functionalities implemented are described in chapter 3.

## 1.1 The Large Hadron Collider at CERN

CERN (in french: Conseil Européen pour la Recherche Nucléaire) is an European institute nearby Geneve, located at the border between Switzerland and France. With 27 km circumference the Large Hadron Collider (LHC) [3] at CERN is the largest particle accelerator in the world. Mostly protons are accelerated in opposite direction in two separate beam tubes to an energy of 6.5 TeV.

The four big experiments at the LHC are LHCb [4], ATLAS [5], CMS [6] and ALICE [7]. The experiments study the structure of matter as well as the interactions between the particles. The LHCb detector specialises on precise measurements of the CP violation and rare decays of B and D mesons. The ATLAS and CMS detectors are general purpose detectors, positioned at opposite sides of the LHC. They are used to search for new physic phenomena at high energy scales, making use of the full luminosity provided by the LHC. One major achievement was the Higgs discovery in 2012 [8, 9]. The ALICE detector focuses on the study of Quantum Chromo Dynamic (QCD) effects. For this it is optimised for taking data with LHC beams of lead ions, studying the physics of strongly interacting matter.

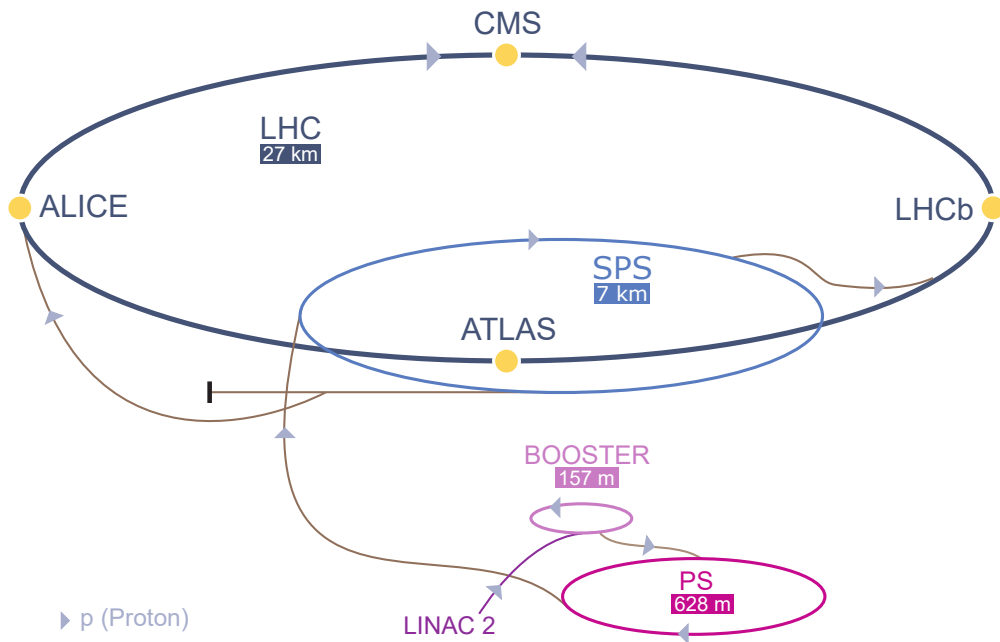


**Figure 1.1:** Schematic of the LHC accelerator complex at CERN. Below the accelerators their circumference is listed. The arrows give the flight direction of the protons within the accelerators. Modified from reference [10].

The CERN complex is shown schematically in figure 1.1. Since the magnets, which hold the particles on their path, are not arbitrarily variable in their field strength, the protons are accelerated in multiple sections. Firstly, they are accelerated in the Linear Accelerator 2 (LINAC 2) to an energy of 50 MeV. Afterwards the Proton Synchrotron Booster (BOOSTER) accelerates the protons to an energy of 1.4 GeV. From there they continue to the Proton Synchrotron (PS) and afterwards to the Super Proton Synchrotron (SPS). Finally, they are injected into the LHC. At the four experiments the protons collide at an energy mass of 13 TeV [11].

The beams inside the LHC are not continuous but consist of a train of bunches. The collisions of the protons at the experiments are therefore referred to as bunch crossings. A bunch consists of  $\sim 1 \times 10^{11}$  protons and revolves around the LHC with a frequency of 11 245 Hz. The bunches of a beam are spaced dependent on the so-called filling scheme. In the beginning of the data taking a bunch spacing of 50 ns was used. Later it was updated to 25 ns, resulting in a collision rate of 40 MHz. The spacing of the bunches in the beams is not uniform. Some of the positions in the beam that could contain a bunch are left empty, resulting in an effective bunch crossing rate of 30 MHz.

The bunches are not all injected at the same time. The period before the beam is completely filled is called the injection mode. When the beam has stabilised, the time period of the fill is referred to as the physics mode, which is used for the data taking. This is also referred to as nominal conditions. Before each fill a single bunch is injected into the beam to confirm proper operation of all machine components. This procedure is referred to as the single bunch mode.

In case of adverse beam conditions, the beam can be aborted from the accelerator, called beam dump, to protect the detectors from any damage. The responsible system is the Beam Interlock System (BIS). It constantly provides a current in a serial loop. The beam is dumped, when this beam permit signal is withdrawn by one of the connected monitoring systems.

## 1.2 The LHCb experiment

The Large Hadron Collider beauty (LHCb) [4] detector is optimised for the study of hadrons containing beauty (b) and charm (c) quarks. Main goals are precise measurements of CP violation and investigation of rare B and D meson decays.

The LHCb detector is, differently from the other three experiments, a single arm forward spectrometer. This is a design choice based on the angular distribution of the b quarks, which are mostly produced at small angles to the beam.

### 1.2.1 The LHCb upgrade detector

The LHCb detector successfully operated in 2011 and 2012 (Run I) at centre of mass energies of 7 TeV and 8 TeV, respectively, and from 2015 to 2018 (RunII) at a centre of mass energy of 13 TeV. The experiment is currently (2019-2021) being upgraded in order to cope with a five times larger instantaneous luminosity in Run III, starting in spring 2022. Among the main changes the hardware trigger is removed, the tracking detectors are replaced, and the electronics for all subdetectors are upgraded to readout at the 40 MHz collision rate. A schematic view of the upgraded LHCb detector [12] is shown in figure 1.2.

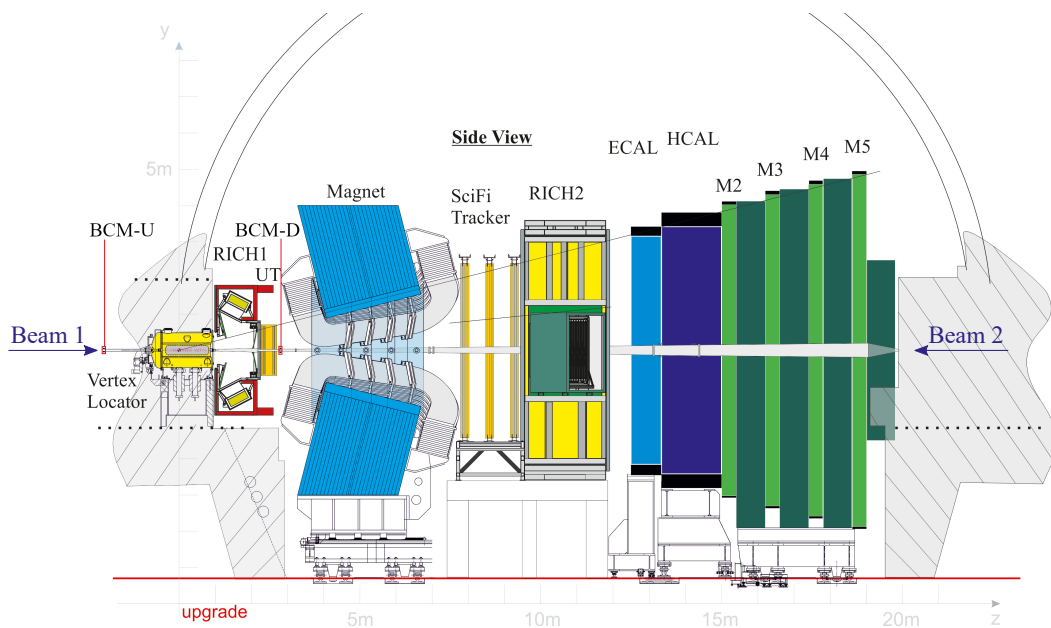


**Figure 1.2:** Schematic of the LHCb upgrade detector with its individual components. Modified from reference [13].

The standard LHCb coordinate system [14] is adopted, with the  $z$ -axis along the beam direction, the  $y$ -axis pointing upwards, and the  $x$ -axis pointing outwards of the LHC ring. The origin is placed at the Interaction Point (IP). The directions of the two beams are also shown in the figure. The protons of beam 1 transverse LHCb towards positive  $z$  direction, the protons of beam 2 towards negative  $z$  direction.

The tracking system is composed of the VERtEX LOcator (VELO) [15], Upstream Tracker (UT) [16] and Scintillating Fibre (SciFi) tracker [17]. The VELO surrounds the collision region. It is used to measure the tracks close to the collision point and to determine the primary and secondary vertices of the decays. The secondary vertex is a characteristic of  $b$  and  $c$  hadrons due to their long lifetime. The upgraded VELO maintains the same mechanical structure of the previous detector, including two movable halves that open during injection and close when the beams are stable. The silicon strips of the previous detector are replaced by pixel sensors. Upstream and downstream of the VELO, mounted on the concrete wall and onto the beam pipe are the upstream and downstream stations of the Beam Conditions Monitor (BCM). The BCM is used to protect the detector in case of adverse beam conditions [18]. Because of their relevance for the simulation part of this thesis the VELO and the BCM are described in more detail in sections 2.2 and 2.1, respectively.

The UT and the SciFi tracker are positioned upstream and downstream of the magnet, respectively. By bending the tracks with the magnet, the momentum of the particles can be determined. The magnet can be operated in the Magnet Up (MU) and the Magnet Down (MD) configuration. Here up and down is the direction of the magnetic field, thus the tracks bend on the horizontal plane. The UT replaces the former Tracker Turicensis (TT) and is composed of silicon strips. The SciFi tracker replaces the former Inner Tracker (IT) and Outer Tracker (OT), implementing a novel technology of closely packed scintillating fibres. Compared to the IT and OT this increases the granularity of the detector.

The particle identification systems are the two Cherenkov detectors (RICH), the electromagnetic and hadronic calorimeters (ECAL and HCAL) and the muon stations. The RICH detectors make use of Cherenkov radiation between 200 nm and 600 nm. The RICH1 detector is placed upstream of the magnet and identifies charged particles with comparably low momentum. The RICH2 detector is placed downstream of the magnet and identifies particles with comparably high momentum. The calorimeters are used for particle identification by measuring their energy deposition. Electrons and photons deposit their energy mainly in the ECAL, while hadrons deposit their energy mostly in the HCAL. The muon chambers (M2 to M5) are used to identify and reconstruct muon tracks.

## 2 Run III simulation of the Beam Conditions Monitor

The first part of this thesis is dedicated to the Run III simulation studies of the BCM. Due to the different running conditions and the new configurations of some of the LHCb subdetectors in Run III, it is required to re-evaluate the settings of the BCM to ensure a safe operation of the experiment.

The VELO, in its closed position, is the LHCb component located closest to the beam. It is therefore exposed to the highest radiation and is the most endangered by failing beam scenarios. Thus, the VELO is used as the reference detector when evaluating the BCM settings.

The relevant detector components for this simulation study, the BCM and VELO, are described in detail in sections 2.1 and 2.2, respectively. Two types of Run III simulations are performed: under nominal beam conditions, in order to propose new settings for the BCM, and under adverse beam conditions, to verify the effectiveness of the proposed settings. The former is described in section 2.3, the latter in section 2.4.

### 2.1 The Beam Conditions Monitor

The LHCb detector components are exposed to radiation during operation. Should the radiation level increase drastically due to a critical beam scenario, like misalignment of the beams, the sensitive parts of the detector might be damaged or potentially destroyed. The BCM [18] is constructed as a safety system to prevent such damage to the LHCb detector components. Should an adverse beam scenario occur the BCM will request a beam dump, thus preventing the beam from damaging the detector.

The BCM [18] consists of a station upstream (BCM-U) and a station downstream (BCM-D) of the IP, located at  $z = -2131$  mm and  $z = 2765$  mm, respectively. The BCM-U station is mounted directly on the concrete wall of the LHCb cavern, while the BCM-D station is mounted onto the beam pipe between the UT tracker and the magnet.



A schematic of both BCM stations is depicted in figure 2.1. Each BCM station uses a set of eight polycrystalline Chemical Vapor Deposited (pCVD) diamond sensors positioned symmetrical around the beam pipe centre. Each sensor has a sensitive area of 10 mm by 10 mm and a thickness of 0.5 mm. The sensitive area of the BCM-U station begins at a radial distance of 50.5 mm, while the one of the BCM-D station begins at a radial distance of 37.0 mm. The artificially created pCVD diamond material was chosen for its high resistance to radiation damage and its charge collection capabilities making it suitable for operation close to the beam pipe.

The BCM was operated successfully during Run I and Run II. The beam was dumped a few times during operations, with post-mortem data confirming the necessity for this action. Only towards the end of Run II two sensors showed damage due to radiation [19]. The BCM detector is currently being refurbished for Run III. All the sensors are being replaced. The detector layout is identical to Run I and Run II, except for the mechanical support for the BCM-U station [19].

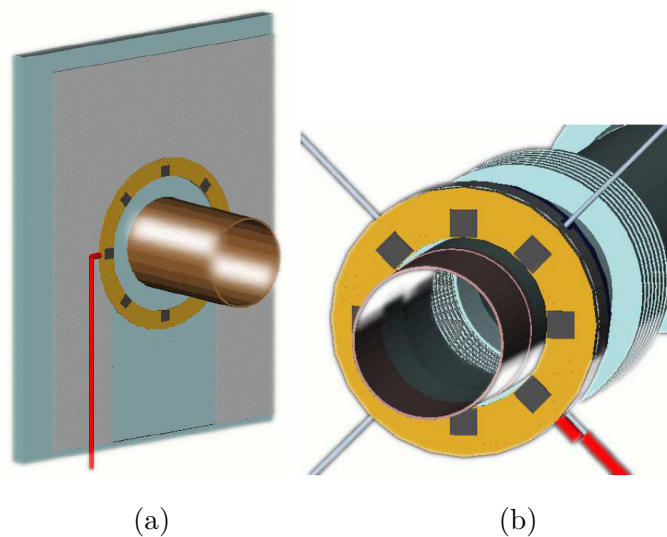


**Figure 2.1:** Drawing of the BCM-U (a) and the BCM-D (b) stations. The BCM stations are depicted in yellow. The diamond sensors are represented by the grey squares. The brown tube corresponds to the beam pipe. The readout cables are depicted in red. Figure (a) includes a section of the concrete wall where the BCM-U station is mounted. Adopted from reference [18].

### 2.1.1 Beam dump logic

The BCM is in constant communication with the accelerators BIS. In case of a failing beam scenario, the BCM removes the beam permit signal and the beam is dumped. The BCM implements the following dump logic [18]. For each diamond sensor a set of running sums (RS) is calculated over a different number of timeframes of 40  $\mu$ s. One timeframe of 40  $\mu$ s is the integration time of the BCM, which corresponds to a signal rate of 25 kHz. It is to be noted that this is low compared to the 30 MHz effective LHC collision rate at the LHCb detector.

For each timeframe the detector readout is converted into a current. Several RS are used, referred to as  $RS_n$ . Each  $RS_n$  is a summation over the  $n$  most recent current readouts. For example,  $RS_1$  is simply the most recent current readout, while  $RS_{32}$  is the sum over the 32 most recent current readouts.

Different threshold values are set depending on the operation mode. While four different modes can be implemented in the firmware, only two of them are employed: mode 0 as the physics mode, and mode 3 as the injection mode. For each of them two abort algorithms are implemented: the slow and the fast abort logic.

In the fast abort logic, the  $RS_1$  is considered and continuously monitored for each sensor. If the corresponding threshold  $t_{RS_1}$  is exceeded the sensor is flagged. When three adjacent sensors in one BCM station are flagged the beam is dumped. This triple redundancy reduces the risk of triggering a beam dump due to dark current fluctuations. In the injection mode the fast abort logic is modified to use a  $RS_2$ , because it is favourable for single bunches.

In the slow abort logic for each sensor a  $RS_{32}$  is calculated. The advantage of integrating over a longer time period is that most of the noise is averaged out [20]. A so-called  $RS_{32}$ -SUM is computed, by adding up the  $RS_{32}$  values of the eight sensors of a station, leaving out the two highest values and the lowest value to remove outliers:

$$RS_{32}\text{-SUM} = \sum_{i=0}^4 RS_{32}[i]. \quad (2.1)$$

Hence, this sum considers the energy deposition in a complete detector station. The beam is dumped when the corresponding threshold  $t_{RS_{32}\text{-SUM}}$  is exceeded.

## 2.2 The upgraded Vertex Locator

The VELO is one of the LHCb subdetectors being upgraded in order to maintain or even improve its performance in the harsher environment of Run III, compared to Run I and Run II. The upgraded VELO [21, 15] consists of 26 stations placed along the  $z$  axis near the IP. Each station is composed of two modules, one on each side of the beam. The modules located at positive  $x$  are in the so-called A side, the modules at negative  $x$  in the C side of the detector. The two sides of the VELO can be retracted along the  $x$  axis during beam injection, to ensure that the sensitive parts are not damaged by unstable beams. A schematic of one side of the upgraded VELO and of a station viewed from the front in closed position is given in figure 2.2.

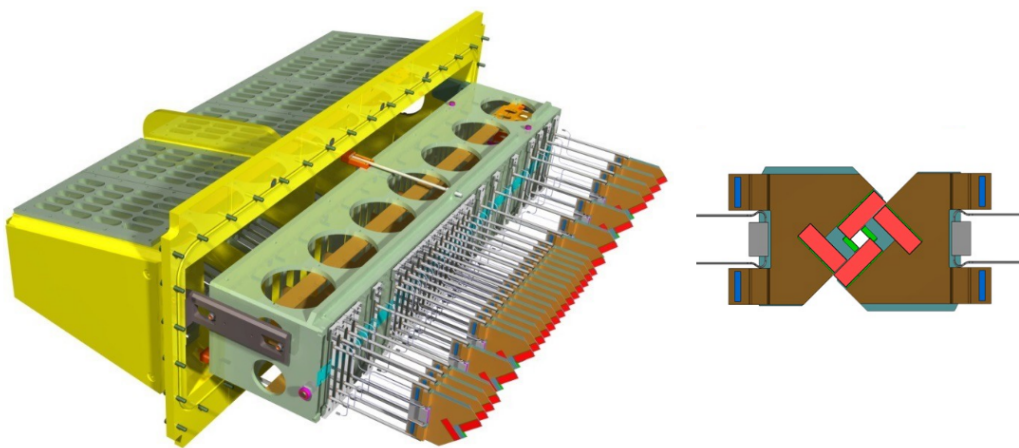


**Figure 2.2:** Schematic of one side of the upgraded VELO (left), as well as the front view of a station in its closed position (right). Adopted from reference [22].

Each module consists of four silicon pixel tiles arranged in a L shape geometry. Two of the tiles are placed on the front side and two on the back side of the module. Each tile is composed of a  $1.4 \times 4.2$  mm sensor with  $55 \times 55$   $\mu\text{m}$  pixels, bump bonded onto three VeloPix ASICs (Application Specific Integrated Circuits). The sensors are  $200$   $\mu\text{m}$  thick. The tiles are cooled by a micro channel cooling system embedded in a silicon substrate, which also provides the mechanical support for the module. In its closed position the minimal radial distance of the sensors to the beam axis is  $5.1$  mm. For the VELO operated during Run I and Run II the distance was  $8.2$  mm. The two sides of a VELO station are positioned with a slight offset along the  $z$  direction, which allows for an overlap of the modules in the  $x$  direction for full coverage.

## 2 Run III simulation of the Beam Conditions Monitor

The VELO modules are enclosed in a separate vacuum than the beam by two aluminium RF boxes, one for each side of the VELO. The part of the RF box that separates the two VELO sides is referred to as the RF foil. The RF foil has a thickness of  $200\ \mu\text{m}$  and is corrugated in order to minimise the material budget. In its closed position the minimal distance of the RF foil to the beam is about  $3.5\ \text{mm}$ . For the VELO operated during Run I and Run II the distance was about  $5\ \text{mm}$ . One of the main challenges for the VELO is the non-uniformity of radiation exposure. The expected radiation dose for the VELO has been estimated in reference [15]. The fluence contours in the  $r$ - $z$  plane are shown in figure 2.3, where  $r$  is the radius from the beam axis. The vertical lines along the horizontal axis indicate the positions of the VELO stations.

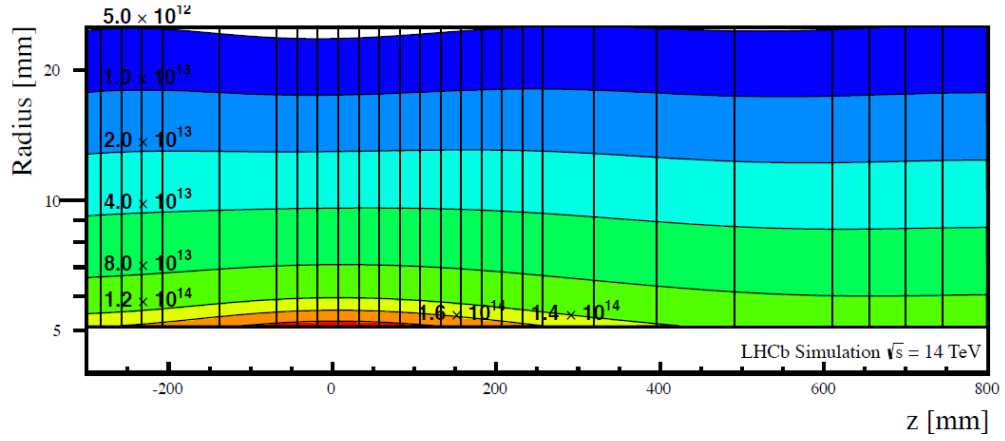


**Figure 2.3:** The expected integrated radiation dose after  $50\ \text{fb}^{-1}$  of integrated luminosity as a function of the position in  $z$  and the radial distance from the beam axis  $r$ . Adopted from reference [15].

## 2.3 Determination of new thresholds

To account for the different beam conditions and upgraded layout of the LHCb subdetectors, a new set of BCM thresholds needs to be determined. For this three Monte Carlo (MC) samples are generated, corresponding to different data taking periods (2011, 2018, upgrade) in nominal beam conditions. This corresponds to the physics mode in the BCM beam dump logic.

Firstly, the occupancy in the BCM stations is studied to investigate how the hits are distributed in the detectors. Secondly, it is evaluated how much energy is deposited in the BCM and the VELO detectors. Additionally, for the VELO sensors and the RF foil a quantity, the maximum energy deposition per unit volume, is defined to estimate a potential damage to the components. The results are compared between the three simulation samples. Thirdly, the correlation between the BCM and the VELO detectors is investigated to verify that the BCM response can be used to provide protection for the VELO sensors. Finally, the BCM currents are calculated from the energy deposition in the BCM sensors and the new threshold values are proposed based on the results.

### 2.3.1 Simulation data

Three datasets of MC samples are generated. The simulation software used is named **Gauss** [23]. The simulation of the collisions provided by **Pythia** [24], the simulation of the particle decays by **EvtGen** [25] and the simulation of the interaction between the particles and the detector by **Geant4** [26]. The simulation conditions for the data samples used are listed in table 2.1.

**Table 2.1:** The simulation conditions used for the Run I, the Run II, and the Run III dataset, with the beam energy  $E_{\text{beam}}$ , the number of bunches colliding at LHCb per cycle  $n_b$ , the instantaneous luminosity  $L_{\text{inst}}$ , the interactions per bunch crossing  $\nu$ , the visible interactions per bunch crossing  $\mu$ , the bunch  $z$  RMS  $z_{\text{RMS}}$ , the optical function  $\beta^*$ , and the normalised emittance  $\epsilon_n$ .

	Run I (2011)	Run II (2018)	Run III
$E_{\text{beam}}$	3.5 TeV	6.5 TeV	7 TeV
$n_b$	810	2300	2400
$L_{\text{inst}}$	$2 \times 10^{32} \text{ cm}^{-2} \text{ s}^{-1}$	$4 \times 10^{32} \text{ cm}^{-2} \text{ s}^{-1}$	$2 \times 10^{33} \text{ cm}^{-2} \text{ s}^{-1}$
$\nu$	2.0	1.6	7.6
$\mu$	1.4	1.1	5.5
$z_{\text{RMS}}$	82 mm	52 mm	90 mm
$\beta^*$	3.10 m	3.00 m	2.79 m
$\epsilon_n$	3.7 $\mu\text{m}$	3.6 $\mu\text{m}$	3.8 $\mu\text{m}$

The first data sample corresponds to Run III conditions. It implements the upgraded detector layout. It features a 25 ns bunch spacing, corresponding to an instantaneous collision rate of 40 MHz. Because of the LHC filling scheme this results in an effective event rate of 30 MHz [27, 28]. This means within one interval of 40  $\mu$ s of the BCM integration time 1200 events occur, where an event corresponds to one bunch crossing. A total of 256 000 events are generated. This sample will be referred to as the Run III dataset.

The second data sample corresponds to 2018 conditions. The detector layout from Run I and Run II is used. The bunch spacing is the same as for the Run III dataset, resulting again in 1200 events during the 40  $\mu$ s of the BCM integration time. A total of 75 000 events are generated. This sample will be referred to as the Run II dataset.

The third data sample corresponds to 2011 conditions. The detector layout from Run I and Run II is used. A different bunch spacing, and filling scheme is used resulting in an effective event rate of 15 MHz and 600 events per 40  $\mu$ s [29]. A total of 100 000 events are generated. This sample will be referred to as the Run I dataset. While all simulation samples have been processed in the same way, the following results are presented for the Run III dataset, unless otherwise specified.

### 2.3.2 Occupancy

The occupancy corresponds to the number of hits in the detector in a given time window. Here it is evaluated on a per event basis and the 40  $\mu$ s readout time of the BCM. The per event occupancy for the BCM-U sensors is shown in figure 2.4 (a). In nominal conditions the occupancy is comparable in all eight BCM-U sensors, and similarly for the BCM-D sensors. The occupancy is about three times larger in the BCM-U sensors, with an average of 1.65 hits per event and 1976 hits per 40  $\mu$ s, compared to 0.57 hits per event and 690 hits per 40  $\mu$ s in the BCM-D sensors. This is due to the larger amount of material upstream of the VELO detector. While in the sensitive area of the LHCb detector the material is minimised, this is not the case for the area of the BCM-U station outside the LHCb acceptance. The interaction with the detector material leads to the creation of secondary particles that are than detected by the BCM-U station.

In general, the occupancy of the BCM stations (in total around  $2.13 \times 10^4$  hits per 40  $\mu$ s) is low compared to the occupancy of the VELO sensors (in total around  $2.28 \times 10^6$  hits per 40  $\mu$ s) and the RF foil (in total around  $4.10 \times 10^6$  hits per 40  $\mu$ s). This is due to the larger radial distance of the BCM sensors from the beam axis and larger distance from the IP along the beam direction.

A radial dependency is observed within each sensor in both stations. This is shown in figure 2.4 (b) for a sensor of each station, by studying the average occupancy per  $40\ \mu\text{s}$  as a function of the radial distance to the beam axis  $r$ . Further occupancy plots can be found in appendix A.1.

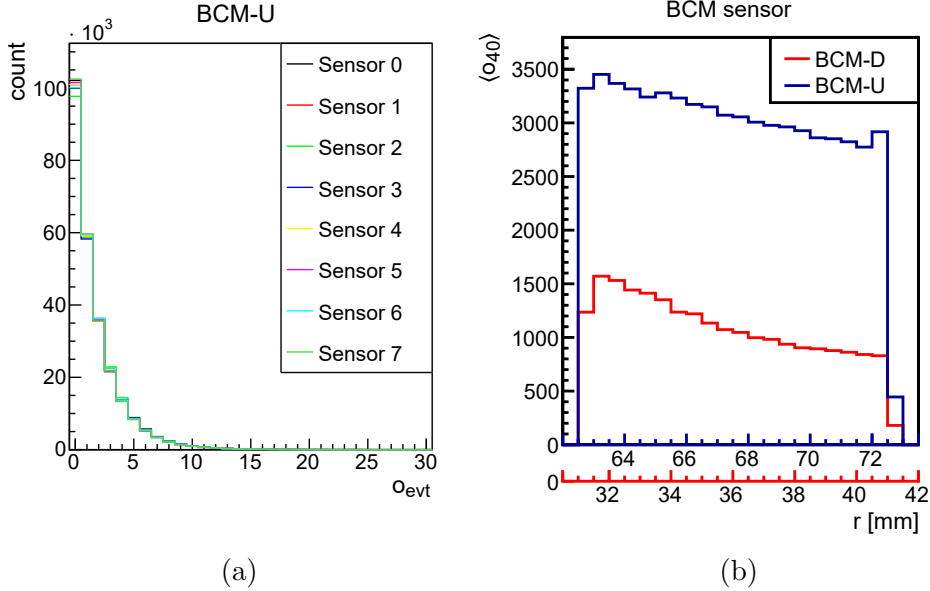


**Figure 2.4:** The occupancy per event  $o_{\text{evt}}$  in the BCM-U sensors (a) and the mean occupancy per  $40\ \mu\text{s}$  ( $\langle o_{40} \rangle$ ) for the first sensor of each station as a function of the radial distance to the beam axis  $r$  (b).

### 2.3.3 Energy deposition

In this section the energy deposition resulting from the hits in the detector is investigated. Firstly, a look is taken at the deposition of a single particle in a sensor. The distribution of the energy loss of single particles interacting with thin absorbers, like the silicon sensors of the VELO or the BCM diamond sensors, can be described by a convolution of a Landau with a Gaussian distribution [30, 31, 32].

The energy loss of the particles is shown for the simulation of the BCM in figure 2.5 (a) and figure 2.5 (b). Since the hits are uniformly distributed over the sensors of the same BCM station, as found in the studies of the occupancy, the plots combine all the sensors of a BCM station to increase the size of the data sample. The distribution of the deposited energy of the individual hits in the detector stations are fitted with the convoluted Landau function, with a Most Probable Value (MPV) of the distribution of  $0.226\ \text{MeV}$  for the BCM-U and  $0.222\ \text{MeV}$  for the BCM-D

station, respectively. The values below 0.2 MeV result mostly from interactions with material other than the sensors and are therefore not described by the fit.

The energy deposited in the detectors by multiple particles in an event is not a trivial distribution. This is shown for the two BCM stations in figure 2.5 (c) and (d), depicting the energy deposition in the stations per event. The peaks that are visible at the lower energies are where just a few single hits are detected in the BCM sensors. The first peak is located at the MPV of a single hit in a sensor, the second one at two times the MPV and so on.

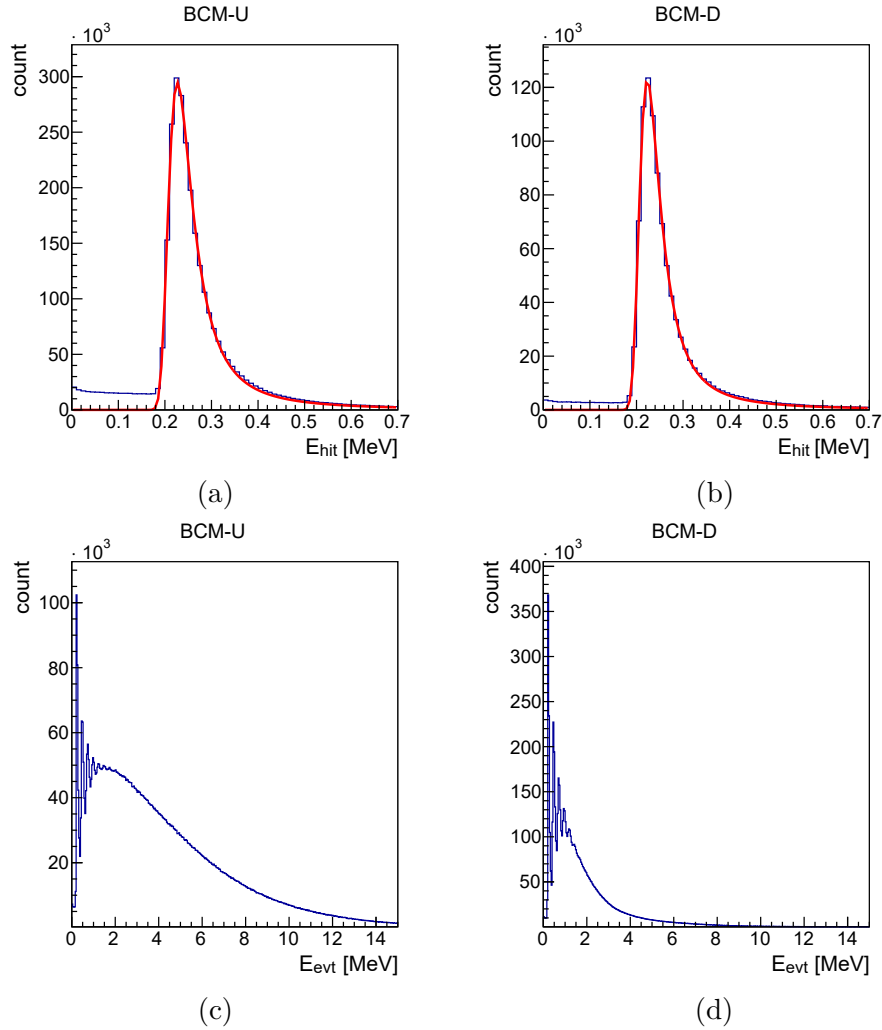


**Figure 2.5:** The top figures show the energy deposited per hit  $E_{hit}$  in the BCM-U station (a) and the BCM-D station (b). The graphs are fitted by a Landau function convoluted with a Gaussian distribution. The bottom figures show the energy deposited per event  $E_{evt}$  in the BCM-U station (c) and the BCM-D station (d).



Of special interest is the energy deposition in the  $40\ \mu\text{s}$  of the BCM integration time, as shown for the BCM-U station in figure 2.6 (a). For this integration time the energy distribution is well described by a Gaussian function. Therefore, the mean value of the energy deposition is determined by fitting a Gaussian function to the distribution.

The same procedure is applied for the energy deposited in the VELO sensors and the RF foil (appendix A.2). The resulting values for the mean energy deposition  $\langle E_{40} \rangle$  per  $40\ \mu\text{s}$  for the BCM stations, the VELO sensors, and the RF foil are given in table 2.2. The uncertainties correspond to the sigma values of the Gaussian fits.

**Table 2.2:** Mean energy deposition per  $40\ \mu\text{s}$  for the studied detector components. The entry for the sensors refers to the energy deposition in all the VELO sensors combined.

Detector component	$\langle E_{40} \rangle$ [MeV]
BCM-U	$(4.932 \pm 0.127) \times 10^3$
BCM-D	$(2.027 \pm 0.117) \times 10^3$
Sensors	$(2.299 \pm 0.033) \times 10^5$
RF foil	$(1.104 \pm 0.015) \times 10^6$

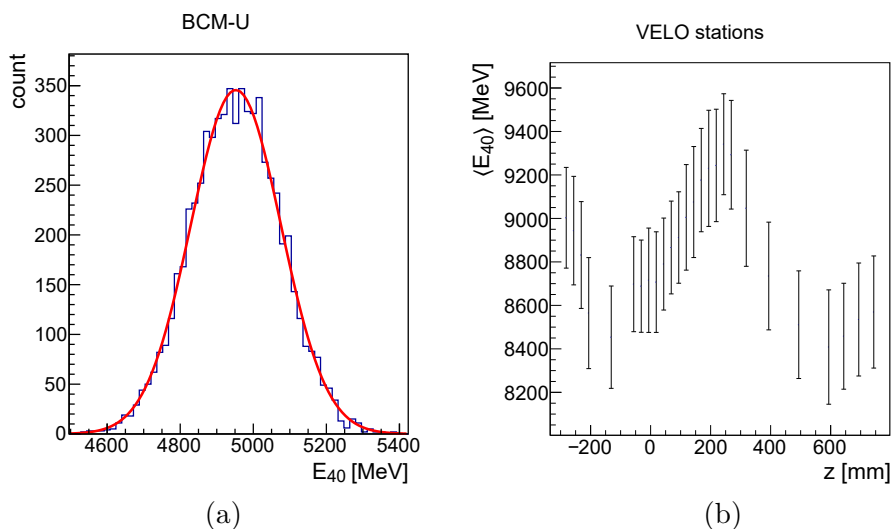


**Figure 2.6:** The energy deposition per  $40\ \mu\text{s}$   $E_{40}$  in the BCM-U station (a) and the mean energy deposition per  $40\ \mu\text{s}$   $\langle E_{40} \rangle$  in the individual VELO stations as a function of their respective  $z$  location (b).

For the VELO sensors it is also interesting to look at the mean energy deposition per  $40\ \mu\text{s}$  of the individual stations. This is shown in figure 2.6 (b) as a function of the  $z$  position of the corresponding station. The energy deposition depends on the radial distance and position along the beam axis, following the trend of figure 2.3. The mean energy deposition in the VELO stations ranges from 8385 MeV to 9345 MeV per  $40\ \mu\text{s}$ .

Since the occupation studies show that the distribution in the detectors is not uniform as a function of radial distance from the beam axis, the two-dimensional distributions of the mean energy deposition per  $40\ \mu\text{s}$  have been studied. For the BCM stations and the first VELO station this is shown in figure 2.7.

In figure 2.7 (a) the outer ring corresponds to the BCM-U sensors and the inner ring to the BCM-D sensors. The higher energy deposited in the BCM-U station is visible. In figure 2.7 (b) the shape of the VELO sensors can be seen, due to the overlap between front and back sensors, highlighted by an increased energy deposition. The two-dimensional distributions of the RF foil can be found in appendix A.2.

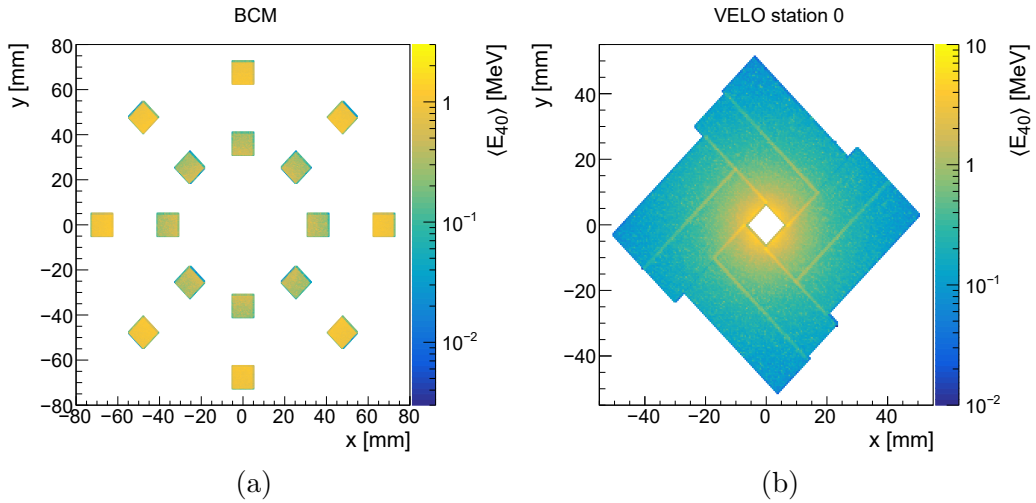


**Figure 2.7:** The projections onto the  $x$ - $y$  plane of the mean energy deposited per  $40\ \mu\text{s}$   $\langle E_{40} \rangle$  in the BCM stations (a) and in VELO station 0 (b).

### 2.3.4 Maximal energy deposition

In order to quantify a possible damage to the sensitive detector components, the quantity  $\Delta Q_{40}$  is defined. It represents the maximum value of the mean energy deposition per  $40\ \mu\text{s}$  per unit volume. The methods developed to determine this quantity for both the VELO sensors, and the RF foil are briefly described in this section. For better binning the  $x$ - $y$  coordinates are rotated by  $45^\circ$ , to the new reference frame  $x'$  and  $y'$ .

For the VELO sensors  $\Delta Q_{40}$  is determined by studying the energy deposition projection onto the  $x'$ - $y'$  plane for each individual VELO station in bins of  $1\ \text{mm}^2$ . This is done separately for the front and back side sensors of each station, in order to account for their overlap. Taking the highest bin value of all the stations and dividing by the sensor thickness  $d_{\text{VELO}} = 0.2\ \text{mm}$  results in a value of  $\Delta Q_{40}$  of:

$$\Delta Q_{40,\text{VELO}} = 108.41\ \text{MeV}\ \text{mm}^{-3}. \quad (2.2)$$

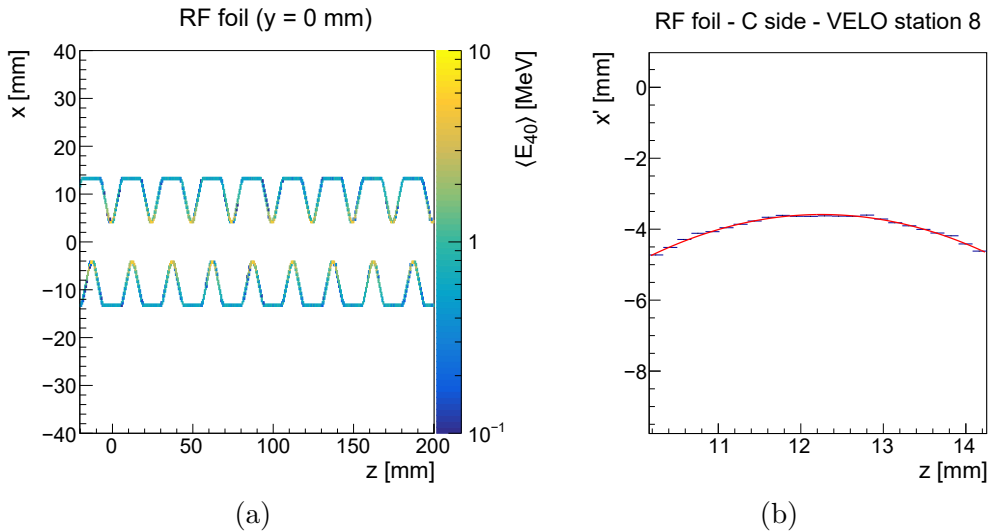


**Figure 2.8:** The mean energy deposition per  $40\ \mu\text{s}$   $\langle E_{40} \rangle$  in the RF foil projected in the  $z$ - $x$  plane at  $y = 0\ \text{mm}$  (a) and fitted profile of the innermost region of the corrugation around the C side of VELO station 8 (b).

For the RF foil the shape along  $z$  is not as simple compared to the VELO sensors. This can be seen from figure 2.8 (a), where the  $z$ - $x$  energy deposition projection at  $y = 0\ \text{mm}$  is shown for a part of the RF foil. To simplify the task of finding  $\Delta Q_{40}$  each corrugation of the RF foil is considered individually, by taking slices around the  $z$  positions of the VELO stations.

Two methods are adopted for the RF foil. The first method uses the same principle that is used for the VELO sensors. The energy deposition projection onto the  $x'$ - $y'$  plane for each individual RF corrugation is studied in bins of  $1 \text{ mm}^2$ . The highest bin value of all the corrugations is taken and divided by the approximated combined thickness of one corrugation  $d_{\text{Corr}} = 2\sqrt{2}d_{\text{RF}}$ , where  $d_{\text{RF}} = 0.2 \text{ mm}$  is the RF foil thickness and assuming a simplified triangular geometry. This results in a value of  $\Delta Q_{40}$  of:

$$\Delta Q_{40,\text{RF},1} = 258.42 \text{ MeV mm}^{-3}. \quad (2.3)$$

The first method can be used for both nominal and adverse beam conditions. A second method is developed, which describes more accurately the shape of the corrugations, but only around the tip of the corrugation, where the radial distance to the beam axis is minimal. Hence, this method can only be used in cases where the maximum energy is deposited at that location. This is the case in nominal beam conditions, but not necessarily in critical beam scenarios.

The method unfolds the shape of the RF foil by fitting the regions of the corrugations that are closest to the beam axis with a parabolic function. This is shown for the corrugation around the C side of VELO station 8 in figure 2.8 (b). The maximum deposition value in 1 mm length of the RF foil is then divided by the RF foil thickness of  $d_{\text{RF}} = 0.2 \text{ mm}$ . This results in a value of  $\Delta Q_{40}$  of:

$$\Delta Q_{40,\text{RF},2} = 277.85 \text{ MeV mm}^{-3}. \quad (2.4)$$

The difference between the results, obtained with the two methods in nominal conditions, is assigned as a systematic uncertainty to the value of  $\Delta Q_{40}$  and amounts to 8%.

For the VELO sensors  $\Delta Q_{40}$  has been determined only for the Run III dataset, since the VELO sensors of the upgraded VELO detector are significantly different to the sensors used during Run I and Run II. For the RF foil  $\Delta Q_{40}$  is calculated for all three simulation samples. For the Run I and Run II dataset however the method has been slightly modified, due to the different geometry description of the RF foil, as can be seen by comparing figures 2.9 (a) and 2.9 (b). The parabolic function used to fit the RF shape is simply replaced by a constant, as only the innermost region is of relevance. All the determined values are summarised in table 2.3.

**Table 2.3:** The property  $\Delta Q_{40}$  for the different simulation datasets. A systematic uncertainty of 8% is assumed on the results.

Detector component	MC sample	$\Delta Q_{40}$ [MeV mm <sup>-3</sup> ]
Sensors	Run III	108.41
RF foil	Run III	277.85
RF foil	Run II	27.83
RF foil	Run I	14.06

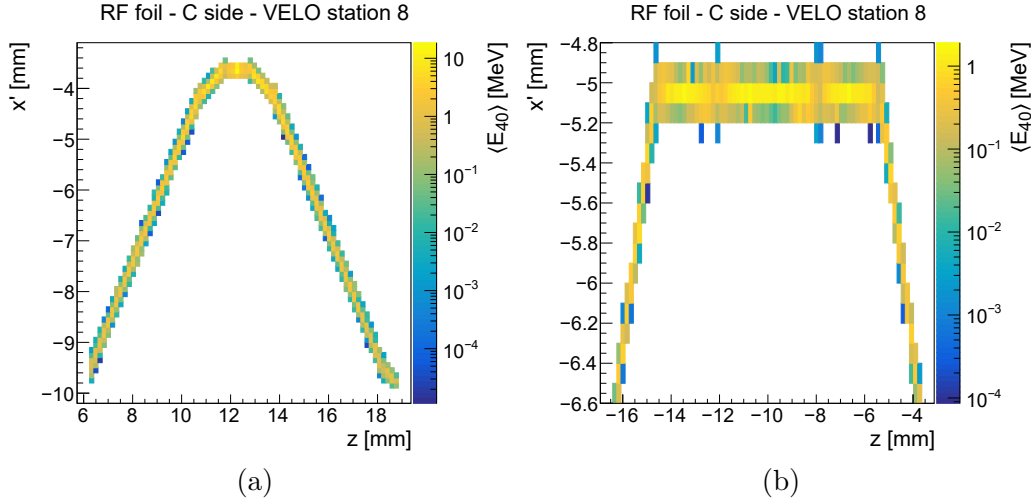


**Figure 2.9:** The mean energy deposition per  $40 \mu\text{s}$   $\langle E_{40} \rangle$  in the RF foil projected onto the  $z$ - $x'$  plane at  $y' = 0 \text{ mm}$  for the C side of VELO station 8 for the Run III dataset (a) and the Run II dataset (b).

The consistency between the obtained values for  $\Delta Q_{40}$  between the generated MC samples is evaluated for the RF foil, by taking into account the following factors: the instantaneous luminosity  $L_{\text{inst}}$ , the minimal radial distance of the RF foil to the beam axis  $r_{\text{RF},\text{min}}$ , and the beam energy  $E_{\text{beam}}$ . The values are summarised in table 2.4.

**Table 2.4:** The instantaneous luminosity  $L_{\text{inst}}$ , the minimal radial distance of the RF foil to the beam axis  $r_{\text{RF},\text{min}}$ , and the beam energy  $E_{\text{beam}}$  for the different data samples.

	Run I (2011)	Run II (2018)	Run III
$L_{\text{inst}}$	$2 \times 10^{32} \text{ cm}^{-2} \text{ s}^{-1}$	$4 \times 10^{32} \text{ cm}^{-2} \text{ s}^{-1}$	$2 \times 10^{33} \text{ cm}^{-2} \text{ s}^{-1}$
$r_{\text{RF},\text{min}}$	5 mm	5 mm	3.5 mm
$E_{\text{beam}}$	3.5 TeV	6.5 TeV	7 TeV

The instantaneous luminosity is directly proportional to  $\Delta Q_{40}$ . This means from the luminosity alone an increase by a factor of  $s_{\text{lumi}1,2} = 2$  is expected between the Run I and the Run II dataset and a factor of  $s_{\text{lumi}2,3} = 5$  between the Run II and the Run III dataset.

The dependency of  $\Delta Q_{40}$  on  $r_{\text{RF},\text{min}}$  and  $E_{\text{beam}}$  cannot be determined directly. Therefore, additional simulations are performed to study their influence. Between the Run I and the Run II dataset  $r_{\text{RF},\text{min}}$  does not change, thus no influence on  $\Delta Q_{40}$  is expected resulting in the factor  $s_{\text{rad}1,2} = 1$ .

The value of  $r_{\text{RF},\text{min}}$  does however change between the Run II and the Run III dataset. The dependency is determined by recalculating the value of  $\Delta Q_{40}$  for the Run III dataset, but considering only the energy deposited at and beyond a minimal radial distance to the beam axis larger than  $r_{\text{RF},\text{min}} = 5$  mm. This gives the value for  $\Delta Q_{40}$  under Run III conditions, but with the  $r_{\text{RF},\text{min}}$  from the Run II dataset:

$$\Delta Q_{40,\text{RF},3} = 147.94 \text{ MeV mm}^{-3}. \quad (2.5)$$

Comparing this with the value of  $\Delta Q_{40}$  for the Run III dataset from table 2.3 a factor of approximately  $s_{\text{rad},2,3} = 2$  is determined, considering the uncertainty on  $\Delta Q_{40}$  of 8%.

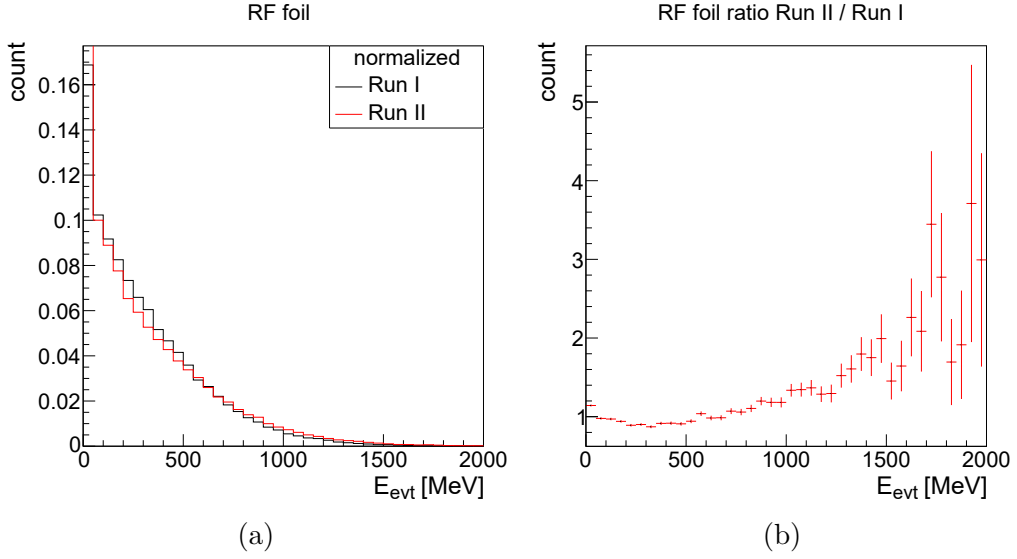


**Figure 2.10:** The energy deposition per event  $E_{\text{evt}}$  in the RF foil for the Run I and Run II dataset (a) and the ratio between the histograms (b).

The factor for the increased beam energy is determined by comparing the per event energy deposition in the RF foil between the Run I and the Run II dataset. This is shown in Figure 2.10 (a). The histograms are normalised due to the different number of generated events in the MC samples. Figure 2.10 (b) shows the ratio between the distribution of the Run II dataset and the Run I dataset.

The ratio is approximately one for most of the events, while a significant deviation from one only occurs above per event deposition values of 1000 MeV. The number of events with a deposition per event larger than this value is negligible, considering  $\Delta Q_{40}$  is integrated over 40  $\mu\text{s}$ . This results in the factor  $s_{\text{energy}} = 1$  between all datasets.

The scaling factors are summarised in table 2.5. Taking all the factors into account an increase in the deposition of a factor two is expected between the Run I and the Run II dataset and a factor of ten between the Run II and Run III dataset. This is in agreement with the values of  $\Delta Q_{40}$  for the RF foil from table 2.3.

**Table 2.5:** The determined scaling factors for the instantaneous luminosity ( $s_{\text{lumi}}$ ), the minimal radial distance of the RF foil to the beam axis ( $s_{\text{rad}}$ ), and the beam energy ( $s_{\text{energy}}$ ), as well as the combined total scaling factors ( $s_{\text{total}}$ ).

	$s_{\text{lumi}}$	$s_{\text{rad}}$	$s_{\text{energy}}$	$s_{\text{total}}$
Run I - Run II	2	1	1	2
Run II - Run III	5	2	1	10

### 2.3.5 Correlation between the detectors

The decision to dump the beam is based on the BCM currents. It is thus important that the signal response of the BCM stations is correlated to the response of the VELO sensors. The correlation between the energy deposition in the BCM stations and the VELO sensors under nominal conditions can be seen from figure 2.11. The correlation between the BCM energy deposition and the RF foil is similar.

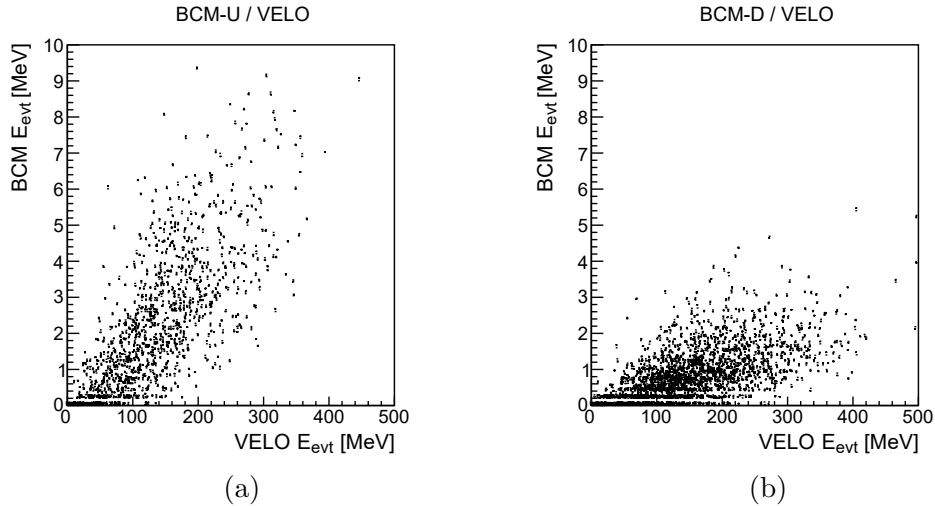


**Figure 2.11:** The energy deposition per event  $E_{\text{evt}}$  in the BCM-U station (a) and the BCM-D station (b) as a function of the corresponding energy deposition of the same event in the VELO sensors.

For each event in the simulation the energy deposition in the BCM stations is studied as a function of the corresponding energy deposition in the VELO sensors. The simulation shows a visible correlation between the BCM stations and the VELO sensors. For higher energy the spread increases, due to the limited amounts of events with a deposition in that energy region and the kinematics of the event. A fairly linear behaviour is observed between the response of the two detectors, making the BCM suitable to initiate a beam dump based on its response.

### 2.3.6 Determination of currents

The energy deposition has been studied in detail and the correlation between the detectors has been verified. In this section the expected currents for the BCM sensors are determined from the simulation.

Using the method from section 2.3.3 the energy deposition in the individual sensors of the BCM stations is determined. This is shown in figure 2.12 (a). Each sensor of the BCM is assigned to a unique sensor ID: the sensor IDs from 0 to 7 are assigned to the BCM-U sensors and the sensor IDs from 8 to 15 are assigned to the BCM-D sensors.

The energy deposited is nearly the same between the sensors of one station, as expected from the occupancy studies. In Figure 2.12 (b) the values are converted to a current value  $I$  [33]:

$$I = \frac{\langle E_{40,i} \rangle}{40 \mu\text{s}} \frac{e}{13 \text{ eV}}, \quad (2.6)$$

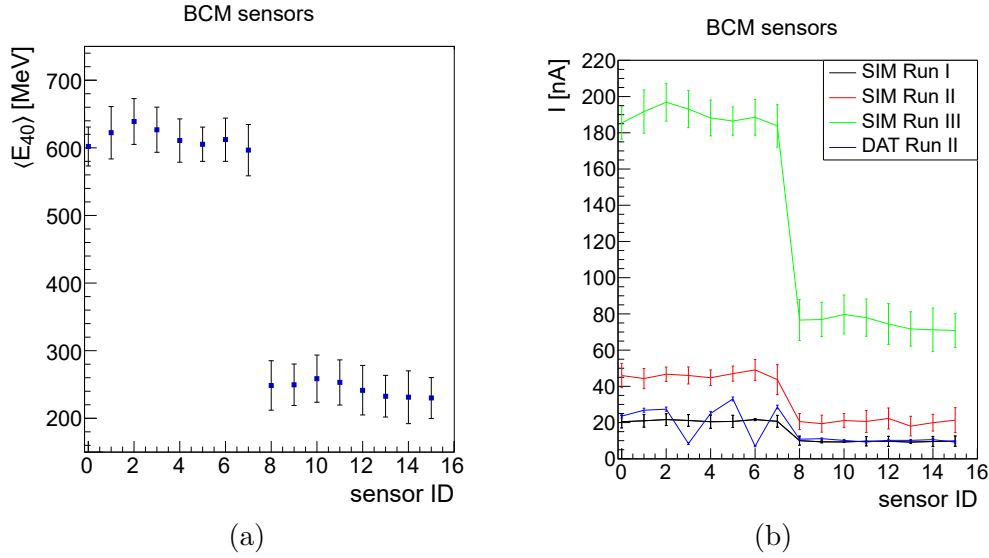
where  $\langle E_{40,i} \rangle$  is the mean energy deposition per 40  $\mu\text{s}$  in sensor  $i$ ,  $e$  is the electrical charge in coulomb and the energy needed to generate an electron-hole pair in a diamond sensor is 13 eV [34].

Figure 2.12 (b) shows the current values for the simulated datasets (SIM), as well as the measured average current values during a fill in November 2018 (DAT). The DAT values are extracted from the LbECSDData system [35].

The measured currents are all below the corresponding simulation values. This is because for the simulation a charge collection efficiency of 100 % is assumed, where in reality an efficiency of around 70 % is expected. Additionally the efficiency of the sensors decreases over their lifespan due to radiation damage [19, 33]. It can be noted, that two of the diamond sensors of the BCM-U station are performing worse compared to the other sensors. Despite the factor two difference, the simulation is considered reliable enough for the evaluation of the BCM thresholds for Run III.

The resulting mean current values of the individual stations for the SIM and DAT datasets are summarised in table 2.6. The mean expected currents for Run III are around a factor of four larger compared to the Run II values.





**Figure 2.12:** The mean energy deposition per 40  $\mu\text{s}$   $\langle E_{40} \rangle$  in the BCM sensors for the Run III dataset (a) and the current values for all simulated datasets (SIM), as well as for the Run II data from 2018 (DAT) (b), as a function of the BCM sensor ID. The lines in figure (b) are inserted to guide the eye and have no physical meaning.

**Table 2.6:** The determined current values from simulation for both BCM stations. The values for DAT from 2018 are listed in brackets behind the Run II SIM values.

	Station	Run I [nA]	Run II [nA]	Run III [nA]
SIM (DAT)	BCM-U	20	46 (22)	189
SIM (DAT)	BCM-D	9	20 (10)	75

### 2.3.7 New thresholds

Based on the currents expected from simulation the new thresholds for the beam dump logic are proposed. The thresholds need to be set high enough to not wrongly trigger a beam dump, but at the same time need to be as low as possible to best protect the detector. The thresholds used during Run I and Run II, as well as the new proposed thresholds are listed in table 2.7.

## 2 Run III simulation of the Beam Conditions Monitor

---

**Table 2.7:** The applied thresholds (appl. thr.), and proposed thresholds (prop. thr.) for Run III in  $\mu\text{A}$  and in ADC values. The thresholds depend on the RS, the BCM station, and the operation mode.

	station	mode	appl. thr. [ $\mu\text{A}$ ]	prop. thr. [ $\mu\text{A}$ ]	prop. thr. [ADC]
RS1	BCM-U	0	10.1	40.4	8148
		3	20.2	80.8	10290
	BCM-D	0	2.6	10.4	2148
		3	7.8	31.2	63D8
RS2	BCM-U	0	10.1	40.4	8148
		3	2560	2560	1ffff
	BCM-D	0	2.6	10.4	2148
		3	2560	2560	1ffff
RS32	BCM-U	0	64.64	258.56	33B65
		3	64.64	258.56	33B65
	BCM-D	0	16.64	66.56	D4FE
		3	16.64	66.56	D4FE
RS32-SUM	BCM-U	0	323.2	1292.8	1028F6
		3	323.2	1292.8	1028F6
	BCM-D	0	83.2	332.8	428F6
		3	83.2	332.8	428F6

The first column of the table specifies the RS on which the threshold is set. The thresholds are different based on the BCM station and the operation mode. The thresholds of the RS2 mode 3 (injection mode) are set to a high value that corresponds to no threshold. The column for the applied threshold (appl. thr.) shows the thresholds that were set during Run I and Run II. These thresholds were originally calculated by setting their values to multiples of the mean currents determined by simulations [29].

The new proposed thresholds (prop. thr.) are given in the right columns and are set a factor four higher than the corresponding thresholds in Run II. This reflects the increase in corresponding expected currents, as seen in table 2.6. The proposed thresholds are additionally converted in Analogue Digital Count (ADC) hexadecimal values. There are 4096 counts for every  $5\mu\text{A}$ . The ADC values are the ones written in the firmware. With these proposed thresholds, the probability of wrongly triggering a beam dump under nominal conditions has been evaluated over the typical timespan of a fill and found to be negligible.

## 2.4 Detector response under adverse beam conditions

It is also crucial to investigate the BCM response in critical beam scenarios, such as beam scraping, where the beam drifts away from its nominal position and starts to scrape on the surrounding detectors. The detector that is again most affected in this case is the VELO, since it has the smallest aperture in the LHCb detector. It is the goal of the BCM to dump the beam before the beam drifts too far from its nominal position and starts to damage the sensitive detector parts. In this section the effectiveness of the new proposed thresholds is evaluated in this scenario.

### 2.4.1 Beam scraping simulation

To study the detector response under adverse conditions a beam scraping simulation is performed. The 'Particle Gun' component of 'Gauss' is used, which generates single protons at a given location in the LHCb coordinate system that are then propagated through the detector [29]. The simulation implements the upgraded detector design for Run III.

The two LHC beams are simulated separately. A beam is generated by setting a beam centroid  $(x_0, y_0, z_0)$  with a beam position spread  $\sigma_i$ , as well as a momentum centroid  $(p_{x0}, p_{y0}, p_{z0})$  with a momentum spread  $\sigma_{pi}$ . The position and momentum spread are given by:

$$\sigma_i = \sqrt{\varepsilon_i \beta_i}; i = x, y; \sigma_z = 0, \quad (2.7)$$

$$\sigma_{pi} = \sqrt{\varepsilon_i / \beta_i}; i = x, y; \sigma_{pz} = 0, \quad (2.8)$$

where  $\beta_{x,y}$  is the optical function and  $\varepsilon_{x,y}$  is the transverse emittance in  $x$  and  $y$  direction. The protons are randomly generated from the resulting Gaussian distributions.

For beam 1 the protons are generated at  $z_0 = -22\,180$  mm upstream of the IP, for beam 2 at  $z_0 = 22\,180$  mm downstream of the IP, just in front of the MBXWS compensator dipoles of the LHCb experiment [29]. The components of the momentum along  $x$  and  $y$  are given by:

$$p_{x0} = p_E \cos(\phi) \sin(\theta), \quad (2.9)$$

$$p_{y0} = p_E \sin(\phi) \sin(\theta), \quad (2.10)$$

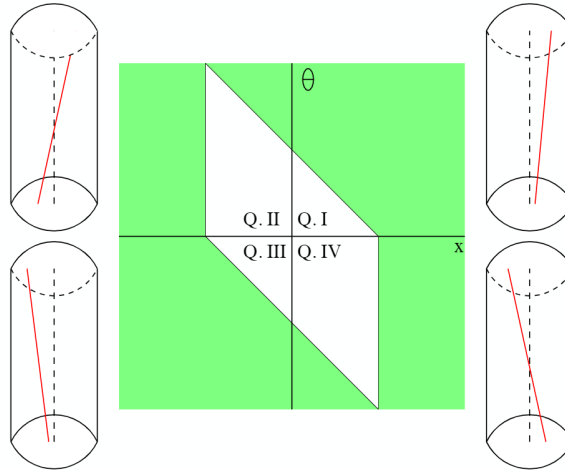
where  $p_E$  is the total momentum of the protons,  $\theta$  is the azimuth angle in the  $x$ - $z$  plane with respect to the beam axis and  $\phi$  is the polar angle around the beam axis. The component of the momentum along  $z$  results in:

$$p_z = \sqrt{p_E^2 - p_x^2 - p_y^2}, \quad (2.11)$$

where  $p_{x,y}$  are the momentum components picked randomly from the Gaussian momentum distribution. The values of  $\beta_{x,y} = 2.79$  m and  $\varepsilon_{x,y} = 5.09 \times 10^{-10}$  m are used. These values correspond to the values given in section 2.3.1. The resulting beams are Gaussian distributed with a total sigma in  $x$  and  $y$  of  $\sigma_{\text{beam}} = 38$   $\mu\text{m}$ .

### 2.4.2 Comparison of the coverage

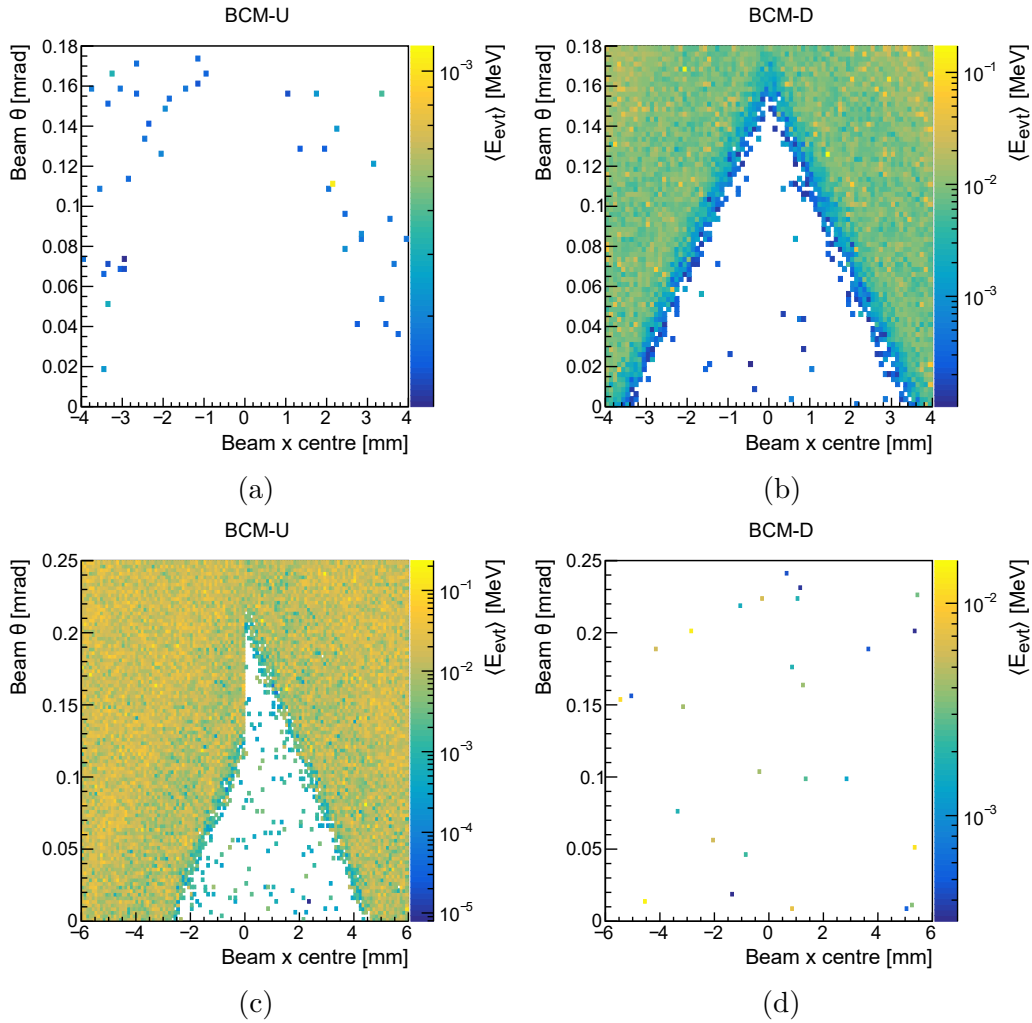
For the purpose of this simulation the protons are generated at fixed location in  $y$ , with  $y_0 = 0$ , and the angle  $\phi$  fixed to zero. A two-dimensional scan is performed in  $x_0$  (beam  $x$  center) and  $\theta$  (beam  $\theta$ ), as the  $x$ - $z$  plane is the bending plane of the magnet. The value of  $x_0$  is varied between  $\pm 7$  mm and the value of  $\theta$  is varied between  $\pm 0.4$  mrad. The value for each observable is taken randomly from a uniform distribution within the given range. A total amount of  $10 \times 10^6$  events is generated.



**Figure 2.13:** Depiction of the coverage of a detector when varying  $x$  and  $\theta$ . The green area is the sensitive area, the white area the blind area. Adopted from reference [29]

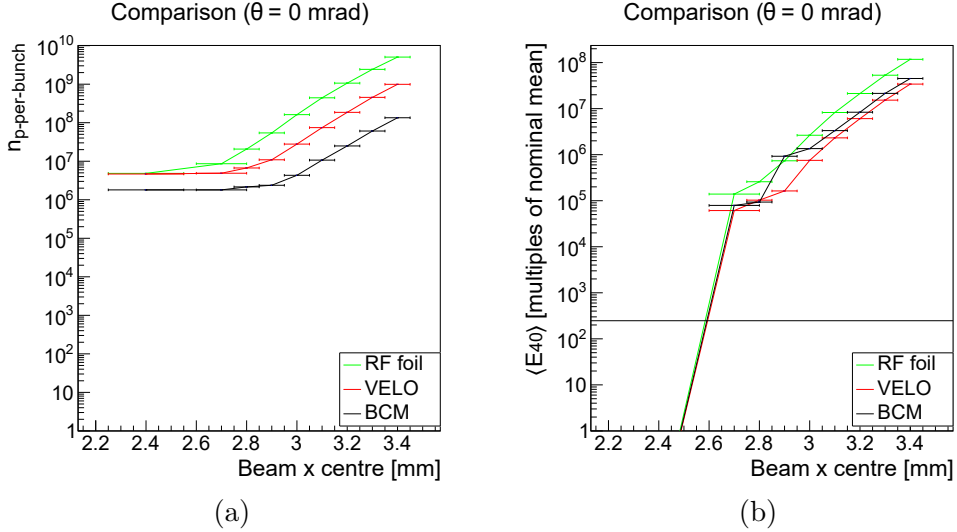
The coverage of a detector in the  $x$ - $\theta$  plane is schematically depicted in figure 2.13. The green areas represent the sensitive regions of the detector, while the white areas represent the blind regions of the detector, where no signal is detected. Only quadrants Q. I and Q. III from figure 2.13 are considered, since they cover the full range in  $x$  and the other two quadrants only add redundant information.

Figure 2.14 shows the coverage of the BCM-U and BCM-D stations obtained from the simulation, separately for beam 1 and beam 2. The absolute value of  $\theta$  is shown as a function of the beam centre in  $x$ . This corresponds to flipping the quadrant Q. III of figure 2.13 around the horizontal axis, with the result that the blind area assumes a triangular shape. On the  $z$  axis is the mean energy deposited per event  $\langle E_{\text{evt}} \rangle$  in the BCM stations, scaled such that every bin corresponds to one generated proton.



**Figure 2.14:** The coverage of the BCM for beam 1 of the BCM-U station (a), for beam 1 of the BCM-D station (b), for beam 2 of the BCM-U station (c), and for beam 2 of the BCM-D station (d). On the  $z$  axis is the mean energy deposited per event  $\langle E_{\text{evt}} \rangle$ .

For beam 1 a signal is observed in the BCM-D station; for beam 2 in the BCM-U station. This is due to the beam direction and the opening angle of the generated beams. There are some hits noticeable in the detectors where no signal is expected, as well as in the blind areas of the detectors. This can be explained by backscattering of the protons and an imperfection in the description of the vacuum near the IP, that causes random noise [29]. In the following the noise is removed from the plots. The protons of beam 2 pass through the magnet field before hitting the BCM-U station. Depending on the magnet polarisation this leads to a shift in  $x_0$  either in positive or negative direction. In the magnet down configuration used for the simulation the border of the coverage assumes a lambda shape, as can be seen in figure 2.14 (c). From this point onward the focus lies on beam 1, where only the BCM-D station is of relevance. The study has been repeated for beam2. Firstly, the coverage of the BCM-D station is compared to the one of the VELO sensors and the RF foil at  $\theta = 0$ . High statistic samples have been generated for values of beam centre  $x_0 < 3.5$  mm, with  $5 \times 10^6$  events each.



**Figure 2.15:** Number of protons per bunch  $n_{p\text{-per-bunch}}$  directly or indirectly producing hits in the respective detector components (a) and the scaled mean energy deposition per 40  $\mu\text{s}$  ( $\langle E_{40} \rangle$ ) normalised to the nominal mean energy deposition per 40  $\mu\text{s}$  (b), as a function of the beam centre in  $x$ .

Figure 2.15 (a) shows the number of protons per bunch  $n_{p\text{-per-bunch}}$  directly or indirectly producing hits in the respective detector components as a function of the beam centre in  $x$ . For reference, the total number of protons per bunch is  $2.2 \times 10^{11}$  [27]. The trend is comparable between the three components, with a larger number of particles hitting the RF foil, followed by the VELO sensors and finally the BCM-D station. This is reasonable, since the BCM detector mostly

detects secondary particles that are created after interaction with the RF foil material. Despite this, whenever a signal is registered in the RF foil or the VELO sensors, a signal is also registered in the BCM.

In figure 2.15 (b) the mean energy deposition per proton is scaled to the mean energy deposition per 40  $\mu\text{s}$ , according to the scale factor  $s_{40}$ :

$$s_{40} = n_{\text{p-per-bunch}} n_{\text{bunches}} f_{\text{bunch}} 40 \mu\text{s}, \quad (2.12)$$

where the number of bunches of a filled beam is  $n_{\text{bunches}} = 2748$  and the circulation frequency of a bunch is  $f_{\text{bunch}} = 11\,245 \text{ Hz}$  [27]. Due to  $n_{\text{p-per-bunch}}$ , the scale factor  $s_{40}$  is dependent on the position of the beam centre in  $x$  and the detector component, as indicated by figure 2.15 (a).

To better compare the trends, the scaled mean energy deposition per 40  $\mu\text{s}$  is normalised to the nominal mean energy deposition per 40  $\mu\text{s}$ , using the values of  $\langle E_{40} \rangle$  from table 2.2. The proposed BCM threshold for RS32-SUM from section 2.3.7 is converted to the same unit, indicated by the horizontal black line. The beam would be dumped after the signal exceeds the threshold. The position of the beam  $x$  centre where this is the case is  $x_{\text{thresh}} = 2.6 \text{ mm}$ .

In figure 2.16 (a) to (c) the coverage of the detectors has also been investigated in the  $x$ - $\theta$  plane, however due to the limited sample sizes there is a region around the border of the coverage where the uncertainty on the energy deposited is significant. This is indicated by a coloured band for the BCM-D (black), the VELO sensors (red) and the RF foil (green), respectively. The lower border of the bands is determined for  $\theta = 0$  from figure 2.15 (b). The boundaries of the bands at  $\theta = 0$  for the individual detector components are listed in table 2.8. Since for beam 1 the coverage is symmetric in  $x$ , the absolute value of the beam centre in  $x$  is displayed.

To further visualise and compare the coverage of the detector components the bands are overlapped in figure 2.16 (d). Considering the statistical uncertainty on the border of the detector coverages, it can be concluded, that the energy deposited in the VELO sensors and RF foil corresponds to an increase in the energy deposited in the BCM to a sufficient amount, so that the BCM can act as a safety measure and protect the VELO components.

**Table 2.8:** The boundaries  $x_1$  and  $x_2$  for the beam centre in  $x$  for the band representing the statistical uncertainty at  $\theta = 0$ , and the resulting band width  $d_{\text{band}}$ . For the BCM-D station additionally the location for the beam centre in  $x$  is listed, where the threshold for RS32-SUM is exceeded.

Detector component	$x_1$ [mm]	$x_2$ [mm]	$d_{\text{band}}$ [mm]	$x_{\text{thresh}}$ [mm]
BCM-D	2.5	3.3	0.7	2.6
Sensors	2.5	3.1	0.5	-
RF foil	2.5	2.9	0.3	-

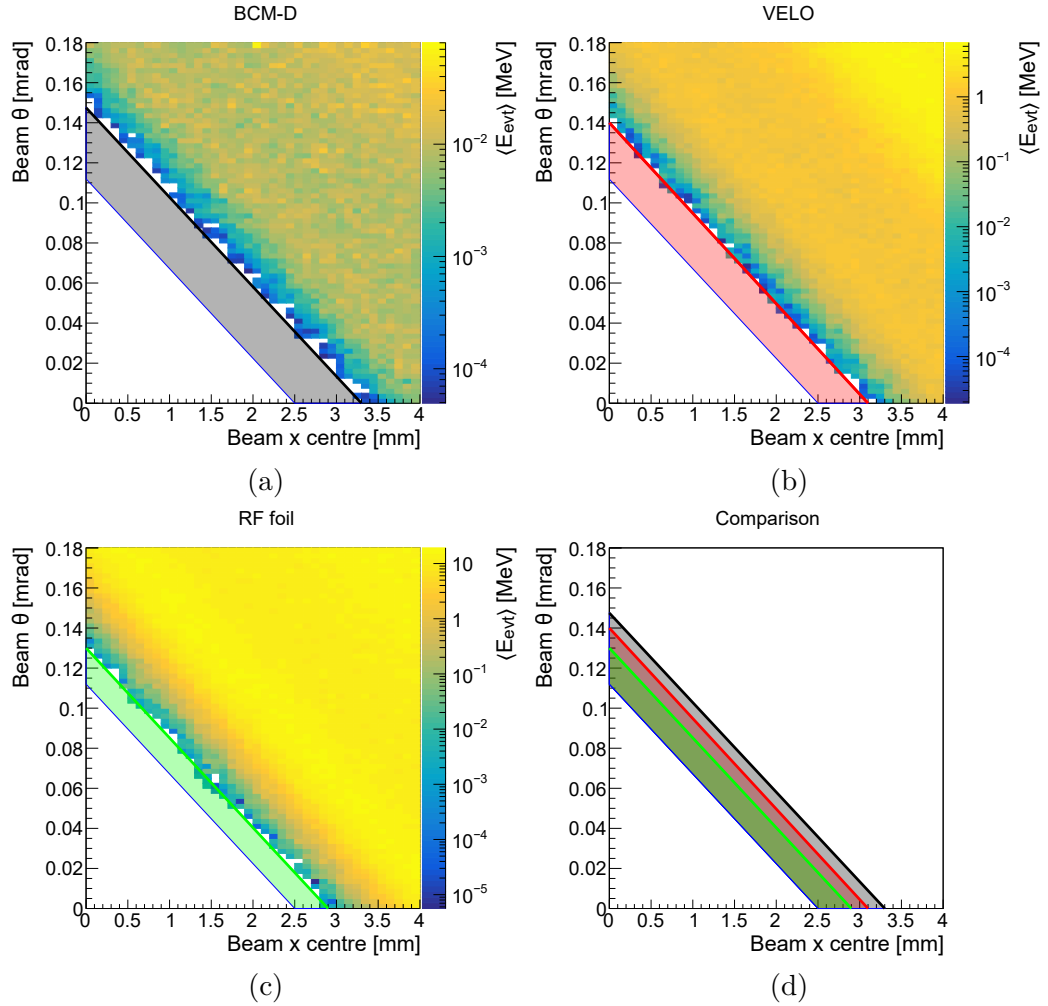


**Figure 2.16:** The coverage for beam 1 of the BCM-D station (a), the VELO sensors (b), and the RF foil (c). On the  $z$  axis is the mean energy deposited per event  $\langle E_{\text{evt}} \rangle$ . The bands along the border of the coverage indicate the uncertainty due to the limited size of the data sample. In figure (d) the bands of the three detector components are compared.



### 2.4.3 RF foil temperature estimation

Before the beam gets dumped by the BCM, the RF foil and the VELO sensors are exposed to increased radiation. In this section an estimation of the expected worst case increase of the RF foil temperature in the time period leading up to the beam dump is performed.

Only the relevant region around the border of the BCM coverage is considered, in order to reduce the computation time. Of relevance is the maximum temperature increase  $\Delta T_{40}$  in the BCM integration time of 40  $\mu\text{s}$ . The maximum energy deposition per volume  $\Delta Q_{40}$  is determined over the second procedure described in section 2.3.4 and then converted into a temperature increase:

$$\Delta T_{40} = \frac{\Delta Q_{40}}{\rho c_V}, \quad (2.13)$$

where  $\rho = 2.700 \text{ g cm}^{-3}$  [36] is the material density and  $c_V = 910 \text{ J kg}^{-1} \text{ K}^{-1}$  [37] is the specific heat capacity for aluminium. The temperature increase depends on the origin  $x_0$  and  $\theta$  of the generated protons. The procedure is thus applied for each of the bins in the selected region individually, by generating a dedicated simulation sample per bin. Figure 2.17 (a) depicts the maximum temperature increase  $\Delta T_{40}$  for the RF foil in the relevant region. Figure 2.17 (b) corresponds to a slice through the plot at  $\theta = 0$ .

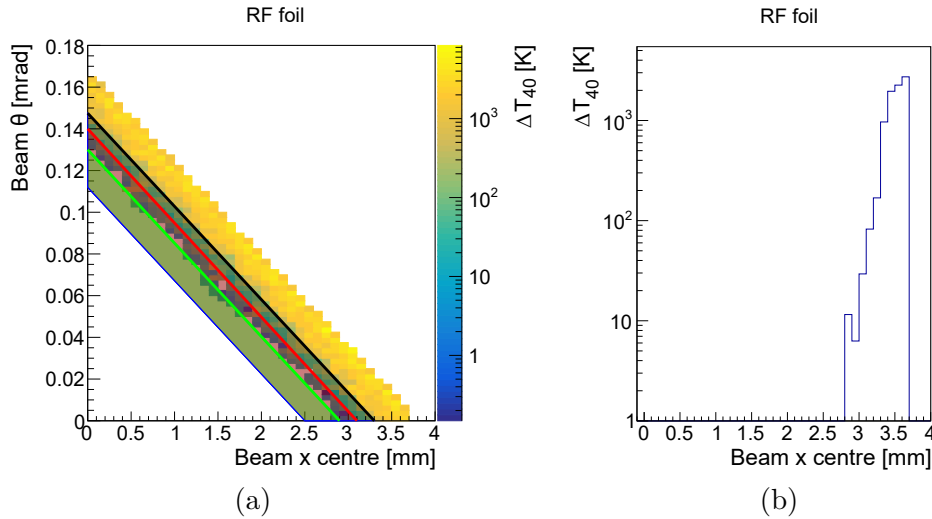


**Figure 2.17:** The worst case increase in temperature per 40  $\mu\text{s}$   $\Delta T_{40}$  (a) and a slice at  $\theta = 0$ . In figure (a) the coloured bands correspond to the border of the coverage of the BCM (black), the VELO sensors (red), and the RF foil (green).

Referring back to the boundaries of the BCM band at  $\theta = 0$  from table 2.8 and taking into account the change in the order of magnitude of the energy deposition seen in this region from figure 2.15 (b), the order of magnitude of  $\Delta T_{40}$  at the location  $x_{\text{thresh}} = 2.6$  mm, where the beam would be dumped by the BCM, is extracted from the plots to:

$$\Delta T_{40,\text{thresh}} \sim 0.01 \text{ K.} \quad (2.14)$$

Considering that no beam drifting or dissipation of the temperature is taken into account, the BCM is expected to successfully dump the beam before any damage to the detector occurs.

#### 2.4.4 Beam 2 beam scraping

The same beam scraping studies have been performed for beam 2. Here the BCM-U station is of relevance. Because the particles are crossing the magnetic field before hitting the BCM-U station a shift in  $x_0$  is observed. Figures of the visible coverage of the detector components can be found in appendix A.3.

The overall behaviour of the coverage is the same as for beam 1. The BCM detector responds to an increase in the deposition of the VELO sensors and the RF foil. In the period leading up to the beam dump an increased exposure to radiation is seen in the RF foil and the VELO sensors. The order of magnitude for the worst temperature increase is expected to be the same as for the beam 1 studies. Therefore, the BCM-U station provides the same protection that is seen for the BCM-D station in case of a critical beam 2 scenario.

## 3 Development of a control system for the Timepix4 telescope

In the second part of this thesis a slow control system for the Timepix4 telescope is developed. The Timepix4 telescope is described in section 3.1. An overview of the slow control system, that was developed specifically for the Timepix4 telescope, is given in section 3.2. The slow control system is divided into multiple subcomponents. The two parts of the slow control system that were developed as part of this thesis are described in section 3.3 and section 3.4.

### 3.1 The Timepix4 telescope

Telescopes are tracking detectors that precisely reconstruct particle tracks using a set of sensor planes. A Device Under Test (DUT), typically a prototype for a detector, is then characterised by comparing its response with the information provided by the telescope.

The Timepix4 telescope [38] is the next generation of beam telescopes, based on the Timepix family of readout ASICs (Application Specific Integrated Circuits). It is the successor to the Timepix3 telescope [39], that used the Timepix3 ASIC. In first iterations of the Timepix4 telescope a mixture of 100 and 300 nm thick sensors will be bonded to the Timepix4 ASIC. The Timepix4 chip, as its predecessor, can simultaneously measure the Time of Arrival (ToA) and the Time over Threshold (ToT) of the particles. The former is related to the timestamp and the latter to the charge collected.

For the Timepix4 ASIC the ToA binning resolution improves from 1.56 ns to 195 ps with respect to the Timepix3 ASIC, and the ToT energy resolution improves from  $< 2$  keV to  $< 1$  keV. This makes it an excellent prototype for future four-dimensional tracking detectors. The main characteristics for the Timepix3 and Timepix4 ASICs are listed in table 3.1.

The Timepix4 telescope will be operated at the SPS test beam facility in the north area of the LHC. The Timepix4 telescope is mainly developed within the LHCb VELO project, however it will also be used for studies on other detectors.

**Table 3.1:** Properties of the Timepix3 and Timepix4 ASIC.

	Timepix3 (2013)	Timepix4 (2019)
Technology	130 nm	65 nm
Pixel size	55×55 μm	55×55 μm
Pixel matrix	256×256	512×448
Sensitive area	1.98 cm <sup>2</sup>	6.94 cm <sup>2</sup>
Event packet	48-bit	64-bit
Max rate	0.43 × 10 <sup>6</sup> mm <sup>-2</sup> s <sup>-1</sup>	3.58 × 10 <sup>6</sup> mm <sup>-2</sup> s <sup>-1</sup>
Max rate per pixel	1.3 kHz/pixel	10.8 kHz/pixel
ToT energy resolution	<2 keV	<1 keV
ToA binning resolution	1.56 ns	195 ps
ToA dynamic range	409.6 μs	1.638 μs
Readout bandwidth	5.12 GB	164 GB
Target global minimum threshold	< 500e <sup>-</sup>	< 500e <sup>-</sup>

### 3.1.1 Layout

A schematic view of the Timepix4 telescope is given in figure 3.1. A right-handed coordinate system is used, where the  $y$  axis points upwards and the  $z$  axis points in the direction of the beam. The telescope consists of two arms with four sensor planes each. Each telescope arm will be enclosed in a dry air-filled container. The sensor planes are water cooled to around 15 °C.

For the Timepix3 telescope the sensor planes were angled around  $x$  and  $y$  with respect to the  $z$  axis to provide optimal charge sharing between the pixels and thus the best spatial resolution. For the Timepix4 telescope the best layout for the spatial resolution is potentially different from the best layout for the time resolution. For the first implementation of the Timepix4 telescope, the two planes with 300 nm thick sensors are angled 9° both in  $x$  and  $y$  direction, while the two planes with 100 nm thick sensors are placed perpendicular to the beam.

The DUT can be mounted at the centre of the telescope, between the telescope arms, referred to as the centre stage. The telescope additionally provides an outer stage, at the back of the telescope, where larger DUTs can be mounted. A vacuum box is available to be installed on the centre stage to test irradiated devices at high bias. In this case, additional cooling is provided by a Peltier element.

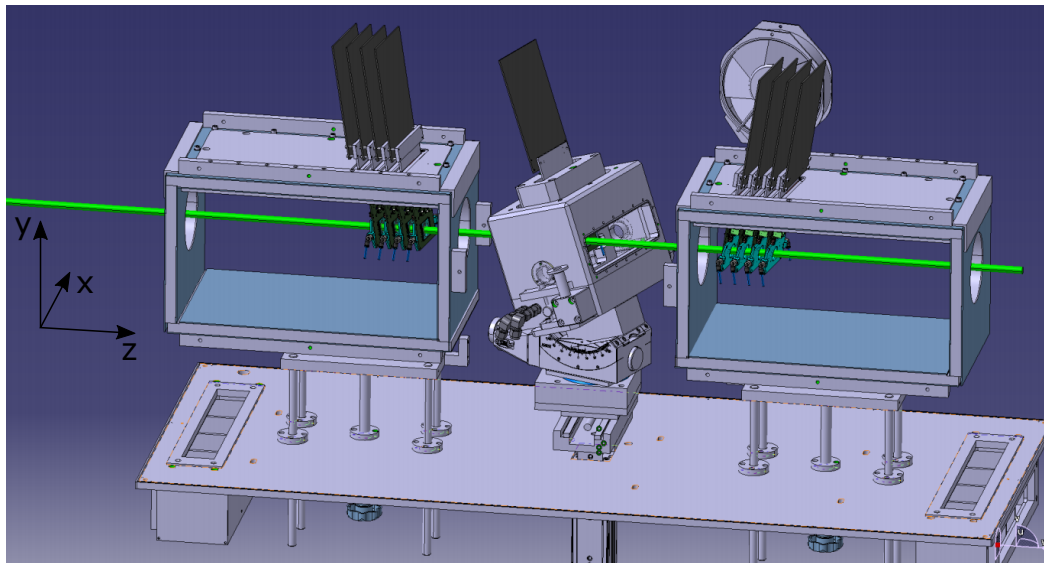


**Figure 3.1:** Schematic of the Timepix4 telescope. Adopted from reference [38].

The main telescope motion stage can be moved in the  $x$  and  $y$  direction to align the telescope with the beam. The telescope arms are mounted on rails allowing for translation along the  $z$  direction increasing or decreasing the distance with respect to the DUT. The DUT translation stage allows to move the DUT in  $x$  and  $y$  direction to perform scans. The DUT is additionally mounted on a rotation stage allowing it to be rotated and tilted around the  $x$  and  $y$  axis. Compared to the Timepix3 telescope this adds an additional degree of freedom for the DUT.

For the Data Acquisition (DAQ) the sensor planes are read out by the fourth generation of Speedy P*IX*el Detector Readout (SPIDR4) boards. With one SPIDR4 board per sensor plane, this results in four SPIDR4 boards per telescope arm. The SPIDR4 board was designed to handle the full bandwidth of  $160 \text{ Gbit s}^{-1}$  of the Timepix4 ASIC.

## 3.2 The slow control system

In this part of the thesis the general aspects of the slow control system are described. Section 3.2.1 gives an overview of the components of the control system. In section 3.2.2 to section 3.2.4 the architecture used to implement the control system is described. Finally, the protocols used to communicate between the software and the hardware are given in section 3.2.5.

### 3.2.1 Overview

The slow control system is used to remotely control the motion stages and power supplies, as well as to monitor the environmental conditions of the Timepix4 telescope. In case of unfavourable conditions, a warning is raised. The monitored data is logged for later analysis. The slow control system is divided into the multiple subcomponents taking care of the individual tasks. A full overview of the slow control components is given in figure 3.2.

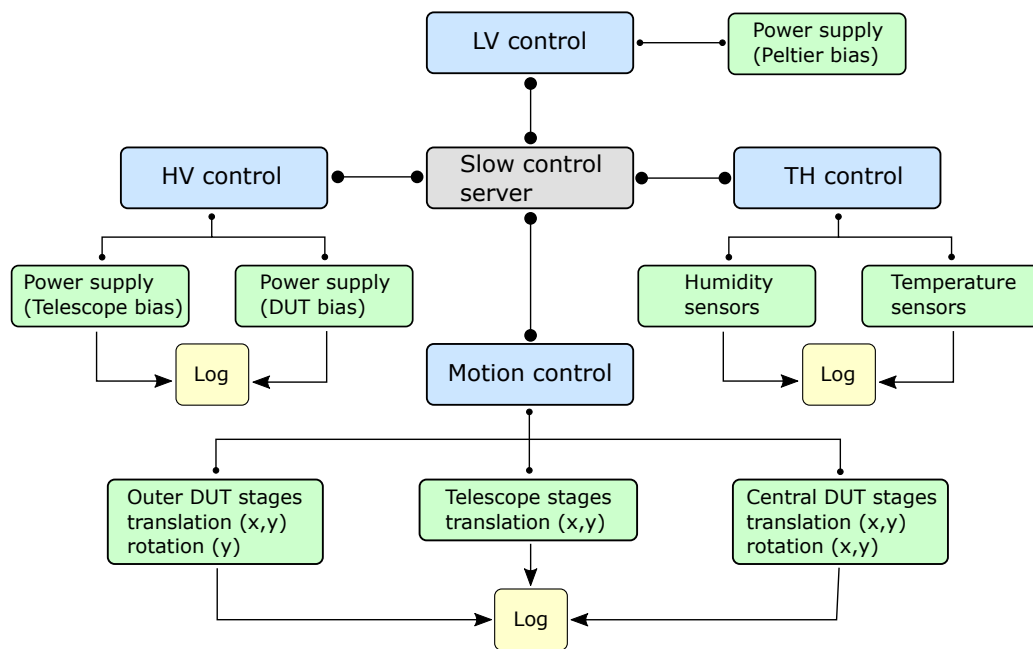


**Figure 3.2:** Schematic overview of the components of the slow control system, including the High Voltage (HV) control, the Low Voltage (LV) control, the Temperature and Humidity (TH) control, and the motion control. Inspired by reference [39].

The High Voltage (HV) control sets and monitors the voltages for the telescope arms and the DUT. The motion control is responsible for the translation and rotation of the telescope stages. The telescope stages include the main translation stage, as well as the centre and outer stages for the translation and rotation of the DUT. The Low Voltage (LV) control will set the voltage for the Peltier cooling element. The Temperature and Humidity (TH) control is responsible for monitoring the temperature of the telescope sensors, the temperature of the DUT, as well as the temperature and humidity inside the boxes enclosing the telescope arms and the DUT.

In the course of this thesis the HV and the TH control have been implemented and tested. The structure of the implemented control systems can be distinguished into three major parts: the hardware, the User Interface (UI), and the drivers and software used to interface between the two. They will be described in detail for both subcomponents in their respective section. The slow control project is set up on a single dedicated machine. For the operating system CERN CentOS 7 (CC7) is used. It is based on CentOS 7 and is one of the main operating systems used at CERN [40, 41].

### 3.2.2 WinCC OA and the JCOP framework

The WinCC Open Architecture (WinCC OA) software suite [42, 43] is used to build the control system. WinCC OA is widely adopted across CERN [44]. This allows for a similar look and feel for the operators across the experiments. It also removes the need to reimplement standard procedures as they can be implemented in separate components that are then shared between different projects. The group that manages these components is the Joint COntrols Project (JCOP) group [45]. The framework is consequently referred to as the JCOP framework [43, 46]. Components are included into a project over a framework installation tool [47]. It is installed individually for each project and allows for easy management of the JCOP components.

WinCC OA is based on a Data Point (DP) system. This allows and provides capabilities for device description and access by setting and reading from DP elements, alarm handling by monitoring said DP elements, as well as archiving and logging of the DP element values. WinCC OA provides the components to build the UI that will display the DP element values and allows interaction with the operator over the use of graphical widgets like text fields or buttons. The resulting UI is referred to as the operator panel.

WinCC OA operates on an event basis using managers. Usually, the events are triggered by user input or changes in the DP elements, however timed execution is also possible. There are four layers of managers: the driver layer, the communication and memory layer, the processing layer and the UI layer. The managers are shown

in figure 3.3. The driver layer includes the Driver (D) managers, that handle the communication with the hardware. This allows to read and set the DP element values from the hardware side.

The data exchange between the managers is event driven. This is handled by the Event (EV) manager in the communication and memory layer. It can be seen as the main manager. In the same layer is the Database (DB) manager. Its task is to manage and store the DP values in a database. This is done by exporting the data at a fixed time specified in the DB options.

The processing layer handles the execution of scripts over Control (CTRL) managers. They are executed over events handled by the EV manager. The scripts are working with a C like syntax. When triggered the code is sequentially executed. It is possible to execute multiple CTRL managers at the same time, as all the managers are started in their own thread. The Application Programming Interface (API) manager allows to include external libraries into the project.

The last layer is the UI layer. It is responsible for the graphical representation. Here all the panels and UI actions are implemented using UI managers, which execute the scripts behind the individual widgets.

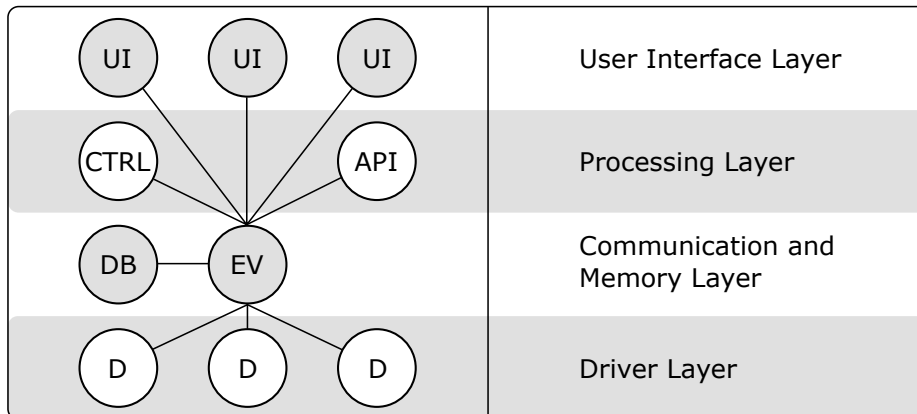


**Figure 3.3:** Schematic overview of the WinCC OA manager layers and managers. Based on reference [43].



When creating a project, a system type can be specified. It is distinguished between a single system, a scattered system and a redundant system. The system types in their distributed form are summarised in figure 3.4.

For the single system everything is set up on a single machine. The operator will use this machine to communicate with the hardware. For the scattered system the main project is set up on a server and the user interface is scattered to multiple operator devices that will communicate with the server over the event manager. The server can spread the processing load. The redundant system is an extension of the scattered system. In this case a second server is set up as a clone of the first server. In case of a failure of the primary server the project will automatically switch to the secondary server. The redundancy is handled by a Redundancy (REDU) manager. Additionally, the project can be set up as a distributed system. This will add a Distribution (DIST) manager to the project. It allows to interchange data between multiple autonomous systems.

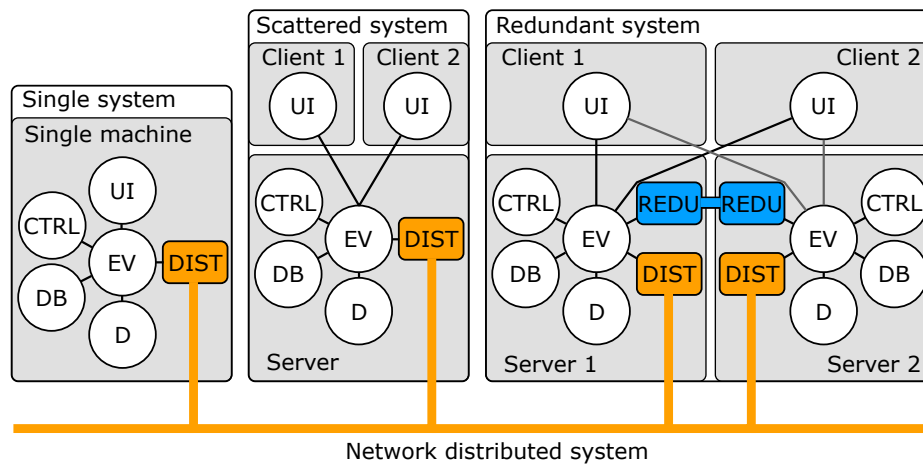


**Figure 3.4:** Schematic overview of the WinCC OA system types: the single system, the scattered system, the redundant system, and the distributed system. Based on reference [43].

Because the slow control project is running on a dedicated machine, the project is set up as a single distributed system. The distribution capabilities are not strictly necessary; however, this allows for easy integration into a larger distributed network should this become necessary at a later point.

The individual components of the slow control system are developed as individual WinCC OA projects to simplify the development process. The completed components are then merged into a main project. This approach also allows to develop and test the subcomponents without directly affecting the main project.

### 3.2.3 Alarm handling

To guarantee safe operations of the detector, alarms have been implemented to inform the operator when the values of voltage, current, temperature, and humidity exceed the defined thresholds. In WinCC OA the thresholds are referred to as alarm limits. WinCC OA handles alarms via alarm classes with an assigned priority indicating the severity of the triggered alarm. In the HV control and TH control project two alarm classes are used. The first is the warning class triggered at 80 % of the limit value. The second is the alarm class triggered at the full limit. The alarm classes are assigned to value ranges that are separated by the limits set on the alarm class. The concept is shown on the right side of figure 3.5. There is always a value range required that has the default alarm class assigned, that stands for the good state where no alarm is triggered.

The alarm class includes a colour code for each of the possible states. The possible states for an alarm are `triggered-unacknowledged`, `triggered-acknowledged`, `not-triggered-unacknowledged` and `not-triggered-acknowledged`. The alarm states and the transition between the states is shown on the left side of figure 3.5. The `triggered` state is based on the limit set on the monitored value. The limit can be a fixed value; however, it is possible to set a hysteresis or dead band around the limit to prevent constant triggers of the alarm in case of a fluctuating signal. The alarm can be activated and deactivated by disabling the limit. The `acknowledged` state indicates whether the alarm has been acknowledged by the operator. An alarm can be acknowledged for example over the use of a specified button.

There are three possible transitions between the states. The three transitions are `came`, `went` and `acknowledged`. For each of the transitions a message can be set, or a specific action can be implemented. The limit that specifies `came` and `went` are usually set to the same value but can also be set to different values.

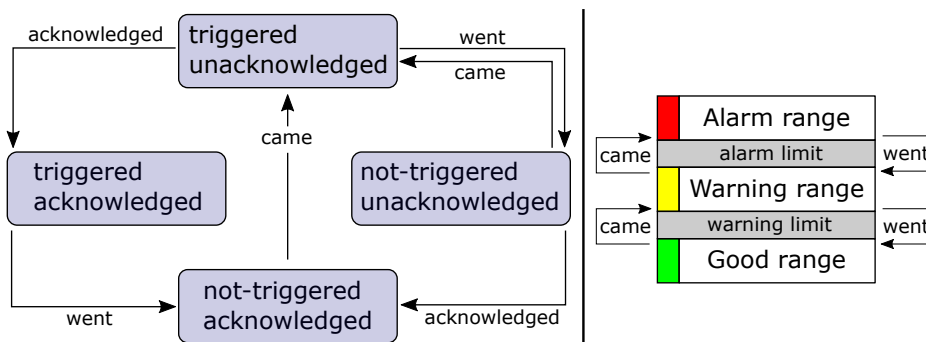


**Figure 3.5:** Visualisation of the alarm handling in WinCC OA. On the left the alarm states are depicted, on the right the alarm ranges are shown. Based on reference [43].

### 3.2.4 Data logging

The values are exported to hard drive at regular intervals. This preserves the information related to the settings and the environmental conditions for future analysis of the data. WinCC OA provides capabilities for data logging, handled by the DB managers. The possible DBs are the RAIMA [48] and the Oracle [49] DB. The RAIMA DB stores the data locally to the disk. Oracle also provides cloud services, that are widely used throughout CERN [43, 50]. For the HV control and the TH control project the RAIMA DB is sufficient. The archives can be configured in WinCC OA to include the specified DP element values. To reduce the data size data smoothing is used. Data smoothing means that not every value is saved to disk. If for example the smoothing is set to only save the data every ten seconds all the changes in between are ignored.

An online and offline backup is used. For each the time interval between the exports and the number of files to be kept is specified. The number of files kept in the online backup is usually limited to a small amount. For the offline backup the data is compressed, and the data can be exported to an external hard drive. The number of files to keep in the offline backup is usually set to a large amount to prevent data loss, as the oldest files are deleted when the number of files specified for the offline backup is exceeded. The offline backup is the final backup location.

For example, assume twelve backup files exist and the number of files specified for the online backup is set to two and the one for the offline backup is set to ten. The two newest backup files are kept for online correction, while the other ten will be compressed and stored to the final offline backup location. Should a new file be created, it will be kept in the online backup, while the oldest file from the online backup will be moved to the offline backup. Since the maximum number of files in the offline backup now exceeds the allowed twelve files the oldest file will be deleted. For the HV and TH control projects, the implemented number of offline backup files is set to the maximum of 9999 files. This means that even when a new backup file is created every day the files will not be deleted within the next 27 years.

WinCC OA stores the data in an internal data format that cannot be easily read out by the operator. To be able to look at the data outside of WinCC OA the data is additionally exported in a human readable format. For this the data is automatically exported in the `.csv` format. The JCOP framework already comes with functionalities supporting that format, that are adapted into a new control script to daily export the data of the previous day.

### 3.2.5 Communication protocols

The communication between WinCC OA and the hardware is based on a server-client basis. The protocols used for this purpose are the OPC Unified Architecture (OPC UA) [51] and the Distributed Information Management (DIM) system [52]. The main concept is visualised in figure 3.6. OPC UA will be used as the communication protocol in the TH project, DIM as the communication protocol in the HV project. The details of the individual protocols will be explained in the respective project, when they become relevant.

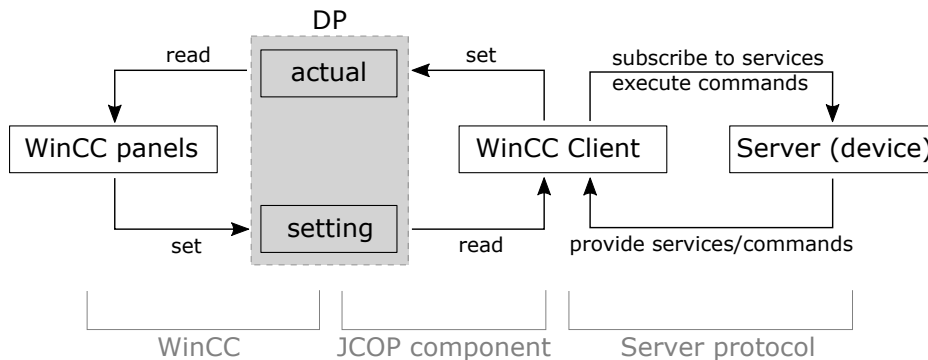


**Figure 3.6:** Visualisation of the communication between the server (device) and WinCC OA via a communication protocol.

The communication protocols are used to read and set the DP elements from the hardware side. The JCOP framework provides packages, that allow to set up WinCC OA as a client or server in the communication the protocol. The server provides services, to which the client can subscribe to, and commands, which the client can execute. Commonly, WinCC OA is set up as the client and the hardware side is set up as the server. The communication to the hardware is done via the drivers. They are the software components specifically written to allow this communication between the hardware and the operating system.

The DP elements defined for the slow control projects have two different attributes: **actual** and **setting**. The **actual** DP elements are intended to represent the actual values of the device. They are displayed on the WinCC OA panels and are set by the WinCC OA client by subscribing to the values of the server. The server will update the values at a fixed time interval by reading them out from the hardware. The **setting** DP elements are set over the WinCC OA panels. They can be used to assign values to the device or request the execution of an action. When the DP element is updated, the value will be read by the WinCC OA client, which in turn will execute a server command, with the DP element value as the argument. A common task for example, is to set the limits of the hardware device.

## 3.3 High Voltage control

The HV control of the slow control system is responsible to control the HV of the telescope planes and the DUT. The functionalities implemented in the HV project include the monitoring, alarm handling, and data logging of the voltage and current values, as well as performing actions, such as setting and ramping of the voltage. In this section the used hardware, the necessary drivers and software, and the UI of the HV project are described.

### 3.3.1 Hardware

A Keithley [53] is a sourcemeter that provides either a voltage or a current value from a source, while monitoring the value of the other source. For the considered use case the voltage is set, while the current is monitored. To use the voltage source the Keithley needs to be powered on and the internal voltage source must be activated. The former must be done manually by pressing the power button at the front of the device, the latter can be done remotely by sending the corresponding command. Afterwards the voltage can be set to its desired value. Usually this is done over a ramping action in steps of fixed size and time to give the current time to stabilise. The final telescope will use of two up to three Keithleys. The final number is not yet determined at the time of this thesis. The HV project is set up for three Keithleys, however it can be operated with a lower quantity of Keithleys connected.

A test setup composed of two Keithleys of the model 2410 [54] and an Agilent 82357B General Purpose Interface Bus (GPIB) interface [55] is used to develop and test the HV project. The setup is shown in figure 3.7. The Keithleys are connected to a dedicated server over the GPIB interface. The distributing Agilent 10833A cable is employed, such that both Keithleys communicate via the same interface. Both Keithleys are set to use the Standard Commands for Programmable Instruments (SCPI) standard for communication and are assigned a unique GPIB address for identification. The SCPI commands are used to perform read and write operations on the Keithleys. During the development phase of the project, additionally the NI-USB-HS and NI-USB-HS+ interfaces from National Instruments (NI) [56] have been tested.

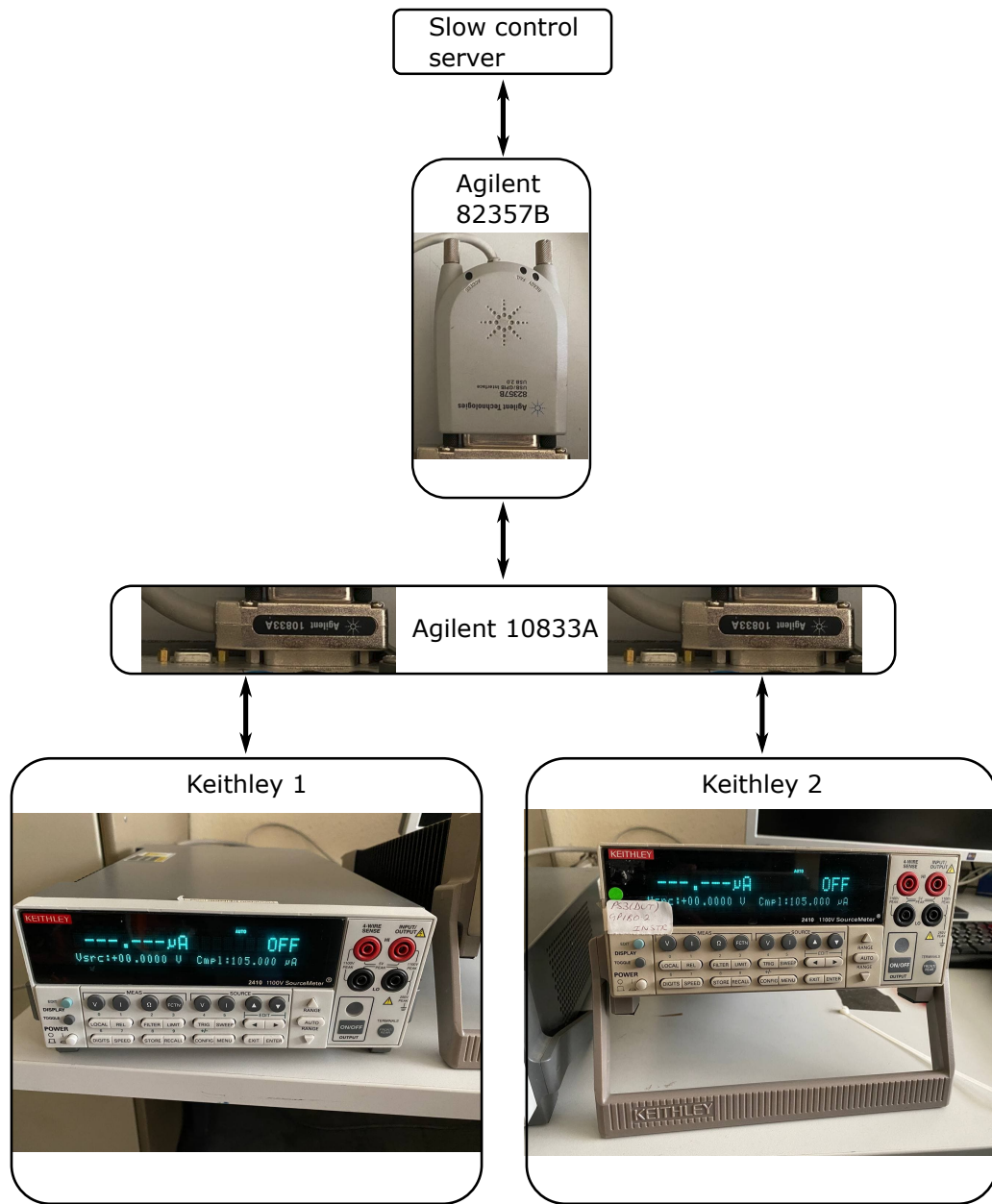


**Figure 3.7:** Schematic of the setup showing the two Keithleys connected to the slow control server via the Agilent 82357B interface. The Agilent 10833A cable distributes the GPIB signal to both Keithleys.

### 3.3.2 Drivers and software

The power supplies are connected to the slow control machine over GPIB interfaces. To establish communication with the hardware drivers are required, as visualised in figure 3.8.

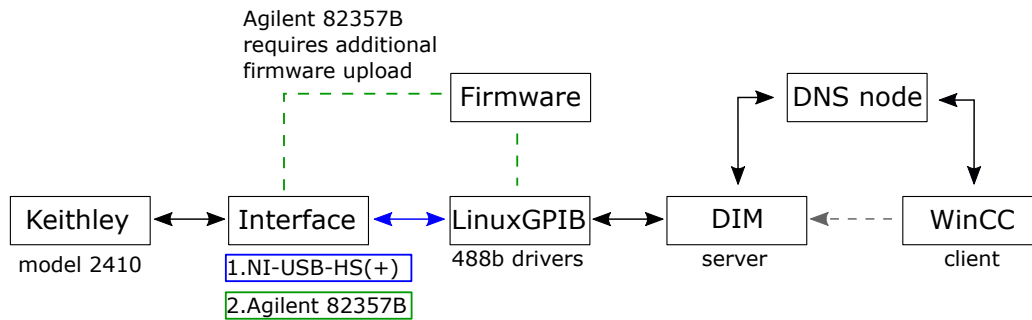


**Figure 3.8:** Visualisation of the drivers used to communicate between WinCC OA and the Keithley. The DIM communication protocol uses the principles described in section 3.2.5.

The slow control project is set up on a CC7 server. For Linux the drivers for the 488b protocol, employed by the interfaces, are provided by the LinuxGPIB [57] project, an open-source project on GitHub [58].

Depending on the interface used a few additional steps are necessary to initialise the interfaces. The NI-USB-HS works out of the box. The NI-USB-HS+ requires a one-time firmware upload the first time it is connected to the server. This is done by plugging the interface into a Windows machine where the NI drivers are installed. Windows will then automatically perform the updated firmware upload. The USB product id is updated from 0x761e to 0x7618. Afterwards the interface can also be used with the LinuxGPIB project. The Agilent interface requires the firmware to be uploaded to the interface each time it is plugged into the computer. The firmware is taken from reference [59]. After successful upload the device id changes from 518 to 718.

The protocol used for the communication with WinCC is DIM. The LinuxGPIB drivers are accessed by the DIM server. The DIM protocol is then, using a Domain Name System (DNS) [60] node that handles the servers and clients, propagating the values retrieved from the hardware to WinCC OA. WinCC OA is used to start and stop the DIM server.

### 3.3.3 DIM server

The server for the DIM protocol is not predefined and needs to be implemented. The main functionalities, services and commands of the server are described in this section. The server is implemented in Python [61] as its own class. The class is inherited from the Thread class of the threading package [62]. This allows the creation of multiple independent servers. The class heavily relies on the PyVISA package [63], the PyDIM package [64], and the asyncio package [65]. The PyVISA package provides the commands, that can be used from within Python, to access the LinuxGPIB drivers via the pyVISA-py backend [66]. In python the device, here the Keithley, is then defined as a resource. The resource is accessed over the GPIB address and among others `write()` and `read()` commands are provided to communicate with the device. Usually data is read from the Keithley by first writing a command that requests the data to be put into the output query that can afterwards be read out by the `read()` command. The `query()` command does this in a single step.

When initialised the server thread is launched in an asynchronous loop. This allows functions to be defined as asynchronous functions. The main loop can create tasks to run multiple of these functions asynchronously at the same time. This method was chosen such that the server does not become unresponsive when executing one of its commands, while avoiding the complications coming with true parallelism. The asyncio package allows for the definition of `Future` objects. These objects monitor the state of an asynchronous function. They are the main feature for flow control of the code. When an asynchronous function is executed, its `Future` object is awaited. The executing function will continue once the state of the `Future` object is `Done`. These `Future` objects can be awaited anywhere in the code making them especially useful when performing `write()` and `read()` operations on the Keithley, as the device can only perform one action at a time.

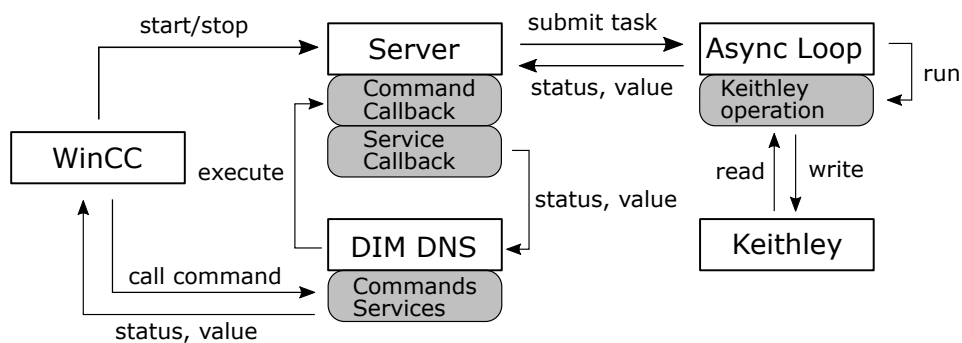


**Figure 3.9:** Schematic of the command execution and reading of values on the server.



If communication with the Keithley cannot be established the server is put into a **Dummy** status. This allows to start the server independent of the power state of the Keithley. The main loop periodically triggers an update function of the server, which is used to read out the current values of the Keithley. It also acts as the heartbeat of the server. Whenever the read operation is successful it will send an **Alive** signal. It is also used to put the server out of the **Dummy** status should the Keithley be powered on after server initialisation. The update interval for the heartbeat is around one second.

The PyDIM package works based on callback functions. Figure 3.9 visualises the concept of executing a command on or reading a value from the server over its callback functions. The server is started and stopped by a WinCC OA manager. The WinCC OA client will trigger a command or subscribe to a service provided by the server to the DIM DNS node. The DNS node handles the communication between the server and the client. The command and service functions will trigger their assigned callback functions, defined in the server, where the main functionality is implemented. Commands are used to execute an action; services are used to receive values from the server. From the callback functions, the server submits a task to the asynchronous loop. The loop runs an operation, that writes or reads from the Keithley. The values of the read operation are propagated back to the WinCC OA client. The commands are always submitted on the client side, the services are updated on the server side.

Figure 3.10 visualises the basic structure of the server. At the top of the server class decorators are defined. The decorators are wrappers used around the defined server functions to differentiate between the kinds of functionalities provided. Basic functions without a decorator are mainly handling internal server functionalities. The **Action** functions are functions, that perform a `write()` or `read()` operation on the Keithley. The **Ramping** functions put the server into a **Ramping** state. The **Task** functions are used to submit new tasks to the asynchronous loop.

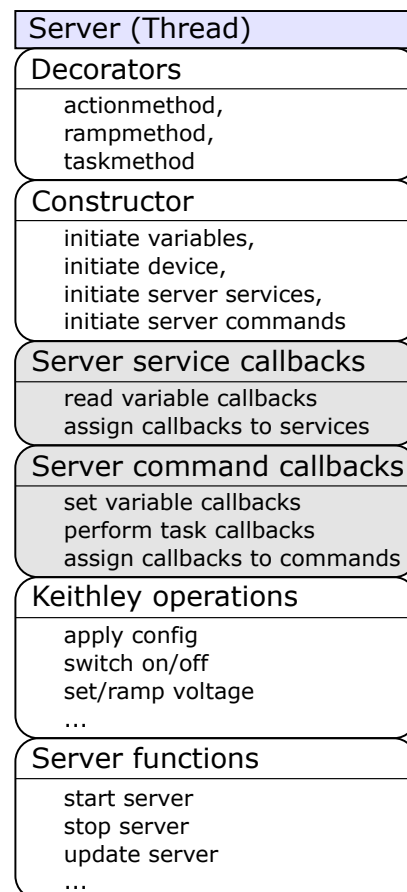


**Figure 3.10:** Server structure.

In the constructor of the class all the relevant variables for the Keithley are defined. This includes the actual voltage and current, the hardware limits that can be set on these values, the voltage source state and many others. The configuration commands are written to the Keithley. All the commands and services of the server are also initialised in the constructor.

In the next section of the code the service callbacks and the command callbacks are defined. The service callbacks are used to read actual values from the Keithley. The command callbacks are used to set values or execute operations on the Keithley. These Keithley operations are mostly implemented as asynchronous functions. They include among others to apply configurations, activate or deactivate the power source, and set or ramp the voltage. Finally, the server control functions are implemented. They include among others launching the main asynchronous loop, as well as starting, stopping, and updating the server.

The server provides logging capabilities, making use of the logging package [67]. Some Keithley specific configurations like the GPIB address are read in via a configuration file using the configparser [68] and argparse [69] package.

#### 3.3.4 User interface

A HV control panel is provided as the user interface. The complete panel can be seen in appendix B.2. The `fwDim` [70] library is used to include DIM functionalities into WinCC OA. The features that have been implemented include performing actions on the Keithleys like starting and stopping the voltage source or ramping the voltage, monitoring of the voltage and the current of the Keithleys, setting of the hardware and software limits, and regular automatic logging of the data. The limits are used for the alarm handling. The alarms are triggered when the monitored values exceed the limits.

Multiple panels are provided: a main panel showing all the relevant information and providing the necessary buttons during normal operation, and additional child panels that can be opened over their respective buttons. At the top of the main panel is a header bar. Besides the title of the panel, a `STOP PROJECT` button is provided that will shut down the complete project and all its managers. This means that it will not just close the panel window but also shut down the DIM servers; the voltage will be ramped down to zero and the voltage sources of the Keithleys are deactivated. To the left of the button the path is displayed, where the data is saved. A `REFRESH ALL` button is given at the top left, which is used to reapply all the settings of the panel.

On the right side of the main panel the actual current and voltage values of all three Keithleys are displayed. The visibility of the curves can be turned on and off to the operators liking. The `fwTrending` component of the JCOP framework is used to display the data and thus comes with all its functionalities. They include among others: scaling of the axis, jumping to a fixed time, and exporting of the trend data. The export functionality has been modified, such that in addition to the default exports of the data in the time range visible in the plot, the desired start and end time of the export can be set.

Below the displayed current and voltage values is a button bar, where the additional child panels can be opened: the `Log viewer`, the `DIM viewer` the `Alert screen` and the `Expert settings`. The `Log viewer` shows the log files for all the WinCC OA managers and processes. The log files of the self-written DIM servers are also included.

The `DIM viewer` is a tool provided by DIM. It shows the servers and clients set up on the DIM DNS node and can be used for debugging. It can also make calls to the server commands and services. The `Alert screen` uses the default alert screen from the `fwAlert` component of the JCOP framework. It can be used to monitor and acknowledge the alarms. The `Expert settings` are used to define settings for the Keithley operations that should not be changed by the standard operator, but only by experts familiar with the functionalities. These settings can only be changed when the voltage sources for all the Keithleys are off to prevent errors when reconfiguring the Keithleys. The reference panel for the expert settings of one of the Keithleys is displayed in figure 3.11.

On the left side of the main panel are the reference panels for the three Keithleys. They all provide the same functionalities. One of the reference panels is shown in figure 3.12. The reference panels are named after the part of the Timepix4 telescope for which the Keithley is providing the voltage: the main telescope, the DUT and a third Keithley, which use is not yet determined.

**Figure 3.11:** Example of expert settings panel for a Keithley.

At the top of the Keithley reference panel are the buttons for the actions that can be performed on the Keithley. The **SWITCH OFF** and **SWITCH ON** buttons are used to turn the voltage source of the Keithley on or off. The **SWITCH OFF** button will ramp down the voltage to zero before completely turning off the voltage source. It uses the same ramping method as the **RAMP VOLTAGE** button. The button is only enabled when the voltage source state is **on**. After successful completion of the action, the voltage source state is set to **off**. The **SWITCH ON** button will set the voltage to a defined **start voltage**, whose value is set in the **Expert settings**. The button is only enabled when the voltage source state is **off**. After successful completion of the action the voltage source state is set to **on**.

The **Apply** button next to the **Target voltage** and **Bias** field will apply a target voltage to the Keithley. The absolute value from the **Target voltage** field is used. The polarity of the voltage is determined over the **Bias** field and can either be set to **positive** or to **negative**. It is changed via the **Expert settings**.

The **RAMP VOLTAGE** button will then ramp the voltage to the applied target voltage. The voltage is ramped up or down to the desired voltage in steps of **step size** and intervals of **step time**. These can be set in the **Expert settings** individually for ramping the voltage up and down. The direction for the ramping is determined on the absolute value of the voltage. While ramping the voltage a **ramping flag** is set. The ramping of the voltage can only be done when the voltage source is **on**. The **STOP RAMPING** button is used to stop the ramping by sending a **cancel** request to the server.

Except for the **Apply** and **STOP RAMPING** all the buttons perform write operations on the Keithley. When clicked an **action flag** is set. To further prevent conflicting user input only one action can be performed at a time. When the status of the Keithley is invalid, meaning no connection can be established, all the buttons except for the **STOP RAMPING** button are disabled.

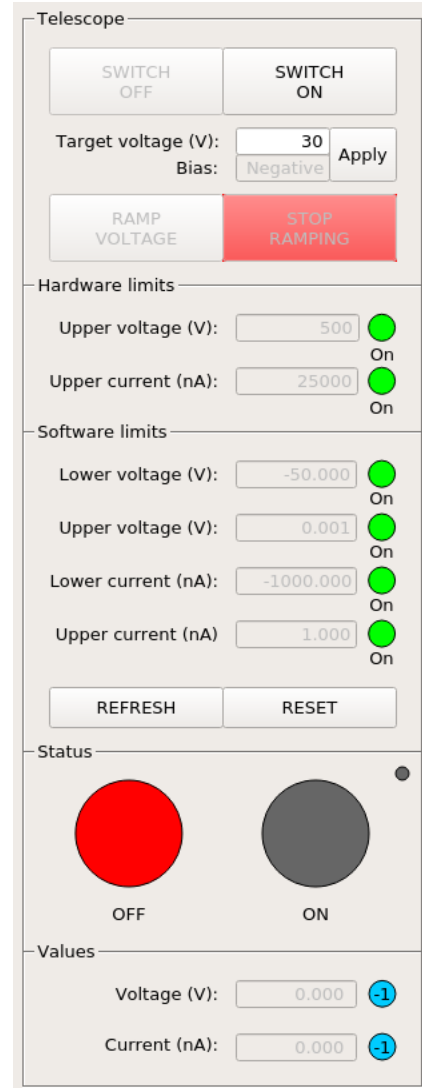


Figure 3.12: Reference panel of the telescope Keithley.

Below the buttons the hardware and software limits are displayed, which can only be changed in the **Expert settings**. The hardware limits are directly applied to the Keithley. They limit the voltage and current output the Keithley will provide. They are set on the absolute values of the voltage and the current. The software limits are set on the current and voltage values that are monitored in WinCC OA. Here not only the upper limit but also the lower limit is displayed. This allows for asymmetric limits on the maximum positive and negative allowed voltage and current. These limits are used for the alarms: when an alarm is triggered any ongoing action, like ramping of the voltage, is cancelled.

Next to each limit a coloured circle (LED) displays if the limit is enabled, by being red (off) or green (on). Below the LED the state is also displayed by a text label, in order to accommodate for colour blindness. The hardware limits are always on and cannot be disabled. The limits can be enabled and disabled over the tick boxes in the **Expert settings**.

Below the limits are a **REFRESH** and a **RESET** button. The **REFRESH** button has the same functionality as the **REFRESH ALL** button in the header bar, except it only applies the settings of the corresponding reference panel. The **RESET** button will reinitialize the Keithley. This means the voltage of the Keithley is ramped to zero, the voltage source is turned off and the settings are reapplied. The **REFRESH** button is always enabled, even if the status of the Keithley is invalid.

Further, the status of the Keithley is displayed. Three coloured circles serve as status LEDs. The left and right big LEDs display whether the Keithleys voltage source is on (green) or off (red). Here two separate LEDs with additional text label are used instead of a single LED as done for the alarms to make it more intuitive for the operator. The small LED in the top right corner blinks yellow whenever a writing action is performed on the Keithley. When the Keithley status is invalid all three LEDs will display cyan.

In the last part of the Keithley reference panel the actual voltage and current values of the Keithley are displayed. The voltage value is updated every time a new voltage target is set or when the Keithley is initialised, refreshed, or resetted. The current value is updated around every second, dependent on the update interval of the server.

To display the status of the values a LED is implemented next to each of them, displaying one of four states. The states are **invalid** (cyan), **normal** (green), **warning** (yellow) and **alarm** (red). The **invalid** state means that the voltage source is off or there was an error receiving the values. The **normal** state means the values could be read without problems and they are not near the alarm limits. The **alarm** and **warning** states are based on the software limits, as described in section 3.2.3.

For colour blind operators the status is additionally displayed as a number, which is negative one for the **invalid** state, zero for the **normal** state, one for the **warning** state and two for the **alarm** state.

### 3.4 Temperature and Humidity control

The TH control of the slow control system is used to monitor the temperature and humidity at different positions of the Timepix4 telescope. The implemented functionalities of the TH project include the monitoring, alarm handling, and data logging of the sensor values. In this section the used hardware, the necessary drivers and software, and the UI of the TH project are described.

#### 3.4.1 Hardware

In total 15 temperature and three humidity sensors are considered in the TH control project. The first eight temperature sensors are meant to monitor the temperature of the eight telescope planes. Further four temperature slots are provided to monitor the temperature of the DUT and its Peltier element. The last three temperature sensors are placed inside the enclosed boxes of the two telescope arms and the DUT, each near a humidity sensor, so that they can be used for the estimation of the dew point in each box.

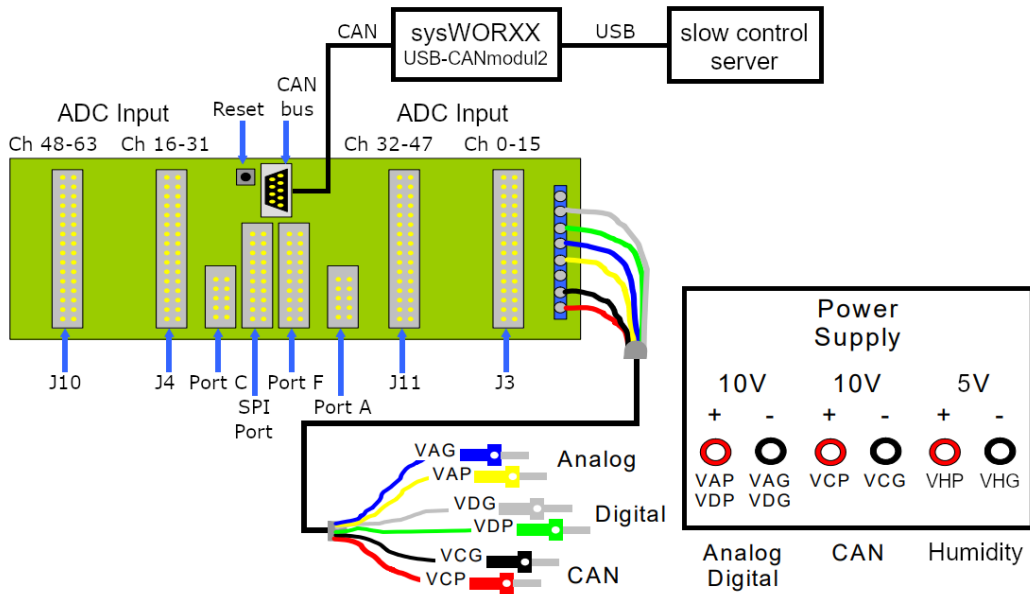


**Figure 3.13:** Schematic overview of the ELMB and its power connection. The board is connected to the slow control machine over the CAN bus. The sensors are connected to the ADC Input channels. The other ports are not used. Modified from reference [71].

The main hardware component, where all the temperature and humidity sensors are connected to, is an Embedded Local Monitor Board (ELMB) [72, 71, 73]. The used version is the ELMB128. The board was originally designed by the ATLAS experiment for control tasks with high channel density in radiation environments. A schematic overview of the ELMB setup is shown in figure 3.13. The ELMB has four Analogue Digital Converter (ADC) input connectors (J3, J4, J10 and J11) with 16 ADC channels each, making a total of 64 input channels. The temperature and humidity sensors are connected to these ADC channels. The ADC signal can be modified by adapters, that are plugged into the back of the board. The board additionally comes with various digital ports called Port A (J5), Port C (J9), and Port F (J7), and a Serial Port Interface (SPI) port (J8). Located next to the CAN bus connector is a button to reset the ELMB.

The ELMB is connected to the slow control server over a sysWORXX interface. The USB-CANmodul2 is used [74]. The ELMB is powered with a voltage of two times 10 V by an external voltage source. The external source is also used to power the humidity sensors, with the 5 V bias. The reference voltage for the temperature sensors of 2.5 V is provided by the ADC channels of the ELMB.

To monitor the temperature four-wire Pt100 sensors [75] are used. They are used together with the 4WPT100 signal adapter. The four-wire connection eliminates the dependency on the wire resistance. As one ADC channel uses two connector pins, each temperature sensor occupies two ADC channels. The circuit diagram for a temperature sensor is shown in figure 3.14 (a). The circuit diagram for the 4WPT100 adapter is shown in figure 3.14 (b). The resistance values for RC and RS are  $R_{RC} = 3.9\text{ k}\Omega$  and  $R_{RS} = 100\ \Omega$ , respectively.

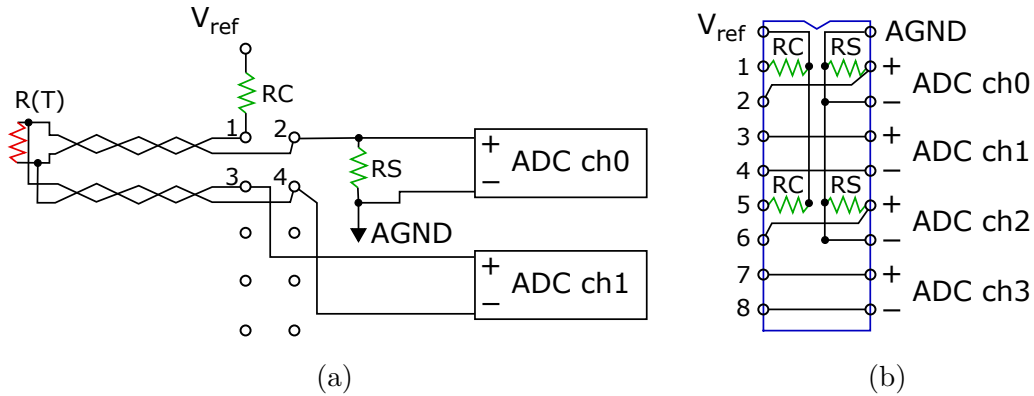


**Figure 3.14:** The circuit diagram for a four-wire temperature sensor (a) and a 4WPT100 adapter (b). Recreated from reference [71].

The ADC channels read voltage values. The temperature value is calculated from a quadratic dependency of the sensor resistance  $R(T)$  from the temperature  $T$  [71]:

$$R(T) = R_0 (1 + aT + bT^2), \quad (3.1)$$

where  $R_0 = 100\Omega$  is the value of the Pt100 resistor at  $0^\circ\text{C}$ . The parameters  $a = 3.9083 \times 10^{-3} \text{ }^\circ\text{C}^{-1}$  and  $b = -5.775 \times 10^{-7} \text{ }^\circ\text{C}^{-2}$  depend on the type of sensor and are provided by the manufacturer. The equation can be solved to give the value of the temperature  $T$ :

$$T = \frac{-a + \sqrt{a^2 - 4b(1 - \frac{R(T)}{R_0})}}{2b}. \quad (3.2)$$

The value of  $R(T)$  can be determined from the ADC voltage values as:

$$R(T) = R_{\text{RS}} \frac{V_{\text{ch1}}}{V_{\text{ch0}}}, \quad (3.3)$$

where  $V_{\text{ch1,2}}$  are the voltage values of the ADC channels ch0 and ch1.

To monitor the humidity HIH-4000 [76, 77] sensors are used. They use a two-wire connection, thus each humidity sensor is connected to one ADC channel of the ELMB. On the back of the ELMB a 4116-R1-102 resistor network [78] with  $1\text{ k}\Omega$  resistors is used as the signal adapter. Its circuit diagram is shown in figure 3.15. The relative humidity is calculated over the voltage value of the ADC channel. From the manufacturer of the HIH-4000 sensors the formula to determine the relative humidity %RH at  $25^\circ\text{C}$  is provided as:

$$\%RH = \frac{V_{\text{ch0}} - V_0}{m}, \quad (3.4)$$

assuming a supply voltage for the humidity sensor of  $V_{\text{supply}} = 5\text{ V}$ . The voltage  $V_{\text{ch0}}$  is the ADC channel voltage. The constants for the zero offset  $V_0 = 0.826\text{ V}$  and the slope  $m = 31.483\text{ mV}/\%RH$  are also provided by the manufacturer.

The constants vary slightly between the sensors, so each HIH-4000 sensor can be ordered with its own calibration to increase the accuracy. The sensor printouts were not yet provided at the time of this thesis, which is why the standard values are used in the test setup. Despite this, a new HIH-4000 sensor type has been defined using the `fwDevice` and `fwELMB JCOP` components to allow to quickly add new humidity sensors with their individual constants.

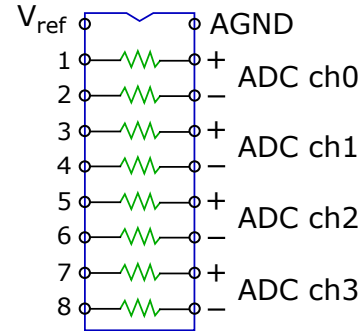


**Figure 3.15:** The circuit diagram for a resistor network adapter. Recreated from reference [71].



The humidity sensors are slightly dependent on the temperature  $T$ . The formula to correct for this effect is given as:

$$\%RH_T = \%RH(1.0546 - 0.00216T). \quad (3.5)$$

In the current version of the TH control the temperature dependency is neglected, because it is expected to only marginally affect the humidity. For the test setup two temperature sensors and one humidity sensor are connected to the ELMB. Images of the setup are shown in figure 3.16.

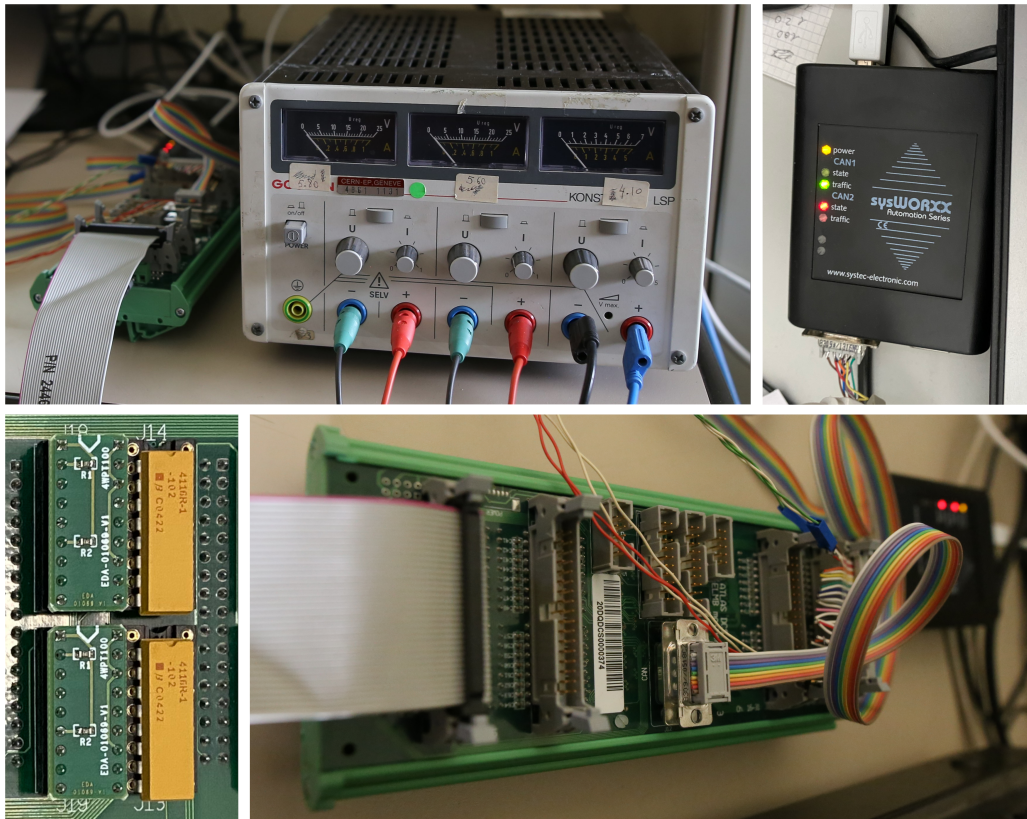


**Figure 3.16:** The top left image shows the voltage source next to the ELMB. The top right image shows the sysWORXX interface. The bottom left image shows two of the 4WPT100 adapters (green) and two of the resistor adapters (yellow). The bottom right image shows the front side of the ELMB.

### 3.4.2 Estimating the dew point

Besides monitoring the temperature and the humidity of the Timepix4 telescope, additionally the dew point is estimated for each of the enclosed boxes of the telescope arms and the DUT. The dew point  $T_{\text{DP}}$  can be approximated as a function of the relative humidity %RH and the temperature  $T$  [79, 80]:

$$T_{\text{DP}} = \frac{c \ln \left( \frac{\%RH}{100} \frac{P_s(T)}{a} \right)}{b - \ln \left( \frac{\%RH}{100} \frac{P_s(T)}{a} \right)}, \quad (3.6)$$

where one of the most used empirical expression for the saturated water vapour pressure  $P_s(T)$  is given as:

$$P_s(T) = a \exp \left( \frac{bT}{c + T} \right). \quad (3.7)$$

Here the constants  $a = 6.1121$  mbar,  $b = 17.502$  and  $c = 240.97^\circ\text{C}$  are optimised for a temperature interval of  $(-20^\circ\text{C}, 50^\circ\text{C})$  [80].

### 3.4.3 Drivers and software

The ELMB uses a Controller Area Network (CAN) bus to communicate with the slow control machine. The drivers needed to communicate with the hardware are visualised in figure 3.17. The CAN bus from the board is connected over the sysWORXX interface. To use CAN with Linux additional SocketCAN drivers [81] are required. The communication with WinCC OA is then established using the OPC UA protocol and a OPC UA CAN server. The OPC UA communication protocol uses the principles described in section 3.2.5. For the OPC UA protocol the DP elements are created in WinCC OA and then mirrored to the OPC UA CAN server by creating a server configuration file with the help of the fwELMB JCOP component [73]. The OPC UA CAN server is started and closed by a WinCC OA manager.

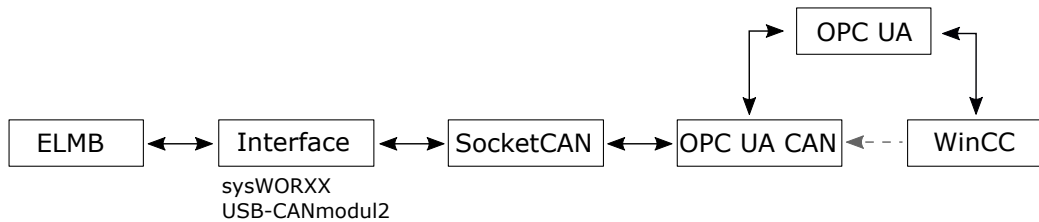


**Figure 3.17:** Visualisation of the drivers used to communicate between WinCC OA and the ELMB.

### 3.4.4 User interface

A TH control panel is provided as the user interface. The complete panel can be seen in appendix B.3. The features that have been implemented include detailed monitoring of all the temperature and humidity sensor values, setting of software limits over a specified `Sensor expert` panel, calculation of the dew points and regular automatic logging of the data. The limits are used for the alarm handling. Multiple panels are provided: a main panel showing all the relevant information and providing the necessary buttons during normal operation, and additional child panels that can be opened over their respective buttons.

At the top of the main panel is the header bar. For consistency reasons it is structured like the header bar of the HV control panel (refer to section 3.3.4), including the title of the panel, a `STOP PROJECT` button and the path to the automatically exported data. Instead of the `REFRESH ALL` button that was specific to the HV control, here the dew points of the three enclosed boxes of the two telescope arms and the DUT are displayed.

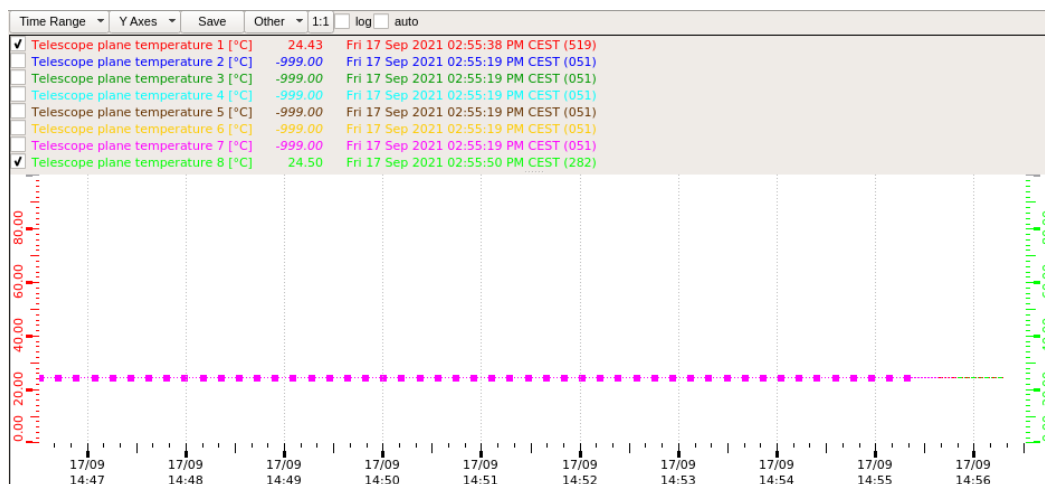


**Figure 3.18:** One of the trends displaying the temperature values of the telescope planes. Only the two sensors that have been connected in the test setup are set to be visible.

The TH control panel is used to monitor the sensor data. Therefore, three large trend widgets are used to display the data, of which one is exemplary shown in figure 3.18. In the top left the humidity and the temperature of the three boxes are displayed. These are also the values that are used to calculate the dew points. In the top right the temperature values of up to eight telescope planes are shown. In the lower right the temperature values of the up to four temperature sensors

considered for the DUT are depicted. To display the values, the same modified JCOP framework component is used, as for the HV control panel. In the lower left corner of the main panel all the sensor values are additionally displayed in a table, as shown in figure 3.19.

Status	Channel Name	Comment	Value	Time Stamp	Unit
Connected	PT_4W_00_01	Telescope plane temperature 1	24.43	2021.09.17 14:55:38.519	°C
Not connected	PT_4W_02_03	Telescope plane temperature 2	-999.00	2021.09.17 14:52:28.063	°C
Not connected	PT_4W_04_05	Telescope plane temperature 3	-999.00	2021.09.17 14:52:36.979	°C
Not connected	PT_4W_06_07	Telescope plane temperature 4	-999.00	2021.09.17 14:52:44.475	°C
Not connected	PT_4W_08_09	Telescope plane temperature 5	-999.00	2021.09.17 14:52:53.369	°C
Not connected	PT_4W_10_11	Telescope plane temperature 6	-999.00	2021.09.17 14:53:00.745	°C
Not connected	PT_4W_12_13	Telescope plane temperature 7	-999.00	2021.09.17 14:53:09.315	°C
Connected	PT_4W_14_15	Telescope plane temperature 8	24.50	2021.09.17 14:55:50.282	°C
Not connected	PT_4W_16_17	DUT temperature 1	-999.00	2021.09.17 14:53:26.072	°C
Not connected	PT_4W_18_19	DUT temperature 2	-999.00	2021.09.17 14:53:33.978	°C
Not connected	PT_4W_20_21	DUT temperature 3	-999.00	2021.09.17 14:53:42.304	°C
Not connected	PT_4W_22_23	DUT temperature 4	-999.00	2021.09.17 14:53:50.286	°C
Not connected	PT_4W_32_33	Box temperature 1	-999.00	2021.09.17 14:54:00.695	°C
Not connected	PT_4W_34_35	Box temperature 2	-999.00	2021.09.17 14:54:13.994	°C
Not connected	PT_4W_36_37	Box temperature 3	-999.00	2021.09.17 14:54:22.484	°C
Connected	RH_4000_48	Box humidity 1	40.04	2021.09.17 14:55:59.796	%
Not connected	RH_4000_49	Box humidity 2	-999.00	2021.09.17 14:54:39.367	%
Not connected	RH_4000_50	Box humidity 3	-999.00	2021.09.17 14:54:47.847	%

**Figure 3.19:** The panel component that shows the state and readings of the ELMB. At the bottom are the buttons to access the child panels.

The alarm status of the values is shown by the colour of the background of the values. **Grey** means that the values are invalid, **green** that they are in the normal range, **yellow** that a warning has been triggered for this value, and **red** that an alarm has been raised. When a sensor value is outside a defined range the value is set to  $-999$  and marked as *invalid*. The range for the temperature sensors is set to  $(-100^{\circ}\text{C}, 1000^{\circ}\text{C})$  and for the humidity sensors to  $(0\%, 100\%)$ .

The values in the table are displayed together with the name of the channel, a description, and a time stamp. The **Channel name** column gives information about the sensor type and the ELMB channels the sensor is connected to. The **Comment** column is used to describe where the sensor is located in the telescope. The **Time stamp** column gives the time when the value was last updated. This can be helpful in case of a malfunctioning sensor. Additionally, the unit and the status of the individual channels are displayed. The status is set manually in the **Sensor expert** panel. It is used to display which of the sensors are physically connected to the ELMB.

The ELMB sends its ADC values even if no sensor is connected. This results in nonsensical negative or **nan** values. The connected status of a channel is shown by a coloured LED and a text field. The possible values are **connected** (green) and **not connected** (red). When setting a channel to **not connected** the value for the channel is explicitly set to invalid.

Below the table a button bar is implemented, where the child panels can be accessed. It holds a status LED and text field for the ELMB, like the connected states of the individual channels. The most common states are **DISCONNECTED** (cyan), **OPERATIONAL** (green) or **STOPPED** (red). Further states are **PREOPERATIONAL** (yellow) and **UNKNOWN** (purple). These are also the states reported in the ELMB expert panel. The child panels are the **Alert screen**, the **Log viewer** and the expert panels. The expert panels are the ELMB expert panel, the OPCUA expert panel and the Sensor expert panel. The **Alert screen** and the **Log viewer** are the same as for the HV control panel, used for viewing the alarms and the logged files.

The ELMB expert panel expands upon the ELMB state. It is adopted from the fwELMB JCOP component and displays some additional error messages. It also provides buttons to change the ELMB state. The OPCUA expert panel is also adopted from the fwELMB JCOP component. It can be used to convert the ELMB channel addresses to the OPC UA format. By default, this is done automatically when the main panel is initialised.

In the **Sensor expert** panel, the limits for the alarms for the individual sensors are set. The connected status is also selected in this panel. The **Sensor expert** panel is displayed in figure 3.20.

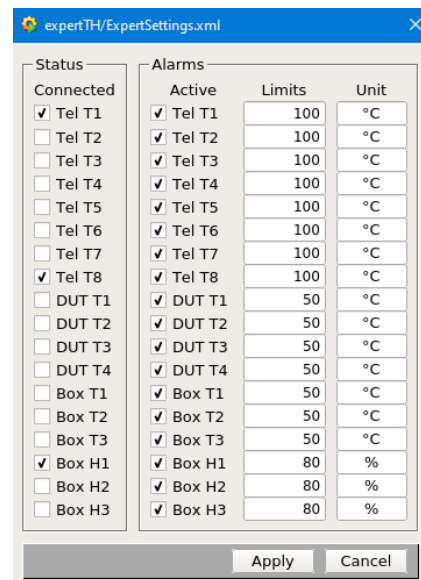


**Figure 3.20:** The panel for the expert settings of the sensors.

### 3.5 Combined projects

Both implemented projects are combined into a main project. The main project has been set up to easily start all the required managers of both projects, as well as open the main operator panels, by a single click of a desktop icon. The managers will take care of starting the servers and the DBs used for logging. The **Log viewer** is also started in the background. This allows for very convenient operation of the HV and the TH project. The other parts of the slow control system, not covered in this thesis, will be added to the main project once finalised.

## 4 Conclusion and Outlook

In the first part of this thesis simulation studies are performed to evaluate the impact of the change in beam conditions between Run II and Run III, as well as the upgraded configurations of the LHCb subdetectors, on the BCM settings. From the simulation, a new set of thresholds is proposed for the BCM dump logic during physics data taking. It has been verified that these thresholds would protect the most delicate parts of the LHCb detector, the VELO sensors and the RF foil, in case of an adverse scenario affecting either of the two beams.

The BCM is the most important system for protecting the detector, by initialising a beam dump when the measured currents exceed the threshold values. In the period leading up to the beam dump an increased exposure in the detector components is expected. The worst case increase in temperature for the RF foil is estimated to be of the order 0.01 K in 40  $\mu$ s.

The proposed thresholds will be used in the first period of data taking next spring. The data taken in this time span will be compared to the simulation and based on the results the thresholds will then be adjusted to the final thresholds used during Run III. Furthermore, the framework developed will be re-employed to study the role of the BCM in the context of machine induced backgrounds, once the simulation input is provided by the LHC experts.

In the second part of the thesis a slow control system for the Timepix4 telescope is developed. Two projects have been implemented, responsible to remotely control the high voltage of the telescope and monitor the temperature and humidity, respectively. The communication has been established with the hardware and user interfaces have been prepared in the form of operator panels, with several control, monitoring, and data logging functionalities implemented. The slow control system will be first tested in the upcoming test beam period in October. The provided feedback will be used to optimise the panels.

## A Additional plots of the simulation

In this appendix additional plots of the simulation are shown that were mentioned during this thesis. This includes plots for the occupancy and the energy deposition for the simulations performed under nominal beam conditions, as well as the plots for the coverage of the detector components for beam 2 for the simulation performed under adverse beam conditions.

### A.1 Occupancy plots

The mean occupancy as a function of the BCM sensor ID is shown in figure A.1 (a) per event and in figure A.1 (b) per  $40\ \mu\text{s}$ , respectively. The sensor ID is 0 to 7 for the BCM-U sensors, and 8 to 15 for the BCM-D sensors. The mean values and their uncertainty in figure A.1 (a) correspond to the mean and the RMS of the distributions (not Gaussian), while the mean values and their uncertainty in figure A.1 (b) correspond to the mean and the standard derivation of the Gaussian function fitted to the distribution.

The occupancy in the VELO sensors averaged over the stations, and the occupancy in the RF foil per  $40\ \mu\text{s}$  are shown in figure A.2 (a) and figure A.2 (b), respectively. The histograms are fitted with a Gaussian function. Since the occupancy in the VELO sensors in figure A.2 (a) is averaged over all stations, it needs to be multiplied by the number of VELO stations  $n_{\text{stations}} = 26$ , to obtain the mean occupation per  $40\ \mu\text{s}$  in all the VELO stations.

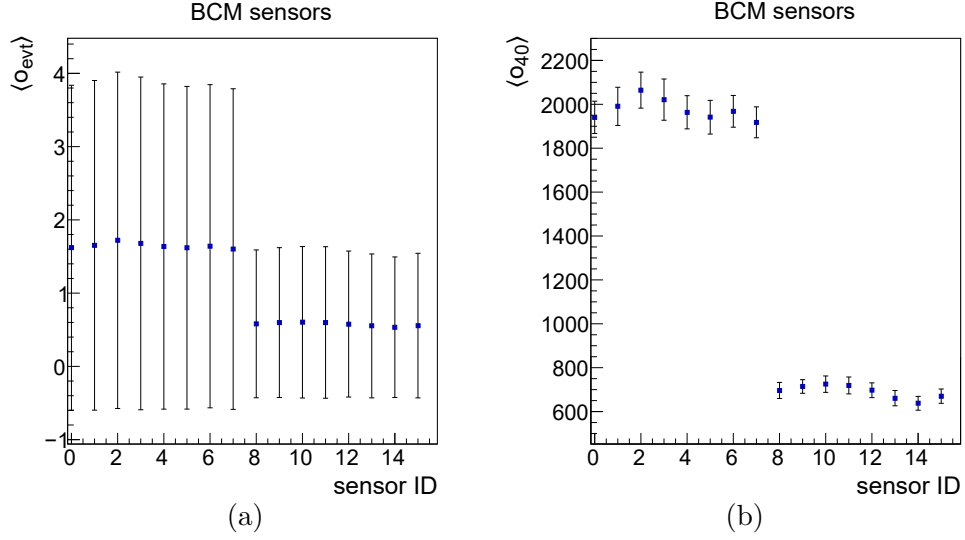


**Figure A.1:** The mean occupancy per event  $\langle o_{\text{evt}} \rangle$  in the BCM sensors (a) and per 40  $\mu\text{s}$   $\langle o_{40} \rangle$  (b) as a function of the sensor ID.

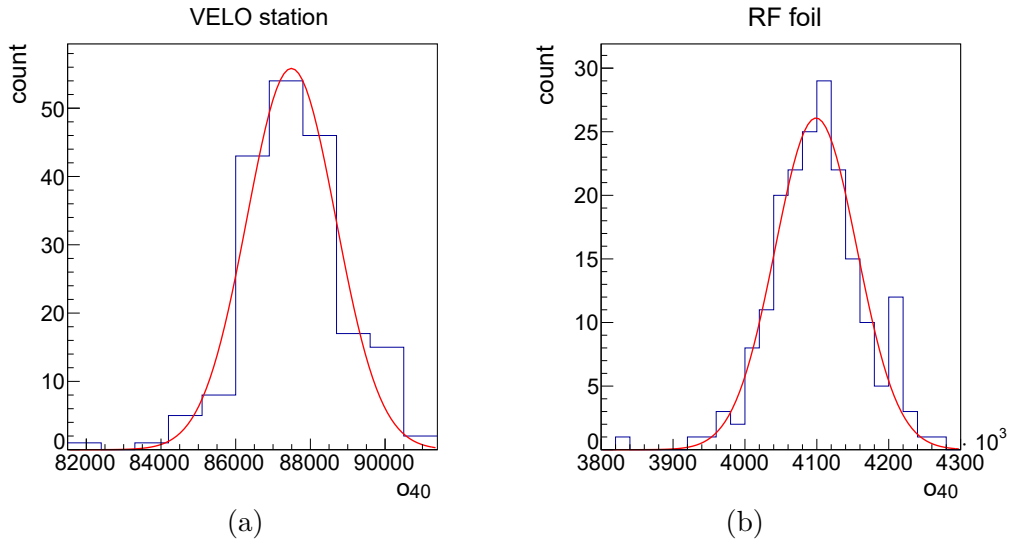


**Figure A.2:** The occupancy per 40  $\mu\text{s}$   $o_{40}$  in the VELO sensors averaged over the stations (a), and in the RF foil (b). The histograms are fitted with a Gaussian function.



## A.2 Energy deposition plots

The energy deposited in the VELO sensors and the RF foil in  $40\ \mu\text{s}$  is shown in figure A.3 (a) and figure A.3 (b), respectively. The mean values of the Gaussian fit are the values of the mean energy deposition  $\langle E_{40} \rangle$ , in the respective detector components. Since the energy deposition in the VELO sensors is averaged over all stations, it needs to be multiplied by the number of VELO stations  $n_{\text{stations}} = 26$ , to obtain the mean energy deposition per  $40\ \mu\text{s}$  in all VELO stations.

The two-dimensional distribution of the mean energy deposition per  $40\ \mu\text{s}$  in the RF foil is shown in the  $x$ - $y$  plane and the  $z$ - $x$  plane in figure A.4 (a) and figure A.4 (b), respectively.

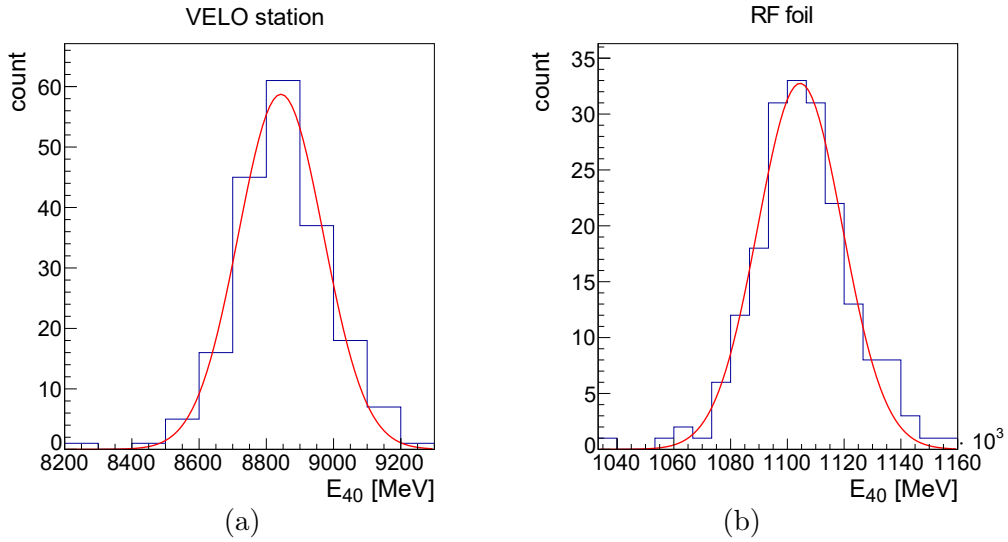


**Figure A.3:** The energy deposition per  $40\ \mu\text{s}$   $E_{40}$  in the VELO sensors (a), and the RF foil (b). The histograms are fitted with a Gaussian function.

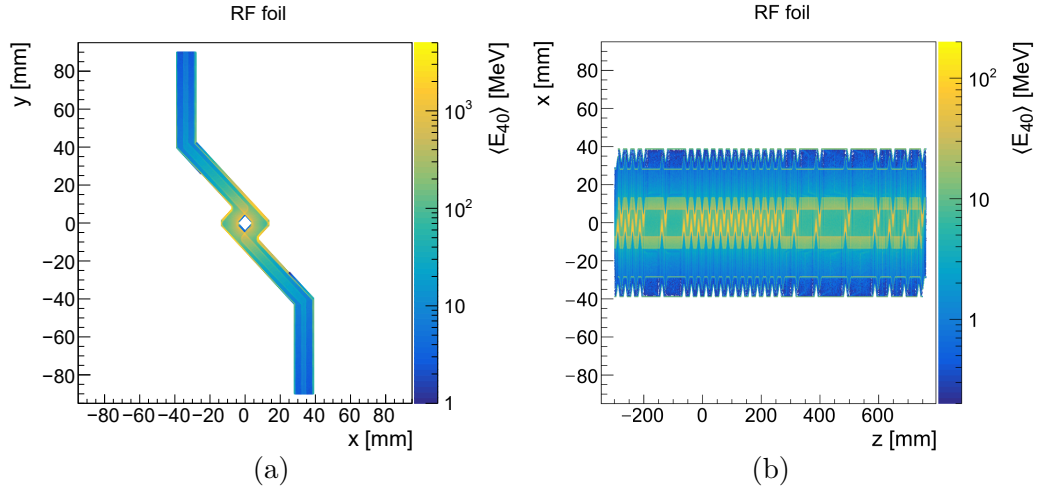


**Figure A.4:** Two-dimensional distribution of the mean energy deposition per  $40 \mu\text{s}$   $\langle E_{40} \rangle$  in the RF foil in the  $x$ - $y$  plane (a) and the  $z$ - $x$  plane (b).

### A.3 Coverage of the detectors for beam 2

For the beam 2 simulation of adverse beam conditions, the BCM-U station is of relevance. The coverage of the BCM-U station, the VELO sensors and the RF foil is shown in figure A.5 (a), figure A.5 (b), and figure A.5 (c), respectively. The coloured lines indicate the border of the coverage of the respective detector components. In figure A.5 (d) the coverage is compared. Here the statistic uncertainty on the border of the coverage, due to the limited size of the data sample, has not been evaluated, however it can be assumed to be analogous to the beam 1 simulations.

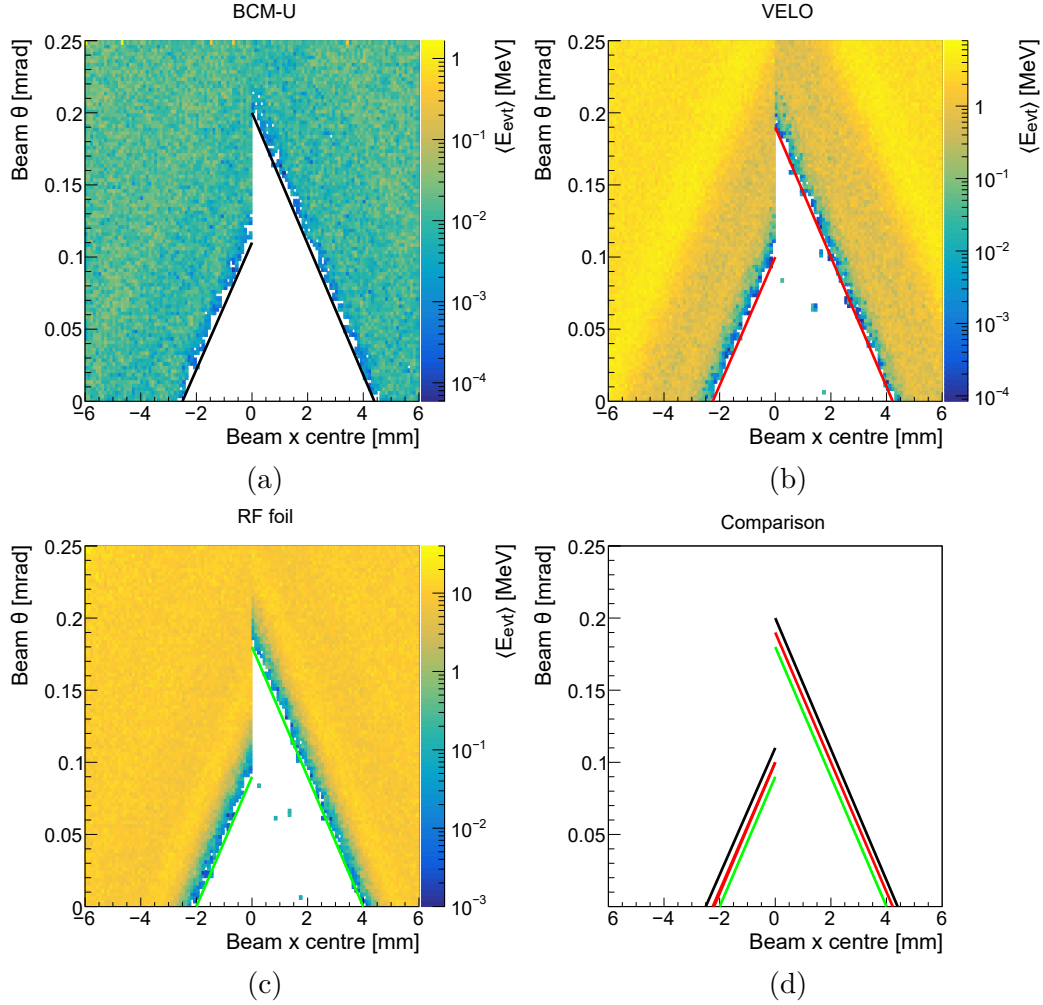
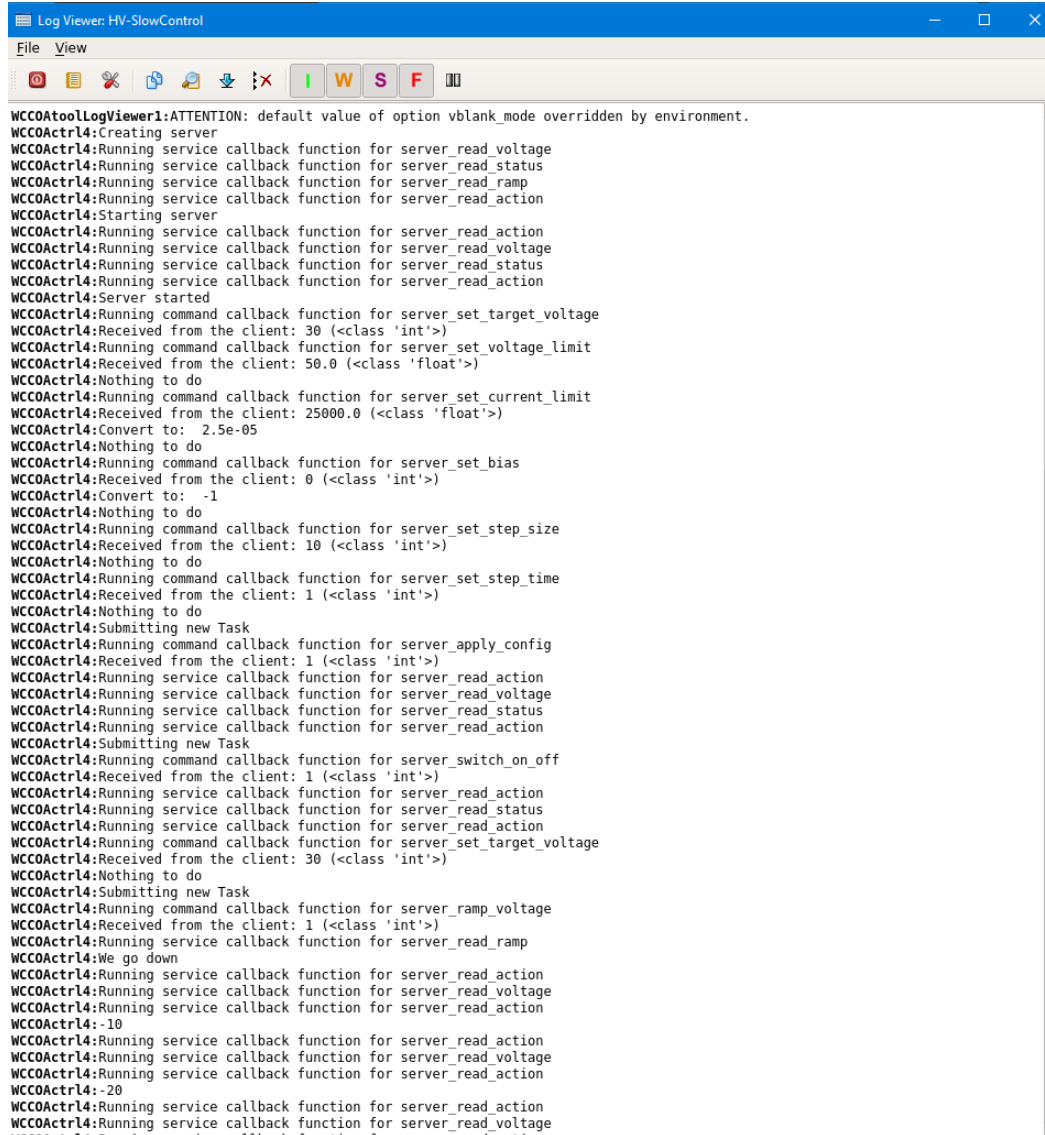


**Figure A.5:** The coverage for beam 2 of the BCM-U station (a), the VELO sensors (b), and the RF foil (c). On the  $z$  axis is the mean energy deposited per event  $\langle E_{\text{evt}} \rangle$ . The coloured lines indicate the border of the coverage of the respective detector components. In figure (d) the border of the coverage of the three detector components is compared. A statistical uncertainty must be assumed on the border of the coverage, due to the limited size of the data sample.





```
Log Viewer: HV-SlowControl
File View
WCCOActrl4:ATTENTION: default value of option vblank_mode overridden by environment.
WCCOActrl4:Creating server
WCCOActrl4:Running service callback function for server_read_voltage
WCCOActrl4:Running service callback function for server_read_status
WCCOActrl4:Running service callback function for server_read_ramp
WCCOActrl4:Running service callback function for server_read_action
WCCOActrl4:Starting server
WCCOActrl4:Running service callback function for server_read_action
WCCOActrl4:Running service callback function for server_read_voltage
WCCOActrl4:Running service callback function for server_read_status
WCCOActrl4:Running service callback function for server_read_action
WCCOActrl4:Server started
WCCOActrl4:Running command callback function for server_set_target_voltage
WCCOActrl4:Received from the client: 30 (<class 'int'>)
WCCOActrl4:Running command callback function for server_set_voltage_limit
WCCOActrl4:Received from the client: 50.0 (<class 'float'>)
WCCOActrl4:Nothing to do
WCCOActrl4:Running command callback function for server_set_current_limit
WCCOActrl4:Received from the client: 25000.0 (<class 'float'>)
WCCOActrl4:Convert to: 2.5e-05
WCCOActrl4:Nothing to do
WCCOActrl4:Running command callback function for server_set_bias
WCCOActrl4:Received from the client: 0 (<class 'int'>)
WCCOActrl4:Convert to: -1
WCCOActrl4:Nothing to do
WCCOActrl4:Running command callback function for server_set_step_size
WCCOActrl4:Received from the client: 10 (<class 'int'>)
WCCOActrl4:Nothing to do
WCCOActrl4:Running command callback function for server_set_step_time
WCCOActrl4:Received from the client: 1 (<class 'int'>)
WCCOActrl4:Nothing to do
WCCOActrl4:Submitting new Task
WCCOActrl4:Running command callback function for server_apply_config
WCCOActrl4:Received from the client: 1 (<class 'int'>)
WCCOActrl4:Running service callback function for server_read_action
WCCOActrl4:Running service callback function for server_read_voltage
WCCOActrl4:Running service callback function for server_read_status
WCCOActrl4:Running service callback function for server_read_action
WCCOActrl4:Submitting new Task
WCCOActrl4:Running command callback function for server_switch_on_off
WCCOActrl4:Received from the client: 1 (<class 'int'>)
WCCOActrl4:Running service callback function for server_read_action
WCCOActrl4:Running service callback function for server_read_status
WCCOActrl4:Running service callback function for server_read_action
WCCOActrl4:Running command callback function for server_set_target_voltage
WCCOActrl4:Received from the client: 30 (<class 'int'>)
WCCOActrl4:Nothing to do
WCCOActrl4:Submitting new Task
WCCOActrl4:Running command callback function for server_ramp_voltage
WCCOActrl4:Received from the client: 1 (<class 'int'>)
WCCOActrl4:Running service callback function for server_read_ramp
WCCOActrl4:We go down
WCCOActrl4:Running service callback function for server_read_action
WCCOActrl4:Running service callback function for server_read_voltage
WCCOActrl4:Running service callback function for server_read_action
WCCOActrl4:-10
WCCOActrl4:Running service callback function for server_read_action
WCCOActrl4:Running service callback function for server_read_voltage
WCCOActrl4:Running service callback function for server_read_action
WCCOActrl4:-20
WCCOActrl4:Running service callback function for server_read_action
WCCOActrl4:Running service callback function for server_read_voltage
```

Figure B.2: The log viewer panel.

## B.2 High Voltage panels

The expert settings panel of the HV project is shown in figure B.3, the DIM viewer in figure B.4. The left and right side of the main operator panel of the HV project are shown in figure B.5 and figure B.6, respectively.

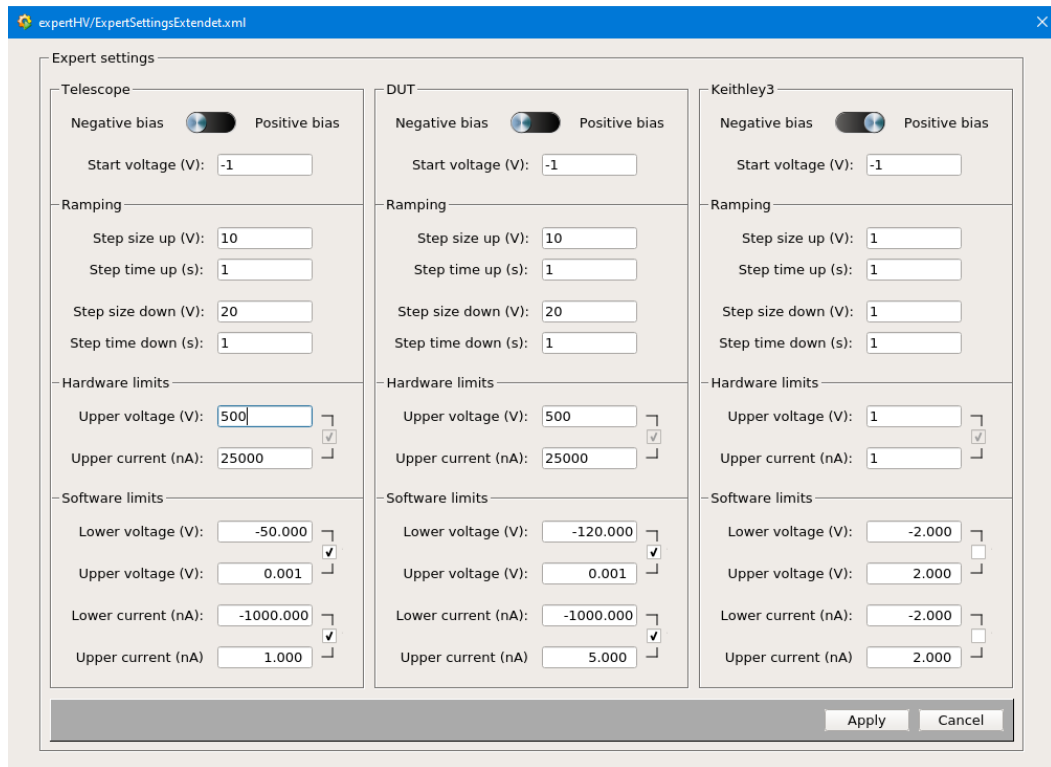


Figure B.3: The expert settings panel of the HV project.

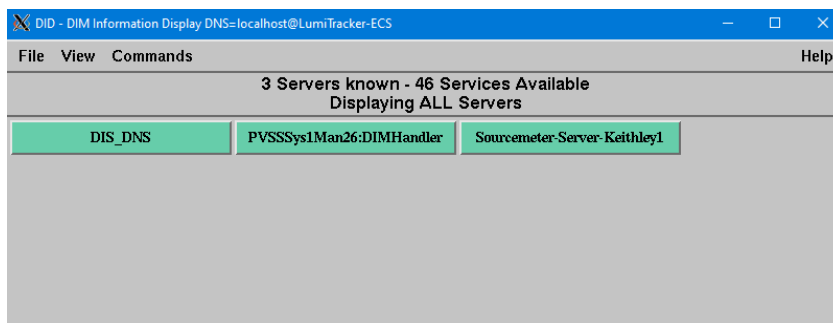


Figure B.4: The DIM viewer of the HV project.

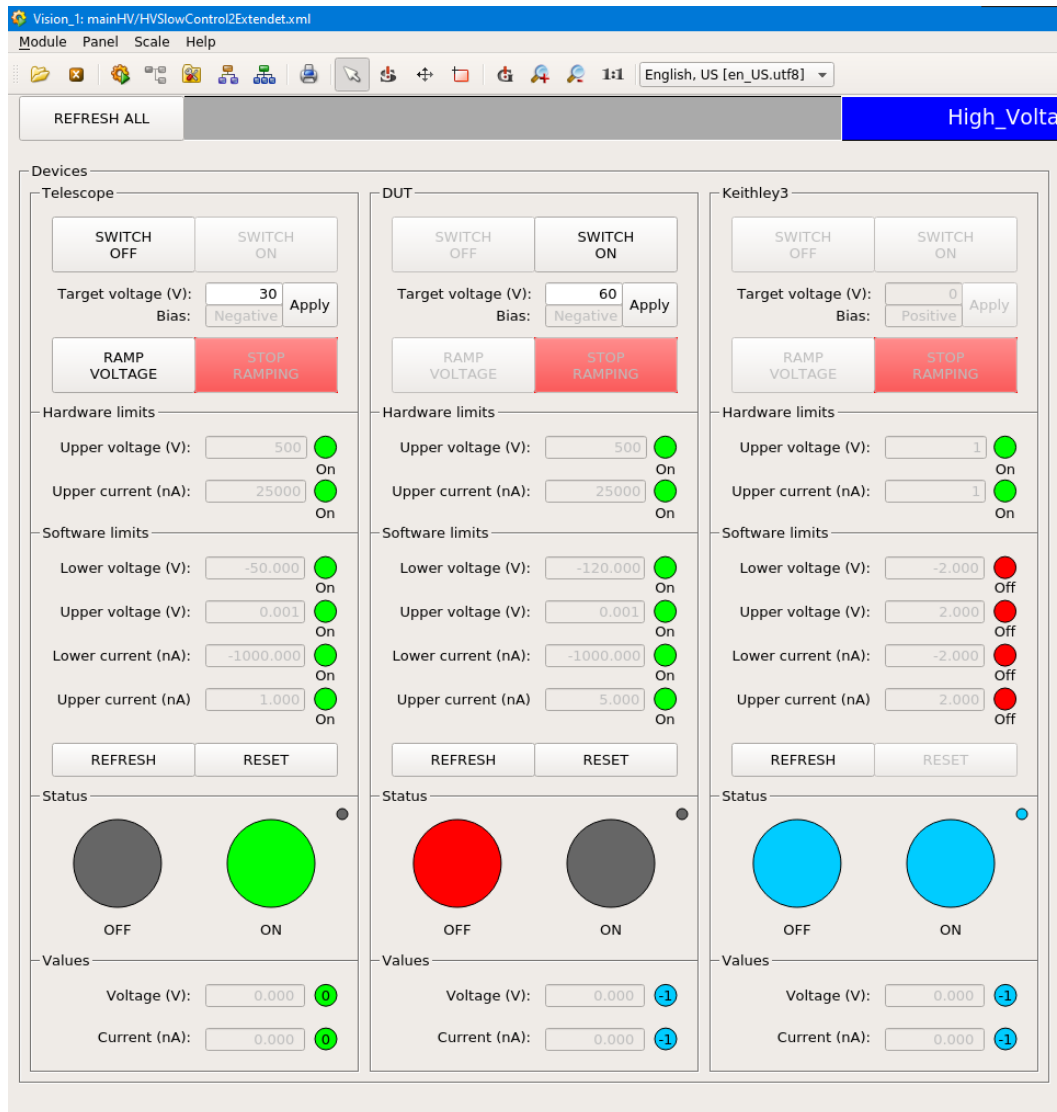


Figure B.5: The left side of the HV main operator panel.

B Slow control operator panels

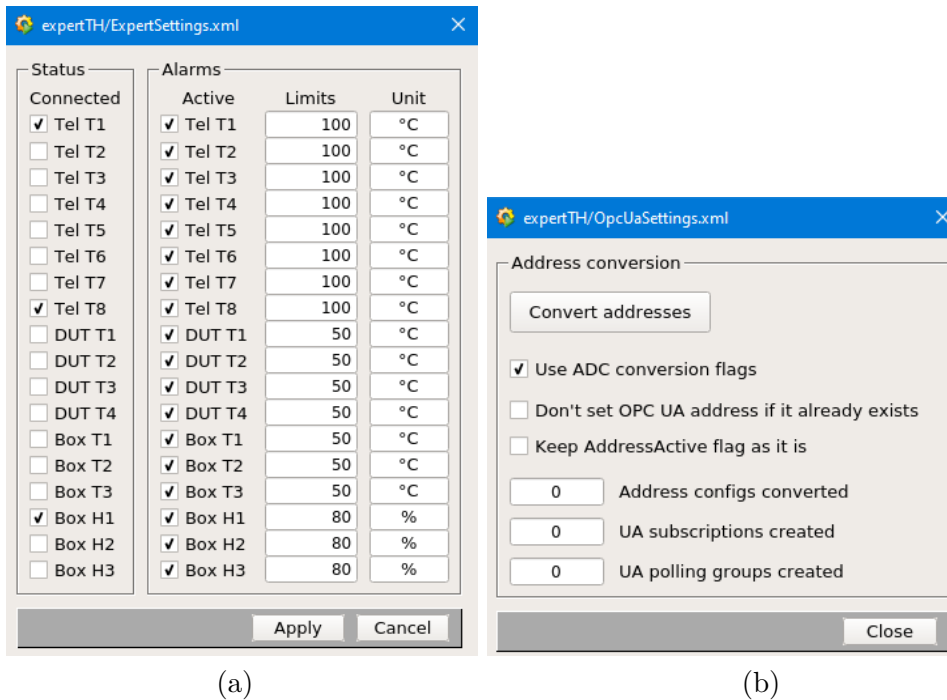


Figure B.6: The right side of the HV main operator panel.



### B.3 Temperature and Humidity panels

The sensor expert settings panel and the OPC UA expert panel are shown in figure B.7. The ELMB expert settings panel is shown in figure B.8. The left and right side of the main operator panel of the TH project are shown in figure B.9 and figure B.10, respectively.



**Figure B.7:** The sensor expert panel (a), and the OPC UA expert panel (b) of the TH project.

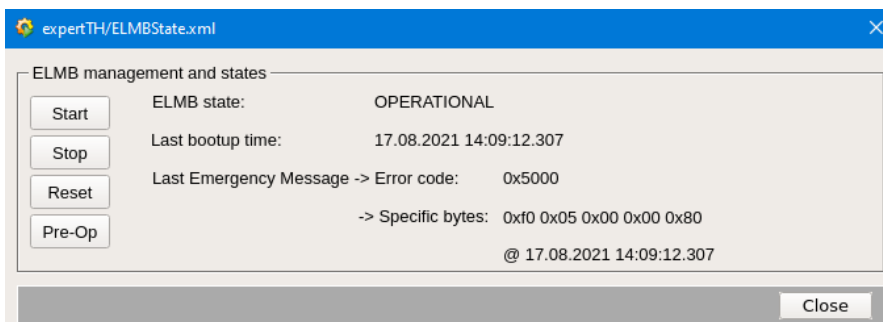


**Figure B.8:** The ELMB expert panel of the TH project.

## B Slow control operator panels

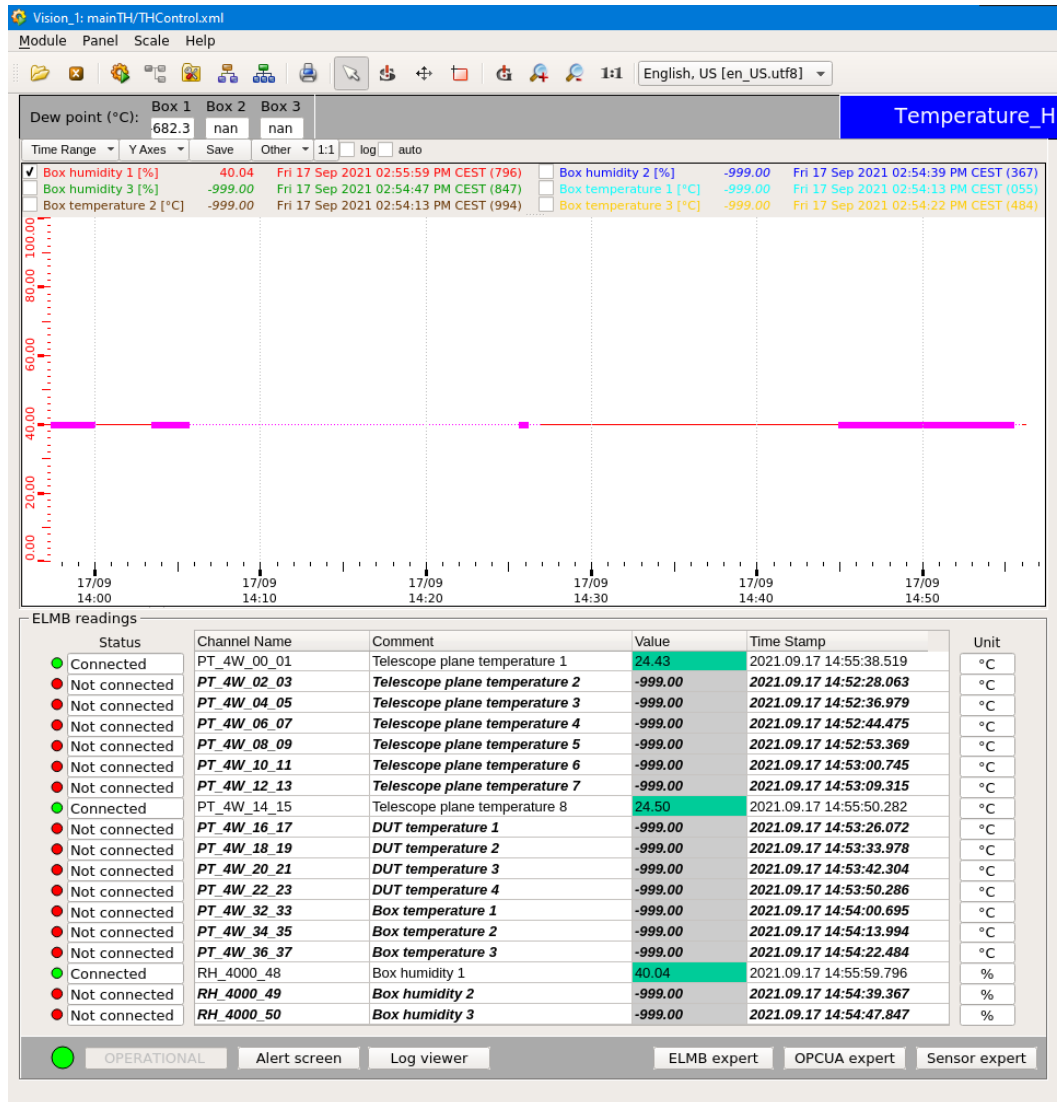


Figure B.9: The left side of the main TH operator panel.

### B.3 Temperature and Humidity panels



Figure B.10: The right side of the main TH operator panel.

## Bibliography

- [1] Helmut Hilscher. *Elementare Teilchenphysik*. Facetten. Vieweg+Teubner Verlag, 2013. ISBN: 9783322850034.
- [2] Alexander Knochel. ‘Offene Fragen’. In: *Neustart des LHC: neue Physik. essentials* (2016). Springer Spektrum, Wiesbaden.
- [3] Oliver Sim Brüning et al. *LHC Design Report*. CERN Yellow Reports: Monographs. Geneva: CERN, 2004. DOI: 10.5170/CERN-2004-003-V-1. URL: <https://cds.cern.ch/record/782076>.
- [4] A. Augusto Alves Jr. et al. ‘The LHCb Detector at the LHC’. In: *JINST* 3 (2008), S08005. DOI: 10.1088/1748-0221/3/08/S08005.
- [5] G. Aad et al. ‘The ATLAS Experiment at the CERN Large Hadron Collider’. In: *JINST* 3 (2008), S08003. DOI: 10.1088/1748-0221/3/08/S08003.
- [6] S. Chatrchyan et al. ‘The CMS Experiment at the CERN LHC’. In: *JINST* 3 (2008), S08004. DOI: 10.1088/1748-0221/3/08/S08004.
- [7] K. Aamodt et al. ‘The ALICE experiment at the CERN LHC’. In: *JINST* 3 (2008), S08002. DOI: 10.1088/1748-0221/3/08/S08002.
- [8] G. Aad et al. ‘Observation of a new particle in the search for the Standard Model Higgs boson with the ATLAS detector at the LHC’. In: *Physics Letters B* 716.1 (Sept. 2012), pp. 1–29. ISSN: 0370-2693. DOI: 10.1016/j.physletb.2012.08.020. URL: <http://dx.doi.org/10.1016/j.physletb.2012.08.020>.
- [9] S. Chatrchyan et al. ‘Observation of a new boson at a mass of 125 GeV with the CMS experiment at the LHC’. In: *Physics Letters B* 716.1 (Sept. 2012), pp. 30–61. ISSN: 0370-2693. DOI: 10.1016/j.physletb.2012.08.021. URL: <http://dx.doi.org/10.1016/j.physletb.2012.08.021>.
- [10] Fabienne Marcastel. *CERN’s Accelerator Complex*. Poster-2013-377. Oct. 2013. URL: <http://cds.cern.ch/record/1621586>.
- [11] CERN. *The accelerator complex*. URL: <https://home.cern/science/accelerators/accelerator-complex> (visited on 30/09/2021).
- [12] Alessio Piucci. *The LHCb Upgrade*. J. Phys.: Conf. Ser. 878 012012. 2017.

- 
- [13] LHCb Collaboration. *LHCb - Large Hadron Collider beauty experiment*. URL: <http://lhcb-public.web.cern.ch/Images2015/Images2018/LHCbUpgrade.jpg> (visited on 30/09/2021).
- [14] Rolf Lindner. *DEFINITION OF THE COORDINATE SYSTEM*. Version 1. LHCb-C-EN-0001. Feb. 2013. URL: <https://edms.cern.ch/ui/file/372642/1/LHCb-coord-system.pdf>.
- [15] The LHCb Collaboration. *LHCb VELO Upgrade Technical Design Report*. Tech. rep. Nov. 2013. URL: <https://cds.cern.ch/record/1624070>.
- [16] The LHCb Collaboration. *LHCb Tracker Upgrade Technical Design Report*. Tech. rep. CERN-LHCC-2014-001. LHCb-TDR-015. Feb. 2014. URL: <http://cds.cern.ch/record/1647400>.
- [17] Plamen Hopchev. *SciFi: A large Scintillating Fibre Tracker for LHCb*. 2017. arXiv: 1710.08325 [physics.ins-det].
- [18] Ch. Ilgner et al. *The Beam Conditions Monitor of the LHCb Experiment*. 2010. arXiv: 1001.2487 [physics.ins-det].
- [19] BCM working group. Internal communication. 2021.
- [20] Sebastian Schleich. ‘FPGA based Data Acquisition and Beam Dump Decision System for the LHCb Beam Conditions Monitor’. Diploma thesis. TU Dortmund, June 2008.
- [21] E. Buchanan. ‘The LHCb Vertex Locator (VELO) Pixel Detector Upgrade’. In: *Journal of Instrumentation* 12.01 (Jan. 2017), pp. C01013–C01013. DOI: 10.1088/1748-0221/12/01/c01013. URL: <https://doi.org/10.1088/1748-0221/12/01/c01013>.
- [22] Karol Hennessy. ‘LHCb VELO upgrade’. In: *Nuclear Instruments and Methods in Physics Research Section A: Accelerators, Spectrometers, Detectors and Associated Equipment* 845 (2017). Proceedings of the Vienna Conference on Instrumentation 2016, pp. 97–100. ISSN: 0168-9002. DOI: <https://doi.org/10.1016/j.nima.2016.04.077>. URL: <https://www.sciencedirect.com/science/article/pii/S016890021630290X>.
- [23] I Belyaev et al. ‘Handling of the generation of primary events in Gauss, the LHCb simulation framework’. In: *Journal of Physics: Conference Series* 331.3 (Dec. 2011), p. 032047. DOI: 10.1088/1742-6596/331/3/032047. URL: <https://doi.org/10.1088/1742-6596/331/3/032047>.
- [24] Torbjörn Sjöstrand, Stephen Mrenna and Peter Skands. ‘A brief introduction to PYTHIA 8.1’. In: *Computer Physics Communications* 178.11 (June 2008), pp. 852–867. ISSN: 0010-4655. DOI: 10.1016/j.cpc.2008.01.036. URL: <http://dx.doi.org/10.1016/j.cpc.2008.01.036>.

- [25] D. J. Lange. ‘The EvtGen particle decay simulation package’. In: *Nucl. Instrum. Meth. A* 462 (2001). Ed. by S. Erhan, P. Schlein and Y. Rozen, pp. 152–155. DOI: 10.1016/S0168-9002(01)00089-4.
- [26] J. Allison et al. ‘Geant4 developments and applications’. In: *IEEE Transactions on Nuclear Science* 53.1 (2006), pp. 270–278. DOI: 10.1109/TNS.2006.869826.
- [27] G. Apollinari et al. *High-Luminosity Large Hadron Collider (HL-LHC): Technical Design Report V. 0.1*. Tech. rep. 2017. DOI: 10.23731/CYRM-2017-004.
- [28] The LHCb Collaboration. *LHCb Trigger and Online Upgrade Technical Design Report*. Tech. rep. CERN-LHCC-2014-016. LHCb-TDR-016. May 2014. URL: <http://cds.cern.ch/record/1701361>.
- [29] Magnus Lieng. ‘Studies of the Machine Induced Background, simulations for the design of the Beam Condition Monitor and implementation of the Inclusive  $\phi$  Trigger at the LHCb experiment at CERN’. Dissertation. TU Dortmund, July 2011. DOI: 10.17877/DE290R-735.
- [30] Lev Davidovich Landau. ‘On the energy loss of fast particles by ionization’. In: *J. Phys.* 8 (1944), pp. 201–205.
- [31] P.A. Zyla et al. ‘Review of Particle Physics’. In: *PTEP* 2020.8 (2020), p. 083C01. DOI: 10.1093/ptep/ptaa104.
- [32] S. Hancock et al. ‘Energy loss and energy straggling of protons and pions in the momentum range 0.7 to 115 GeV/c’. In: *Phys. Rev. A* 28 (2 Aug. 1983), pp. 615–620. DOI: 10.1103/PhysRevA.28.615. URL: <https://link.aps.org/doi/10.1103/PhysRevA.28.615>.
- [33] Yuki Sato et al. ‘Charge-collection efficiency of single-crystal CVD diamond detector for low-energy charged particles with energies ranging from 100keV to 2MeV’. In: *Nuclear Instruments and Methods in Physics Research Section A: Accelerators, Spectrometers, Detectors and Associated Equipment* 834 (2016), pp. 218–222. ISSN: 0168-9002. DOI: <https://doi.org/10.1016/j.nima.2016.08.020>. URL: <https://www.sciencedirect.com/science/article/pii/S0168900216308385>.
- [34] R. C. Alig, S. Bloom and C. W. Struck. ‘Scattering by ionization and phonon emission in semiconductors’. In: *Phys. Rev. B* 22 (12 Dec. 1980), pp. 5565–5582. DOI: 10.1103/PhysRevB.22.5565. URL: <https://link.aps.org/doi/10.1103/PhysRevB.22.5565>.
- [35] Michal Mazurek. *LHCb Experiment Control System API*. URL: <https://lbcsdata.cern.ch/> (visited on 30/09/2021).
- [36] Mark Winter. *WebElements*. URL: <https://www.webelements.com/aluminium/> (visited on 30/09/2021).

- 
- [37] Engineering ToolBox. *Specific Heat of some Metals*. 2003. URL: [https://www.engineeringtoolbox.com/specific-heat-metals-d\\_152.html](https://www.engineeringtoolbox.com/specific-heat-metals-d_152.html) (visited on 30/09/2021).
- [38] Tim Evans et al. *The Timepix4 telescope*. Presented on the EP R&D 1.1 meeting. Apr. 2021. URL: [https://indico.cern.ch/event/1021155/contributions/4286010/attachments/2233118/3784346/slides\\_tpx4.pdf](https://indico.cern.ch/event/1021155/contributions/4286010/attachments/2233118/3784346/slides_tpx4.pdf).
- [39] K. Akiba et al. ‘LHCb VELO Timepix3 telescope’. In: *Journal of Instrumentation* 14.05 (May 2019), P05026–P05026. ISSN: 1748-0221. DOI: 10.1088/1748-0221/14/05/p05026. URL: <http://dx.doi.org/10.1088/1748-0221/14/05/P05026>.
- [40] The CentOS Project. *CentOS Linux*. URL: <https://www.centos.org/centos-linux/> (visited on 30/09/2021).
- [41] CERN. *CERN CentOS 7 - Linux@CERN*. URL: <https://linux.web.cern.ch/centos7/> (visited on 30/09/2021).
- [42] ETM professional control GmbH. *SIMATIC WinCC Open Architecture Portal*. URL: <https://www.winccoa.com/> (visited on 30/09/2021).
- [43] Paul Burkimsher et al. *WinCC OA and the JCOP Framework*. Presentations as part of the Joint WinCCOA JCOP Framework Course. 2020. URL: <https://edms.cern.ch/ui/#!/master/navigator/project?P:1601072490:1601072490:subDocs>.
- [44] ETM professional control GmbH. *WinCC OA @ CERN*. URL: <https://www.winccoa.com/news/detail/wincc-oa-cern.html> (visited on 30/09/2021).
- [45] CERN. *About JCOP*. URL: <https://jcop.web.cern.ch/> (visited on 30/09/2021).
- [46] CERN. *JCOP Framework*. URL: <https://jcop.web.cern.ch/jcop-framework> (visited on 30/09/2021).
- [47] CERN. *JCOP Framework Component Installation Tool*. URL: <https://jcop.web.cern.ch/jcop-framework-component-installation-tool> (visited on 30/09/2021).
- [48] Raima Inc. *RAIMA Database Manager (RDM) | High-Speed Embedded Database*. URL: <https://raima.com/> (visited on 30/09/2021).
- [49] Oracle. *Oracle Database*. URL: <https://www.oracle.com/database/> (visited on 30/09/2021).
- [50] Oracle. *Oracle Cloud helps CERN explore our universe*. URL: <https://www.oracle.com/customers/infrastructure/cern/> (visited on 30/09/2021).

- [51] OPC Foundation. *Unified Architecture*. URL: <https://opcfoundation.org/about/opc-technologies/opc-ua/> (visited on 30/09/2021).
- [52] C. Gaspar. *DIM*. URL: <http://dim.web.cern.ch/> (visited on 30/09/2021).
- [53] Keithley Instruments Inc. *Series 2400 SourceMeter. User's Manual*. 2400S-900-01 Rev. K. Sept. 2011. URL: <https://de.tek.com/keithley-source-measure-units/keithley-smu-2400-series-sourcemeter-manual/series-2400-sourcemeter>.
- [54] Keithley Instruments Inc. *Model 2410 1100 V SourceMeter Instrument. Service Manual*. 2410S-902-01C. Apr. 2017. URL: <https://de.tek.com/keithley-source-measure-units/keithley-smu-2400-series-sourcemeter-manual-3>.
- [55] Keysight Technologies. *GPIB, USB and Instrument Control. For Easy PC-to-Instrument Connections*. Data Sheet. Aug. 2021. URL: <https://www.keysight.com/de/de/assets/7018-01270/data-sheets/5989-1889.pdf>.
- [56] National Instruments Corp. *Engineer Ambitiously - NI*. URL: <https://www.ni.com/en-gb.html> (visited on 30/09/2021).
- [57] vddvss. *linux-gpib-packaging*. GitHub repository. Feb. 2019. URL: <https://github.com/vddvss/linux-gpib-packaging>.
- [58] GitHub Inc. *GitHub: Where the world builds software*. URL: <https://github.com/> (visited on 30/09/2021).
- [59] fmhess. *linux\_gpib\_firmware*. GitHub repository. June 2020. URL: [https://github.com/fmhess/linux%5C\\_gpib%5C\\_firmware](https://github.com/fmhess/linux%5C_gpib%5C_firmware).
- [60] Patrick Schnabel and Thomas Schaerer. *DNS - Domain Name System*. URL: <https://www.elektronik-kompodium.de/sites/net/0901141.htm> (visited on 30/09/2021).
- [61] Python Software Foundation. *Welcome to Python.org*. URL: <https://www.python.org/> (visited on 30/09/2021).
- [62] Python Software Foundation. *17.1. threading - Thread-based parallelism*. Python package. URL: <https://docs.python.org/3.6/library/threading.html> (visited on 30/09/2021).
- [63] PyVISA Authors. *PyVISA: Control your instruments with Python*. Python package. URL: <https://pyvisa.readthedocs.io/en/latest/> (visited on 30/09/2021).
- [64] Radu Stoica and CERN LHCb Online Group. *PyDIM documentation*. Python package. URL: <http://lhcbdoc.web.cern.ch/lhcbdoc/pydim/guide/index.html> (visited on 30/09/2021).



- 
- [65] Guido van Rossum and Python Software Foundation. *18.5. asyncio - Asynchronous I/O, event loop, coroutines and tasks*. Python package. URL: <https://docs.python.org/3.6/library/asyncio.html> (visited on 30/09/2021).
- [66] PyVISA Authors. *PyVISA-py: Pure Python backend for PyVISA*. Python package. URL: <https://pyvisa.readthedocs.io/projects/pyvisa-py/en/latest/> (visited on 30/09/2021).
- [67] Vinay Sajip and Python Software Foundation. *16.6. logging - Logging facility for Python*. Python package. URL: <https://docs.python.org/3.6/library/logging.html> (visited on 30/09/2021).
- [68] Python Software Foundation. *14.2. configparser - Configuration file parser*. Python package. URL: <https://docs.python.org/3.6/library/configparser.html> (visited on 30/09/2021).
- [69] Python Software Foundation. *16.4. argparse - Parser for command-line options, arguments and sub-commands*. Python package. URL: <https://docs.python.org/3.6/library/argparse.html> (visited on 30/09/2021).
- [70] C. Gaspar. *LIBRARY: fwDim*. URL: [https://lhcb-online.web.cern.ch/ecs/fw/FwDIM\\_v17r2/index.html](https://lhcb-online.web.cern.ch/ecs/fw/FwDIM_v17r2/index.html) (visited on 30/09/2021).
- [71] J. R. Cook and G. Thomas. *ELMB128 Documentation*. “Everything you wanted to know but were afraid to ask”. Feb. 2005.
- [72] Henk Boterenbrood. *CANopen Firmware Framework for the ELMB (Embedded Local Monitor Board)*. Version 1.2. Nov. 2004. URL: <https://www.nikhef.nl/pub/departments/ct/po/html/ELMB128/ELMBfw.pdf>.
- [73] Nikiel Piotr and contributing authors. *ELMB Documentation and Framework Component*. Feb. 2020. URL: <https://twiki.cern.ch/twiki/bin/view/Atlas/DcsElmb>.
- [74] SYS TEC electronic AG. *USB-CANmodul. System Manual*. Version 2.05. Sept. 2019. URL: [https://www.systec-electronic.com/fileadmin/Redakteur/Unternehmen/Support/Downloadbereich/Handbuecher/L-487e\\_02\\_05\\_USB-CANmodul.pdf](https://www.systec-electronic.com/fileadmin/Redakteur/Unternehmen/Support/Downloadbereich/Handbuecher/L-487e_02_05_USB-CANmodul.pdf).
- [75] Anjali Rai and Deepak Yadav. ‘Evaluating wiring Configurations for RTD Sensor in Temperature Measurement’. English. In: *i-Manager’s Journal on Electronics Engineering* 10.1 (Sept. 2019). Copyright - 2019 i-manager publications. All rights reserved, pp. 1–7. URL: <https://www.proquest.com/scholarly-journals/evaluating-wiring-configurations-rtd-sensor/docview/2320966638/se-2?accountid=14531>.
- [76] Honeywell International Inc. *HIH-4000 Series. Humidity Sensors*. Feb. 2010. URL: <https://sensing.honeywell.com/honeywell-sensing-hih4000-series-product-sheet-009017-5-en.pdf>.

- [77] Honeywell International Inc. *Humidity Sensor Theory and Behavior*. Application Sheet. Mar. 2008. URL: <https://prod-edam.honeywell.com/content/dam/honeywell-edam/sps/siot/en-us/products/sensors/humidity-with-temperature-sensors/common/documents/sps-siot-009024-2-enciid-49925.pdf>.
- [78] Bourns Inc. *4100R Series - Thick Film Molded DIPs*. Sept. 2019. URL: <https://www.bourns.com/pdfs/4100R.pdf>.
- [79] M. Lawrence. ‘The relationship between relative humidity and the dewpoint temperature in moist air - A simple conversion and applications’. In: *Bulletin of the American Meteorological Society* 86 (2005), pp. 225–233.
- [80] Arden L. Buck. ‘New Equations for Computing Vapor Pressure and Enhancement Factor’. In: *Journal of Applied Meteorology and Climatology* 20.12 (1981), pp. 1527–1532. DOI: 10.1175/1520-0450(1981)020<1527:NEFCVP>2.0.CO;2. URL: [https://journals.ametsoc.org/view/journals/apme/20/12/1520-0450\\_1981\\_020\\_1527\\_nefcvp\\_2\\_0\\_co\\_2.xml](https://journals.ametsoc.org/view/journals/apme/20/12/1520-0450_1981_020_1527_nefcvp_2_0_co_2.xml).
- [81] SYS TEC electronic AG. *Device Driver*. URL: <https://www.systemec-electronic.com/en/company/support/device-driver/> (visited on 30/09/2021).

## Acknowledgement

I want to sincerely thank everybody who supported me in writing this master thesis. Without their help it would not have been possible to deliver the thesis in this form. My first thanks goes to Prof. Dr. Johannes Albrecht, who welcomed me to the E5 chair and allowed me to work out the presented topic. I would also like to thank Prof. Dr. Kevin Kröniger as the second corrector of the thesis.

My special thanks goes to Elena for supervising and supporting me during the year of the thesis. She always took the time out of her busy schedule to answer any of my many questions in a calm and precise manner. I cannot count the times she helped me out of a difficult situation by providing me with meaningful feedback during our many discussion sessions.

In addition I want to give many thanks to Holger and Martin. While during the pandemic it was not possible to visit the university regularly, they were always the people on site I could turn to. I also very much appreciate that they and Henning always invited me to join them in their game of frisbee during the breaks.

Julian I would like to thank for the time I spent at CERN where we shared a flat together. I had a lot of fun during our talks in the evening, not to mention my first visit to the LHCb cavern! Here I want to include Dirk and Janina who partly accompanied us during the visit. More of my thanks goes to Dirk for always very actively encouraging discussions about my work and to Janina for providing me some of the images of my setup. For the setup I also thank Kai for helping me to better understand some of the hardware components.

Finally, I want to thank my family and my friend Yannik for their continued support during my study. Their encouragement helped me a lot in writing up this master thesis.

Thank you!